THE FIRST STRUCTURES IN THE UNIVERSE

A Theoretical Study of their Formation, Evolution, and Impact on Subsequent Structure Formation.

Dissertation der Fakultät für Physik
der
Ludwig–Maximillians–Universität München

vorgelegt von: Thomas Georg Abel
aus Straubing

München, den 23.6.1999

1. Gutachter: Simon D.M. White

2. Gutachter: Harald Lesch

Tag der mündlichen Prüfung: 20. Juni 2000

CONTENTS

Acknowledgments i
Zusammenfassung ii
Short Summary v

1 Introduction **1**

2 Formation of Primordial Molecular Clouds **5**
2.1 Analytical Considerations for Small Scale Structure Collapse 6
2.1.1 The Density at Collapse 6
2.1.2 Molecular Chemistry and Cooling 7
2.2 The Simulations 8
2.3 Results 13
2.3.1 Morphology 13
2.3.2 Profile Plots 16
2.3.3 Evolution 18
2.3.4 Comparison to the Analytic Model 21
2.4 Discussion and Summary 25

3 Fragmentation of Primordial Molecular Clouds **28**
3.1 Simulations 29
3.2 Results 30
3.2.1 Morphology and Dynamics 30
3.2.2 Formation of the First Objects 31
3.2.3 Profiles 33
3.3 Discussion 33
3.4 Conclusions 34

4 First Structure Formation with Cosmic Strings + HDM? **37**
4.1 Introduction 38
4.2 Analytical arguments 39
4.3 Methods and initialization parameters 42
4.4 Wiggly Strings 43
4.5 Results 44
4.6 Conclusion 45

5 On the radiative Feedback of the first Cosmological Objects **47**
5.1 Intergalactic H_2 photo–dissociation 48
5.1.1 Level distribution of intergalactic H_2 48
5.1.2 Relevant Lyman–Werner Bands 49
5.1.3 Cosmic Line Transfer 51
5.1.4 Ratecoefficients 55
5.1.5 Does intergalactic H_2 significantly modulate a soft UV background? 55
5.2 The structure of cosmological H_2 photo–dissociation regions 56

5.3 The influence of a soft UV background on structure formation 57
5.3.1 Equilibrium Arguments 58
5.3.2 Time dependent analysis 58
5.3.3 Could Self–shielding play a role? 60
5.4 Summary and Conclusions 62

6 Lyman Limit Absorption Systems at high redshifts 64
6.1 Introduction 65
6.2 A New Population of Lyman Limit Systems 66
6.2.1 Physical properties 66
6.2.2 The predicted number density of LLS 69
6.3 Discussion 71

7 Radiative Transfer Effects during photo–heating of the IGM 73
7.1 Introduction 75
7.2 Photoheating 75
7.2.1 Optical thin *vs* optical thick 75
7.2.2 Energy input during reionization 76
7.2.3 Photoheating after reonization 77
7.3 Implications 79
7.3.1 Temperature of the IGM 79
7.3.2 Absorption properties of the IGM 80
7.3.3 Baryons in shallow potential wells 80
7.4 Conclusions 81

8 Cosmological Radiative Transfer in three Dimensions 82
8.1 Introduction 83
8.2 Cosmological Radiative Transfer 84
8.3 Implementation 85
8.3.1 Choosing Angles 86
8.3.2 Casting Rays 87
8.3.3 Computing Rates 88
8.3.4 Faster than light I–fronts 89
8.4 Applications 89
8.4.1 Spherical I–front 89
8.4.2 Cosmological Density Field 90
8.5 Summary 92
8.6 Another much faster method? 92

9 Summary and possible Future Research 94
9.1 First Structure Formation 95
9.2 Effects of radiative transfer 96
9.3 Numerical cosmological radiation hydrodynamics 97

References 98

ACKNOWLEDGMENTS

Mike, my friend, thank you so much! Without your support I would not sit here finishing my dissertation. In particular without wearing a green jacket ... ;–)

Thank you, Simon, for your generosity and support.

Thanks to all my collaborators and colleagues for making our scientific journey so much fun.

Sabine – Danke! Forever is too little time with you.

This thesis is dedicated to my parents, my brother, and my granny. Thank you for believing in me throughout all these years.

ZUSAMMENFASSUNG

Die vorliegende Dissertation beschäftigt sich mit Themen der frühen Strukturentstehung im Universum, welche sich in drei zusammenhängende Teilgebiete einordnen lassen. 1) Die Entstehung und Fragmentation der ersten kosmologischen Objekte. 2) Auswirkungen der Physik des Strahlungstransportes auf die Strukturenstehung. 3) Neue Methoden und Ansätze zur numerischen kosmologischen mehrdimensionalen Strahlungshydrodynamik.

Der erste Teil dieser Doktorarbeit befaßt sich, nach einer kurzen Einführung, mit Details der frühen Strukturenstehung zu sehr hohen Rotverschiebungen $z \gg 5$. Eine gegebene baryonische (Gas) Dichtefluktuation, welche aufgrund ihrer Gravitation kontrahiert kann nur zu stellaren Dichten komprimieren wenn sie in der Lage ist ihre interne thermische Energie abzustrahlen. Andernfalls würden schließlich Druckkräfte den Kollaps aufhalten. Für Galaxien wird diese sogennante Kühlung vor allem durch neutrale Wasserstoffatome bereitgestellt. In diesem Fall gibt ein freies Elektron einen Teil seiner thermischen Energie an ein im Wasserstoff gebundenes Elektron ab. Hierbei wird das gebunde Elektron in einen höheren elektronischen Zustand des Wasserstoffs angeregt. Begiebt sich nun das angeregte Elektron durch spontanen Zerfall zurück in den Grundzustand werden ein oder mehrere Lichtquanten freigesetzt. Verläßt diese Strahlung nun die kollabierende Wolke geht also thermische Energie des Systems durch Strahlung verloren. Diese Kühlung vermindert somit den Gasdruck des Gases und erlaubt es der Wolke sich weiter zu verdichten. Dieser Mechanismus ist jedoch nur möglich wenn das freie Elektron ausreichend Energie besitzt, um das gebundene Elektron anzuregen. Es stellt sich heraus, daß dies nur bei Temperaturen von $\gtrsim 10000$ Kelvin erreicht werden kann. Die Objekte welche in dieser Arbeit diskutiert werde haben nicht genügend potentielle (Gravitations-) Energie, um solch hohe Temperaturen zu erreichen. Für diese "kleinen" Objekte übernimmt molekularer Wasserstoff die Kühlungsarbeit. Hierbei werden Rotations– und Vibrations–Schwingunen im Wasserstoffmolekül durch Zusammenstöße mit atomarem Wassertoff angeregt. Strahlungs–Quadrupolübergange des di–atomischen Moleüls setzen nun wieder Photonen frei, welche ungehindert die sich verdichtende Gaswolke verlassen können, und so zum Verlußt interner thermischer Energie führen. Bei Labordichten bilden sich Wasserstoffmoleküle in einem neutralen Wasserstoff–Helium Gemisch hauptsächlich durch Dreikörperstöße von Wasserstoffatomen. In primordialen Gas hingegen geschieht dies mit Hilfe von freien Elektronen als Katalysatoren. Diese bilden durch Kollisionen mit atomaren Wasserstoff das negative Wasserstoffion H^-, welches dann mit einem weiteren Wasserstoffatom zu einem elektronisch angeregtem H_2 Molekül assoziiert und dabei das Elektron wieder abgibt. Die Existenz von freien Elektronen bei Temperaturen unterhalb von zehntausend Kelvin ist ein Nichgleichgewichtseffekt der bei kosmologischen Dichten auftreten kann. Zusätzlich spielt die Dynamik dunkler Materie eine entscheidende Rolle in heutigen Modellen der Stukturenstehung. Man vermutet, dass diese dunkle Materie aus nich–relativistischen schwach wechselwirkenden Teilchen, sogennanten WIMPS[1], besteht. In der kosmologischen Hydrodynamik ist es also notwendig das N–Körperproblem der dunklen Materie und der Hydrodynamik des Gases

---

[1] **W**eakly **I**nteracting **M**assive **P**articles

simultan zu lösen. Im Rahmen meiner Diplomarbeit hatte ich geignete chemische und thermodynamische nicht–gleichgewichts Modelle zur numerischen hydrodynamischen Simulation, der oben erwähnten Physik, entwickelt. Im ersten Teil dieser Dissertation werden nun drei verschiedene Anwendungen unserer hydrodynamischen Methoden auf die Enstehung der ersten kosmologischen Objekte im Universum vorgestellt.

Das zweite Kapitel bespricht Resultate mehrerer Simulationen mit einer effektiven Auflösung von 512^3. Hier ist es zum ersten mal möglich die Morphologie von den typischerweise 10^6 Sonnenmassen schweren Strukturen zu beschreiben. Sie befinden sich in virialisierten dunkle Materie Halos, welche sich an den Knotenpunkten länglicher Filamente, bilden. Sobald die relative Häufigkeit von H_2 Moleülen einen Wert von ein paar mal 10^{-4} überschreitet gelingt es dem Gas effektiv zu kühlen und sich zum Zentrum der dunklen Halo hin zu verdichten. Überaschenderweise gelingt es immer nur einem geringem Teil des Gases stark zu kühlen. Dieses Ergebnis könnte bedeuten, daß die Effizienz der Sternentstehung in den studierten kleinen Objekten weit geringer sein könnte als man das für die schwereren Galaxien erwarten würde. Leider kann man mit der beschränkten Auflösung der angewandten Methode keine detailierten Aussagen über die weitere Entwicklung innerhalb der Protogalaxie machen. Eine neue Methode, das sogenannte Adaptive Mesh Refinment, zur Lösung hydrodynamischer Gleichungnen erlaubt es jedoch diesen Nachteil zu überwinden. Hier wird das numerische Gitter an den interessanten Stellen immer weiter verfeinert, um noch kleinere Skalen aufzulösen. Mit dieser innovativen Methode gelang es uns nun nicht nur der Enstehung der ersten Objekte zu folgen sondern auch der Fragmentation des Gases in dichte "proto-stellare" Klumpen. Diese Arbeit ist im dritten Kapitel diskutiert und zeigt deutlich die Stärke der neuen numerischen Methode. Es werden unterschiedliche Skalen, welche sich um einen Faktor 3×10^5 voneinander unterscheiden, realistisch berechnet. Von dieser Arbeit lernt man wie sich das proto–galaktische Gas in 200 Kelvin kalte primordiale Molekülwolken mit ca. $10^3 - 10^4\ M_\odot$ aufteilt. Innerhalb bilden sich ca $100\ M_\odot$ dichte Klumpen durch eine erneute Schwerkraftsinstabilität. Es ist bemerkenswert, daß der limitierende Faktor in diesen Simulationen nicht Auflösung oder Computerzeit sondern das Modell der primordialen Gaschemie, welche bei höheren Dichten komplexer wird. Seit den sechziger Jahren wurde über die Natur dieser ersten Objekte spekuliert. In der Literatur findet man Behauptungen über die Enstehung von braunen Zwergen, Jupiter großen Klumpen, schwerer schwarze Löcher, hauptsächlich schwerer Sterne, Kugelsternhaufen, und vieles mehr. All diese Arbeiten argumentieren von mehr oder weniger den gleichen Anfangsbedingungen und kommen doch zu so unterschiedlichen Ergebnissen. Unsere Simulation ermöglichen nun zum ersten Male genauere Vorhersagen zu treffen. Sobald sich jedoch der erste Stern in einem proto–galaktischen Objekt bildet ist es wahrscheinlich, daß dieser die Entwicklung seiner Umgebung wesentlich beeinflußt. An diesem Punkt scheitert jede ab initio Simulation da die komplexe Physik des Strahlungstransportes, Staubentstehung, Sternenwinde, Magnetfelder, und Supernovae noch nicht realistisch modelliert werden können.

Im vierten Kapitel widmen wir uns kurz einem alternativen Modell der Strukturenstehung zu; kosmische Strings mit heißer dunkler Materie. Es wurde in den 80ziger Jahren spekuliert, daß sich in diesem Modell Strukturen schon bei Rotverschiebung weit grösser als 100 bilden könnten. Hier würde ein sicher mit nahezu Lichtgeschwindigkeit bewegender String die Baryonen in einer Ebene verdichten. Die heiße dunkle Materie hingegen würde den String nicht bemerken da ihre kinetische Energie größer als die gravitative Wirkung des Strings. Könnten nun das heisse Gas in der Ebene stark kühlen würde man Fragmentation erwarten. Um diese Vorhersage zu testen haben wir unsere detailiert Gasphysik in ein ein und zwei–dimensionales kosomologisches Hydrodynamik–Program integriert, und eine Parameterstudie durchgeführt. Von diesen Simulationen und analytischen Überlegungen konnten wir zweifelsfrei nachweisen, daß sich keine kosmologisch interessanten

Strukturen bilden können bevor die dunkle Materie kalt genug ist, um mit den Baryonen zu kollabieren. Unsere Resultate sind ein weiteres Indiz für die Unzunlänglichkeit des kosmischen String Modelles der Strukturenstehung.

Im fünften Kapitel fragen wir nun welchen Einfluß die Ultraviolette Strahlung der ersten Sterne auf die weitere Strukturentstehung hat. Hierzu diskutieren wir die detailierte Mikro–physik der H_2 Photo–Dissoziation und zeigen auf wie eine externes Strahlungsfeld die Molekülbildung in protogalaktischen Strukturen verhindern kann. Der qualtitative chemo–thermische Aufbau einer kosmologischen H_2 Photo–Dissoziationsregion wird ausführlich besprochen. Schließlich besprechen wir die kosmologische Bedeutung dieses Effektes. Es wird einen negatives Feedback erwartet falls die ersten Strukturen Sterne sind. Diese Rückwirkung könnte jedoch auch positive Auswirkungen haben falls die ersten Strahlungsquellen harte Röntgenstrahlung emittieren.

Falls kleine Strukturen wirklich keine Moleküle bilden können wenn ein UV Strahlungshintergrund besteht, dann würden viele kleine neutrale virialisierte Objekte vorhergesagt. Im sechsten Kapitel zeigen wir, daß solche mini–Galaxien die beobachteten Lyman Limit Absorptionssysteme in Quasar Spektren erklären können.

Im siebten Kapitel besprechen wir einen an sich einfachen Effekt des Strahlungstransports und dessen Einfluß auf die Heizung des intergalaktischen Mediums. Da Photoionisation bevorzugt durch Photonen an der Absorptionskante erfolgt erscheint das Spektrum einer Quelle umso härter umso weiter man von ihr entfernt ist. Überaschenderweise wurde dieses Faktum von keinem der heutigen hydrodynamischen Modelle von Quasarabsorptionlinien berücksichtigt. Wir zeigen hier, wie man dadurch die Temperatur und so den Anteil der thermischen Verbreiterung der Absorptionlinien um einen Faktor 2 unterschätzen kann. Dieser Effekt erhöht auch die minimale Masse von in dunkle Materie Halos gebundenen Baryonen, welche durch Photoionisation verdampft werden können. Diese Besonderheiten unterstreichen die dringende Notwendigkeit Strahlungstransport in unseren mehrdimensionalen Hydrodynamischen Modelle des intergalaktischen Mediums und der Galaxienenstehung. Zu genau diesem Ziel geben wir im achten Kapitel eine Methode welches erlaubt den Strahlungstransports in der Umgebung mehrerer Quellen in drei Dimensionen zu berechnen. Die numerische Methode zeichnetet sich durch ihre konservative Formulierung aus, welche Ionisationsfronten mit der richtigen Geschwindigkeit verfolgt, unabhängig von der Hydrodynamik gegebenen numerischen Auflösung. Der Algorithmus löst die Strahlungstransportgleichung entlang einer adaptiv gewählten Anzahl von radialen Strahlen.

Alle Kapitel dieser Dissertation, außer Einleitung und Zusammenfassung, wurden zur Veröffentlichung eingereicht, akzeptiert, oder sind bereits erschienen.
- Kapitel 2: Abel, T., Anninos, P., Norman, M.L., & Zhang, Y. 1998, ApJ, 508, 518.
- Kapitel 3: Abel, T., Bryan, G.L., Norman, M.L. 1999, ApJ eingereicht.
- Kapitel 4: Abel, T., Stebbins, A., Anninos, P., Norman, M.L. 1998, ApJ, 508, 534.
- Kapitel 5 zum Teil in: Haiman, Z., Abel, T., Rees, M.J. 1999, ApJ, in Druck und Ciardi, B., Ferrara, A., Abel, T. 1999, ApJ, in Druck.
- Kapitel 6: Abel, T., & Mo, H.J. 1998, ApJL, 494, L151.
- Kapitel 7: Abel, T., & Haehnelt, M. 1999, ApJL, in Druck.
- Kapitel 8: Abel, T., Norman, M.L., Madau, P. 1999, ApJ, in Druck.

Andere veröffentlichte Beiträge zu diesem Thema, Ergebinsse meiner Diplomarbeit, findet man in
- Abel, T., Anninos, P., Zhang, Y., and Norman, M.L. 1997, NewA, 2, 181,
- Anninos, P., Zhang, Y., Abel, T., and Norman, M.L. 1997, NewA, 2, 209,
- Tegmark, M., Silk, J., Rees, M.J., Blanchard, A., Abel, T., Palla, F. 1997, ApJ, 474, 1.

SHORT SUMMARY

New technology drives advances in observational cosmology at a rapid pace. Armed with ground breaking sensitivities the next generation of ground and space observatories are specifically designed to dected the farthest and earliest objects in the Universe at multiple wavelengths. A deeper theoretical understanding aiding the interpretation of the newest observations is highly desirable. Fortunately, the advent of numerical cosmological hydrodynamics in this decade provides us a tool to test and develop realistc and predictive theories of structure formation. The first part of this PhD thesis presents new methods and results that simulate realistically the relevant physics of First Structure Formation in unique detail. Then various effects of radiative transfer on structure formation are discussed. These aspects of radiative transfer apply to quasar absorption line systems, first structure formation and the thermal history of the intergalactic medium. The remainder focuses on new numerical methods introducing cosmological radiation hydrodynamics as new means for the study of the formation and evolution of structure in the universe.

Most of the work discussed in this dissertation has been submitted to, accepted to, or has alredy appeared in the Astrophysical Journal.

Chapter 2: Abel, T., Anninos, P., Norman, M.L., & Zhang, Y. 1998, ApJ, 508, 518.

Chapter 3: Abel, T., Bryan, G.L., Norman, M.L. 2000, ApJ, in press.

Chapter 4: Abel, T., Stebbins, A., Anninos, P., Norman, M.L. 1998, ApJ, 508, 534.

Chapter 5 partially in: Haiman, Z., Abel, T., Rees, M.J. 2000, ApJ, in press; and Ciardi, B., Ferrara, A., Abel, T. 2000, ApJ, in press.

Chapter 6: Abel, T., & Mo, H.J. 1998, ApJL, 494, L151.

Chapter 7: Abel, T., & Haehnelt, M. 1999, ApJL, .

Chapter 8: Abel, T., Norman, M.L., Madau, P. 1999, ApJ, .

Other contributions of mine to this subject which were published in refereed Journals are:

Abel, T., Anninos, P., Zhang, Y., and Norman, M.L. 1997, NewA, 2, 181.

Anninos, P., Zhang, Y., Abel, T., and Norman, M.L. 1997, NewA, 2, 209.

Tegmark, M., Silk, J., Rees, M.J., Blanchard, A., Abel, T., Palla, F. 1997, ApJ, 474, 1.

CHAPTER 1

Introduction

A variety of questions in physical cosmology are intimately related to the understanding of the formation and the nature of the first cosmological objects in the Universe. In particular the first stars synthesize the first heavy elements[1] and emit the first UV photons after recombination. Both of these effects are of fundamental importance for the subsequent evolution of the intergalactic medium and structure formation in general.

Saslaw and Zipoy (1967) realized the importance of gas phase H_2 molecule formation in primordial gas for the formation of proto–galactic objects. Employing this mechanism in Jeans unstable clouds, Peebles and Dicke (1968) formulated their model for the formation of primordial globular clusters. Further pioneering studies in this subject were carried out by Takeda et al. (1969), Matsuda et al. (1969), and Hirasawa et al. (1969) who followed in detail the gas kinetics in collapsing objects and studied the possible formation of very massive objects (VMO's). Hutchins (1976) then looked in greater detail at the effects of rotation and asked what minimum Jeans mass can be reached in a collapsing primordial gas cloud. In the 1980's major contributions to this field were made by Rees and Kashlinsky (1983), Carr et al. (1984), and Couchman and Rees (1986), who all studied the possible cosmological consequences of population III star formation. Their main conclusion was that for hierarchical structure formation scenarios the first objects might reheat and reionize the universe and thus raise the Jeans mass, influencing subsequent structure formation quite dramatically. Massive Pop III stars would also pre–enrich the intergalactic medium with metals.

Mostly due to our poor understanding of primordial star formation, many of the conclusions of these studies depend sensitively on the specific assumptions adopted for the IMF and star formation efficiencies. At a workshop in Florence two years ago, for example, it has been argued that, starting from similar initial conditions, the first objects to form might be Jupiter size "clumpuscules" (Combes), brown dwarfs (Silk), $0.5 M_\odot$ MACHO's (Nishi; Paolis), standard IMF stellar systems (Haiman), or even massive black holes (Haiman; Zinnecker; Silk)[2]. This meeting clearly exmplified that no consensus has been reached in this, at least 30 year old, question: "What is the nature of the first cosmological objects?".

It is also clear that the uncertainties mentioned above arise due to the inherently multidimensional, nonlinear, nonequilibrium physics which determine the collapse and possible fragmentation of gravitationally and thermally unstable primordial gas clouds. One important difficulty in this problem is that H_2 formation in these systems is possible only due to nonequilibrium chemical kinetics, which allows free electrons to act as catalysts at low temperatures ($T < 10^4$ K). This complexity forced all early studies to focus on single cell calculations solving the time dependent rate equations for the chemical network (cf. Hirasawa 1969; Hutchins 1976; Palla et al. 1983; Puy et al. 1996; Tegmark et al. 1997; Stancil et al. 1998) in homologous, spherical collapse models. Bodenheimer (1986) was the first to address the hydrodynamic aspects of the problem, but only in spherical symmetry. Similarly, using a spherical Lagrangian hydrodynamics code and solving the kinetic rate equations simultaneously, Haiman, Thoul and Loeb (1996) studied the important question of which mass scales are able to cool efficiently enough to collapse.

Unfortunately, the issue of fragmentation cannot be addressed in spherically symmetric models. However, steady advances in computer hardware and new developments in more efficient algorithms to solve the chemical rate equations (Anninos et al. 1997, Gnedin and Ostriker 1997) are now enabling us to study the properties of the first structures in the universe in multi–dimensions (Abel 1995; Zhang et al. 1997; Gnedin and Ostriker 1997; Abel et al. 1998a,b,c). These methods are also being employed to study the non–equilibrium kinetics in quasar absorption line systems (cf. Zhang et al. 1995). In this thesis we will discuss some of these new techniques, the first results obtained with them, as well as some new preliminary results illustrating which questions can and will be addressed in future studies. Allow us first, however, to look at some aspects of the physics and associated difficulties of first structure formation in greater detail.

---

[1] including Carbon and Oxygen; the basic building blocks of life on earth.

[2] These contributions were published in special edition of *Mem.S.A.It.* Vol. 69, N.2, 1998

On the nature of the problem

The basic question we are interested in is whether the first structures formed in a given cosmological model fragment or not? If they do, we would like to determine the distribution of fragment masses. If they do not, we would like to ask whether a very massive object is formed or if the material is able to directly collapse into a black hole.

If the models put forward in previous investigations are correct (for references see the previous section), first structure formation is a very well defined problem because, for a given cosmogony, the thermodynamic properties, baryon content, and chemical composition are specified for the entire universe at high redshifts, at least in a statistical sense. Furthermore, the dominant physical laws are readily identified with the general theory of relativity describing the evolution of the background space–time geometry and particle geodesics, the Euler equations governing the motion of the baryonic fluid(s) in an expanding universe, and the primordial kinetic rate equations determining the chemical processes. However, the range of length scales important to this problem span a very wide range. To illustrate this let us compare the Schwarzschild radius to the comoving length scale of the region out of which a fluctuation of given mass collapses. One finds,

$$\frac{R}{l} \approx 4 \times 10^{-14} \left(\frac{M}{10^6 M_\odot} \right)^{2/3} \Omega_0^{-1/3} h^{-2/3},$$

suggesting that if one would like to follow the collapse of a primordial gas cloud to a primordial black hole one has to cover at least 15 orders of magnitude in length scales. Since the Schwarzschild radius of a $5 \times 10^5 M_\odot$ black hole is roughly equal to the solar radius, a similar range of length scales would have to be covered if the cloud were to fragment into stars. In the latter case one might hope that it would be sufficient to follow the collapse only down to scales of the observed infall regions around protostars which are of the order $\sim 1000\,\mathrm{au}$. In this case covering eight orders of magnitude in length scales might be sufficient to understand the basic properties of collapsing primordial gas clouds. These numbers stand in contrast to the dynamic range of past and current "high resolution" three–dimensional Eulerian numerical simulations of $\lesssim 10^3$.

One important ingredient in first structure formation is the nonequilibrium chemistry and cooling behavior of primordial gas that is responsible for the formation of hydrogen molecules. Fortunately, we have now numerical methods (Anninos et al. 1997) and a reliable model for primordial gas (Abel et al. 1997) that is valid for number densities $\lesssim 10^4\ \mathrm{cm}^{-3}$. However, as we will show in the following, new numerical techniques allow us to follow the collapse of the first objects to yet higher densities. This introduces significant complications in the chemistry with non–equilibrium level distributions of the molecules and level– dependent rate coefficients for an increased number of chemical reactions. This additional complexity will be a challenge for future studies, and at present one can only hope that they will not affect the collapse too much.

Yet another complexity will arise when numerical simulations reach high enough column densities such that the cloud becomes opaque to its cooling radiation, at which point the effects of radiative transfer will have to be included. In fact in the classical picture of opacity limited fragmentation for star formation (Hoyle 1953) it is the interplay of radiative transfer and hydrodynamics that determines the fragment masses.

So far only five multi–dimensional numerical investigations of first structure formation have been carried out. Anninos and Norman (1996) studied the collapse of cosmological pancakes in one and two dimensions including the full nonequilibrium primordial gas chemistry. Gnedin and Ostriker (1997) studied the formation of small scale structure and their subsequent impact on structure formation. This latter study contributed significantly to our understanding of the global evolution of the intergalactic medium at high redshift. This thesis contains three more multi–dimensional studies of the collapse of the first structures in cold dark matter (CDM) dominated universes as well as cosmic string + hot dark matter models.

The remainder of this dissertation is concerned with effects of radiative transfer in physical cosmology and with numerical algorithms that enable us to include it in multi–dimensional cosmological hydrodynamics.

Chapter 2

Formation of Primordial Molecular Clouds

ABSTRACT

We investigate the formation of the first primordial star clusters from high–σ perturbations in a cold dark matter dominated universe. For this purpose we have developed a powerful 2–level hierarchical cosmological code with a realistic and robust treatment of multi–species primordial gas chemistry, paying special attention to the formation and destruction of H_2 molecules, non–equilibrium ionization, and cooling processes. We performed 3–D simulations at small scales and at high redshifts and find that, analogous to simulations of large scale structure, a complex system of voids, filaments, sheets, and spherical knots at the intersections of filaments form. On the total mass scales covered by our simulations ($1 \times 10^5 - 1 \times 10^9\ M_\odot$) which collapse at redshifts $z > 25$, we find that only within the spherical knots can enough H_2 be formed ($n_{H_2}/n_H \gtrsim 5 \times 10^{-4}$) to cool the gas appreciably. The time dependence of the formation of H_2 molecules and the final H_2 fraction in the simulations agree with the theoretical predictions of Abel (1995) and Tegmark et al. (1997) remarkably well. Using a different H_2 cooling function (Lepp and Shull, 1983) we repeat the calculations of Tegmark et al. (1997). The minimum mass that is found to collapse and cool via H_2 for a given redshift is found to be an order of magnitude lower than found by Tegmark et al. (1997). Furthermore, we discuss the possible implications for theories of primordial star formation from the extensive merging of small structure that is inherent in hierarchical models. In our simulation typically only 5–8% percent of the total baryonic mass in the collapsing structures is found to cool significantly. Assuming the Padoan (1995) model for star formation, our results would predict the very first stellar systems to be as small as $\sim 50\ M_\odot$. Some implications for primordial globular cluster formation scenarios are also discussed.

2.1 ANALYTICAL CONSIDERATIONS FOR SMALL SCALE STRUCTURE COLLAPSE

In this section we review some analytical arguments which will be of use when discussing our numerical results.

2.1.1 The Density at Collapse

For structures where the initial gas pressure is dynamically important, a simple estimate of the density at collapse is derived by solving the equations of hydrostatic equilibrium (Sunyaev & Zel'dovich 1972; Tegmark et al. 1997). Defining the virial temperature T_{vir} through $3kT_{vir}/2 = -m_p\Phi/2$, where

Φ is the gravitational potential, the density contrast δ can be written as

$$(1+\delta) = \frac{\rho}{\rho_B} = \left(1 + \frac{6}{5}\frac{T_{vir}}{T_B}\right)^{3/2}, \tag{2.1}$$

where T_B and ρ_B denote the background temperature and density, respectively. The morphological characteristics of the object described by equation (2.1) is determined by the gravitational potential Φ. The factor $1/2$ on the right hand side of the definition of T_{vir} is chosen to reproduce the canonical definition of $3kT_{vir}/2 = m_p v^2/2$ for a virialized spherical system with velocity dispersion v. The analysis of a spherical collapse model for structures where the initial gas pressure is not important gives $\delta = 18\pi^2$ for the overdensity at virialization (Gunn and Gott 1972). Hence equation (2.1) should only be applicable as long as $\delta \lesssim 18\pi^2$. Furthermore the assumption of hydrostatic equilibrium, which we used to derive equation (2.1), can only hold for structures with infall (virial) velocities that are small compared to the sound speed of the gas, so that no virialization shock will form. This is true for spherical objects with masses $\lesssim 100\ M_\odot h^{-1}\Omega_0^{-0.5}(1+z_{coll})^{3/2}$, which is in reasonable agreement with the condition $\delta \lesssim 18\pi^2$.

The temperature of the primordial gas decouples thermally from the cosmic background radiation at $z \sim 200$ and evolves adiabatically ($T/\rho^{\gamma-1} = const.$) afterwards. Hence we can write

$$T_B = 135\ \mathrm{K}\left(\frac{1+z}{100}\right)^2, \tag{2.2}$$

which can be used to derive the density at collapse,

$$n_{coll} = \begin{cases} 1\ \mathrm{cm}^{-3}\left(\frac{T_{vir}}{400\ \mathrm{K}}\right)^{3/2}\left(\frac{\Omega_B h^2}{0.025}\right), & \text{for } \frac{T_{vir}}{400\ \mathrm{K}} < \left(\frac{1+z}{30}\right)^2 \\ 1\ \mathrm{cm}^{-3}\left(\frac{1+z}{30}\right)^3\left(\frac{\Omega_B h^2}{0.025}\right), & \text{otherwise.} \end{cases} \tag{2.3}$$

This suggests that, for the smallest structures, the typical density at collapse does *not* depend on the collapsing redshift, and that the chemical and cooling behavior for these structures will be the same for any collapse redshift. However, the above analysis is certainly oversimplified in the sense that it does not include a detailed treatment of the dark matter potential in which the baryons will fall.

2.1.2 Molecular Chemistry and Cooling

Molecular hydrogen can not be destroyed efficiently in primordial gas at low temperatures (< few $\times 10^3$K) unless there is a radiation flux higher than $\sim 3\times10^{-26}$ erg cm^{-2} s^{-1} in the Lyman Werner Bands. Once self–shielding is important even higher fluxes would be needed. Furthermore, only two H_2 producing gas phase reactions operate on time–scales less than the Hubble time: the charge exchange reaction

$$\mathrm{H_2^+} \quad + \quad \mathrm{H} \quad \rightarrow \quad \mathrm{H_2} \quad + \quad \mathrm{H^+}, \tag{2.4}$$

and the dissociative attachment reaction

$$\mathrm{H^-} \quad + \quad \mathrm{H} \quad \rightarrow \quad \mathrm{H_2} \quad + \quad \mathrm{e^-}. \tag{2.5}$$

The H_2 abundance will thus be determined by the H_2^+ and H^- abundances. However, one typically finds that the H_2^+ equilibrium abundance is much lower than that of H^- ($k_9 \ll k_7$ in the notation of Abel et al. 1997a) and additionally that the rate coefficient of reaction (2.4) is about 2.4 times smaller than reaction (2.5). Consequently the H_2 formation is dominated mostly by reaction (2.5).

In the absence of an external UV background at gas temperatures below 6000K, one can integrate the rate equations for the free electron and the molecular hydrogen fraction to find the time evolution of the H_2 fraction during the collapse of primordial gas clouds (see Abel 1995 and Tegmark et al. 1997)

$$\begin{aligned} f_{H_2}(t) &= f_{H_2}(t=0) + \frac{k_{PA}}{k_{rec}} \ln(x_0 n_H k_{rec} t + 1) \\ &= f_{H_2}(t=0) + 1.0 \times 10^{-8} T_{vir}^{1.53} \ln(t/t_{rec} + 1), \end{aligned} \tag{2.6}$$

where k_{PA}, k_{rec}, t_{rec}, x_0, and n_H are the rate coefficients of photo–attachment of H^- and recombination to neutral hydrogen in $\mathrm{cm}^3\ \mathrm{s}^{-1}$, the initial recombination timescale (see equation (2.7)), the initial ionized fraction, and the neutral hydrogen number density (in cm^{-3}), respectively. The production of H_2 therefore depends only logarithmically on time, and increases most rapidly within the first few initial recombination timescales so that it defines a characteristic H_2 formation timescale,

$$t_{rec} = \frac{1}{n_{H^+} k_{rec}} = 5.0 \times 10^{13} \left(\frac{n_H}{100\mathrm{cm}^{-3}}\right)^{-1} \left(\frac{x}{10^{-4}}\right)^{-1} \left(\frac{T}{1000\mathrm{K}}\right)^{0.65} \ \mathrm{s}. \tag{2.7}$$

Here $k_{rec} = 1.8 \times 10^{-10} T^{-0.65}\ \mathrm{cm}^3\ \mathrm{s}^{-1}$ is our fit to the data of Ferland et al. (1992), which is accurate to within a few percent for temperatures below 10^4K. A good estimate for the H_2 fraction is given by evaluating equation (2.6) at $t \sim 2t_{rec}$. The temperature dependence enters from the ratio of the recombination and H^- formation rates. A typical H_2 fraction of $n_{H2}/n \sim 10^{-3}$ is produced during the collapse of structures with virial temperatures greater than 10^3 K. For temperatures higher than 6000 K, the charge exchange with protons will efficiently destroy H_2, and equation (2.6) will not be applicable. However, during the collapse of clouds with such high virial temperatures, the final H_2 fraction will, nevertheless, be $f_{H_2}(T \sim 6000\ \mathrm{K}) \sim 6 \times 10^{-3}$ (see Abel et al. 1997a). Comparing equation (2.6) with the dynamical timescale for a spherical top–hat model, Tegmark et al. (1997) argued for a rule of thumb, stating: "A spherical primordial gas cloud will be able to undergo a stage of free-fall collapse if its H_2 fraction becomes $\gtrsim 5 \times 10^{-4}$."

2.2 THE SIMULATIONS

A numerical code with high spatial and mass resolution is required to model both the collapse of sufficiently large scale structure and the microphysics of chemical reactions and radiative cooling which are important on the smaller scales. We can achieve high dynamical ranges with the two–level hierarchical three–dimensional code (HERCULES) that we have developed for hydrodynamic cosmology (Anninos, Norman & Clarke 1994; Anninos, Zhang, Abel & Norman 1997). This code simulates structure formation in an expanding dark matter dominated universe with Newtonian gravity, multi–fluid hydrodynamics, radiative cooling, non–equilibrium chemistry and external radiation fields, although the latter is not present in these studies. It also utilizes nested grid methods for both the gas and dark matter particles to achieve higher resolution over a selected sub–domain of the coarser parent grid. At the small scales resolved by our calculations (~ 1 kpc), it is important to track the different chemical species in order to model the chemistry and radiative cooling accurately. For this purpose we independently evolve the following nine chemical species: neutral hydrogen H, ionized hydrogen H^+, negative hydrogen ions H^-, hydrogen molecules H_2, ionized hydrogen molecules H_2^+, neutral helium He, singly–ionized helium He^+, doubly–ionized helium He^{++}, and free electrons e^-. The 28 most important chemical rate equations are solved in non–equilibrium for the abundances of each of the nine species. The rate coefficients used in the chemistry model are provided in Abel, Anninos, Zhang & Norman (1997a). We have also implemented a comprehensive model for the radiative cooling of the gas (Anninos, Zhang, Abel & Norman 1997) that includes atomic line excitation, recombination, collisional ionization, free–free transitions, molecular line excitations, and Compton scattering off the cosmic background radiation (CBR) by electrons.

We apply our code to high redshift pre–galactic structure formation and evolution, investigating the collapse of the first high–σ bound objects with baryonic masses in the range $10^4 - 10^8 M_\odot$. Our model background spacetime is a flat ($\Omega_0 = 1$) cold dark matter dominated universe with Hubble constant $H_0 = 50$ km s^{-1} Mpc^{-1} and baryon fraction $\Omega_B = 0.06$, consistent with the constraints from big–bang nucleosynthesis (Copi, Schramm & Turner 1995). The baryonic matter is composed of hydrogen and helium in cosmic abundance with a hydrogen mass fraction of 76% and ratio of specific heats $\gamma = 5/3$. The data is initialized at redshift $z = 100$ with matter perturbations derived from the Harrison–Zel'dovich power spectrum modulated with a transfer function appropriate for CDM adiabatic fluctuations and normalized to the cluster scale $\sigma_{8h^{-1}} = 0.7$. Bertschinger's (1994) constrained realization procedure is used to construct 3 and 4σ fluctuations at the box center over a region of 1/5 the box length.

The chemical abundances are initialized according to the estimates provided by Anninos & Norman (1996). For the primary hydrogen and helium species, we use the residual ionization estimate of Peebles (1968, 1993):

$$\frac{n_{H^+}}{n_H} = 2.4 \times 10^{-4}\ \Omega_0^{1/2} \frac{0.05}{h\Omega_B}, \tag{2.8}$$

and assume negligible amounts of n_{He^+}/n_H and $n_{He^{++}}/n_H$ ($\lesssim 10^{-14}$). The concentrations of the intermediaries, H^- and H_2^+, and hydrogen molecules are given by

$$\begin{aligned} \frac{n_{H^-}}{n_H} &= 2 \times 10^{-9}\ T_K^{0.88}\ \frac{n_{H^+}}{n_H}\ , & (2.9) \\ \frac{n_{H_2^+}}{n_H} &= 3 \times 10^{-14}\ T_K^{1.8}\ \frac{n_{H^+}}{n_H}\ , & (2.10) \\ \frac{n_{H_2}}{n_H} &= 2 \times 10^{-20} \frac{f_H \Omega_0^{3/2}}{h\Omega_B} (1+z_o)^{5.1}\ , & (2.11) \end{aligned}$$

where T_K is the gas temperature in degrees Kelvin, and is set at the starting redshift by assuming an adiabatic expansion from $z = 200$, the approximate redshift at which matter/radiation interactions are negligible (see equation (2.2)). Also, f_H is the hydrogen mass fraction and $z_o = 300$ is an estimate for the largest redshift at which H_2^+ can form efficiently to produce hydrogen molecules without being photodissociated by the cosmic background radiation. For our model parameters ($f_H = 0.76$, $\Omega_0 = 1$, $\Omega_B = 0.06$ and $h = 0.5$), we find $n_{H_2}/n_H = 2.9 \times 10^{-6}$. The neutral hydrogen and helium, and electron densities are then set by the following conservation equations:

$$\rho_{He} + \rho_{He^+} + \rho_{He^{++}} = \rho_b \, (1 - f_H) \ , \tag{2.12}$$

$$\rho_H + \rho_{H^+} + \rho_{H^-} + \rho_{H_2^+} + \rho_{H_2} = \rho_b \, f_H \ , \tag{2.13}$$

$$\rho_{H^+} - \rho_{H^-} + \frac{1}{2}\rho_{H_2^+} + \frac{1}{4}\rho_{He^+} + \frac{1}{2}\rho_{He^{++}} = m_H \, n_e \ , \tag{2.14}$$

where ρ_i are the densities of the ith species, ρ_b the total baryonic density, n_e the number density of free electrons, and m_H the proton mass.

In this chapter we present results from six different nested grid calculations. We investigate the effect of increasing the large scale power by varying the parent box size over $L = 128$, 512 and 1024 kpc, and set up initial data for the collapse of both 3σ and 4σ fluctuations. The different box sizes act to parameterize the mass of the collapsing structures. Throughout the chapter we use the notation whereby the data from the sub grid (top grid) simulation of a 4σ peak in a box of size 512kpc are referred to as 4σ512S (4σ512T). The suffices S and T are sometimes dropped when we refer to properties common to both the top and sub grid. For a fixed mass scale, σ effectively defines the redshift at which the structures begin to collapse. We use 128^3 cells to cover both the top and sub grids which, for the refinement factor of four used in all our simulations, results in an effective 512^3 resolution over the sub grid domain. A box dimension of 1024 kpc is about the maximum we can attempt before losing the resolution in the sub grid needed to resolve the H_2 chemistry and cooling. The spatial and mass resolutions of the top and sub grids are shown in Table 2.1 for each of the calculations. For comparison, we note that the mass resolution is much smaller than the Jeans mass in the background baryonic fluid, which varies from about $10^6 M_\odot$ at $z = 100$ to $\sim 10^4 M_\odot$ at $z = 10$.

Run	Grid	L (kpc)	Δx (kpc)	M_{DM} ($M_\odot$)	M_B ($M_\odot$)	ΔM_{DM} ($M_\odot$)	ΔM_B ($M_\odot$)
3(4)σ1024T	top	1024	8	7.5×10^{10}	4.5×10^9	3.6×10^4	2.1×10^3
3(4)σ512T	top	512	4	9.3×10^9	5.6×10^8	4.4×10^3	2.7×10^2
3(4)σ128T	top	128	1	1.5×10^8	8.8×10^6	6.9×10^1	4.2×10^0
3(4)σ1024S	sub	1024	2	1.2×10^9	7.1×10^7	5.6×10^2	3.3×10^1
3(4)σ512S	sub	512	1	1.5×10^8	8.8×10^6	6.9×10^1	4.2×10^0
3(4)σ128S	sub	128	0.25	2.3×10^6	1.4×10^5	1.1×10^0	6.7×10^{-2}

Table 2.1

Spatial and mass resolution of the different top and sub grid simulations. L is the comoving box size of the top grid defining the longest wavelength perturbation, Δx the comoving cell size in each computational box, M_{DM} the total dark matter mass initially in each grid, M_B the total baryonic mass, ΔM_{DM} the single dark matter particle mass, and ΔM_B the baryonic mass in a single cell at the start of the simulation at redshift $z = 100$. The same parameters were used for both the 3σ and 4σ perturbation simulations. We employ the notation 4σ1024T(S), to denote the top (sub) grid simulations of a 4σ peak in the 1024 Mpc box. When the suffices S or T are dropped we are refering to results common to both grids.

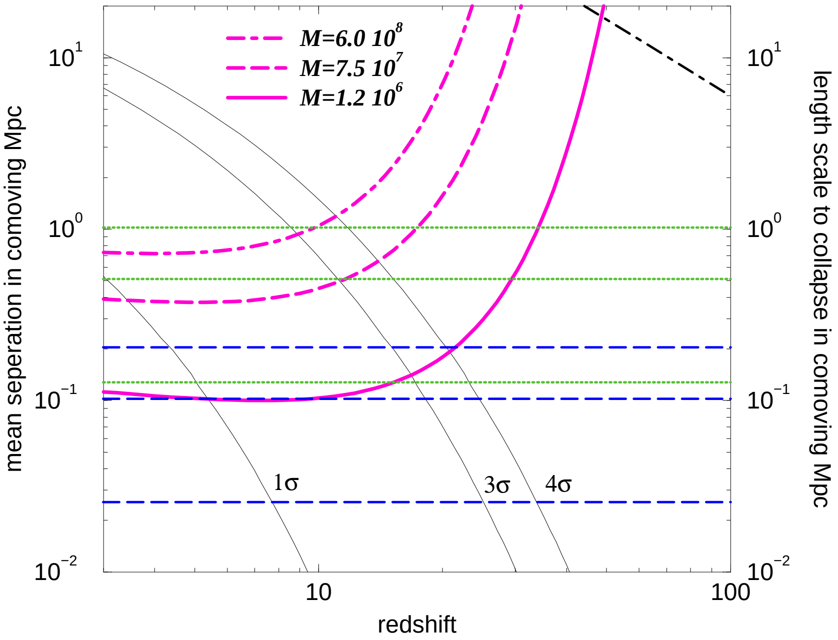

Figure 2.1

The solid lines labeled 1, 3, and 4σ depict the length scales of 1, 3, and 4σ peaks vs. their collapse redshift as predicted by linear theory. This assumes a Gaussian adiabatic CDM spectrum with $\sigma_8 = 0.7$, $\Omega_0 = 1$, and $h = 0.5$, and a linear density contrast of $\delta_c = 1.68$ at collapse. The thick solid, long dashed, and dot–dashed lines depict the comoving mean separation of peaks with a mass of 1.2×10^6, 7.5×10^7, and 6.0×10^8 $M_\odot$, as predicted by the Press–Schechter formalism, respectively. These masses correspond to the three different perturbation wavelengths we have simulated: 25.6, 102.4, and 204.8 kpc (dashed horizontal lines). The dotted horizontal lines show our box sizes, 128, 512, and 1024 comoving kpc. For reference, the Hubble horizon is shown as a dot–dashed line (in the upper right corner).

In Figure 2.1 we show the mean comoving separation, computed from the Press Schechter (1974) formalism, of the three different mass scales we have simulated. The solid, long dashed, and dashed lines correspond to a total collapsing mass of 1.2×10^6, 7.5×10^7, and 6.0×10^8 $M_\odot$ respectively. These masses correspond to perturbation wavelengths (dashed horizontal lines in Figure 2.1) of 25.6, 102.4, and 204.8 kpc, respectively. On the same graph we also plot the perturbation wavelength vs. the redshift at which linear theory predicts its overdensity to be 1.68 (its typical collapse redshift) for $\sigma = 1$, 3, and 4 peaks (solid downward sloping lines labeled 1σ, 3σ, and 4σ). Our simulation box sizes are indicated by the horizontal dotted lines. We see that the 25.6 kpc perturbation of the 4σ128 (3σ128) simulations is expected to collapse at a redshift ~ 34 (25). At these redshifts the typical mean separation of such 1.2×10^6 $M_\odot$ objects is ~ 1 Mpc (300 kpc) which is roughly 8 (2) times greater than the simulation box size of 128 kpc. For the larger box sizes (512 and 1024 kpc), the mean separation of peaks is also larger than the box at the collapse redshift by a factor of a few, and about half the box size for smaller redshifts. Although the mean separation of the simulated peaks is always within a factor of a few of the box sizes, the use of periodic boundary conditions on these small scales will limit the reliability of our results at lower redshifts. Figure 2.1 also shows that 1σ perturbations of scales 128, 512, and 1024 kpc, corresponding to our box sizes, would go non–linear at redshifts of ~ 5, 3, and 2, respectively. Therefore, we terminate our simulations well before these epochs are reached.

2.3 RESULTS

2.3.1 Morphology

In Figure 2.2 we show an evolution sequence of the logarithm of the dark matter and gas overdensities at four redshifts, $z = 35$, 22, 17, and 12, taken from the top grid evolution for the 3σ collapse with the intermediate box size $L = 512$ kpc (3σ512T). Five contour levels of $\log \rho/\overline{\rho} = (0.5, 1, 1.5, 2, 2.5)$ are displayed in the x–y plane of the cube intersecting the maximum density peak. In the gas density plots one can see two originally distinct objects at $z = 35$ that merge later on.

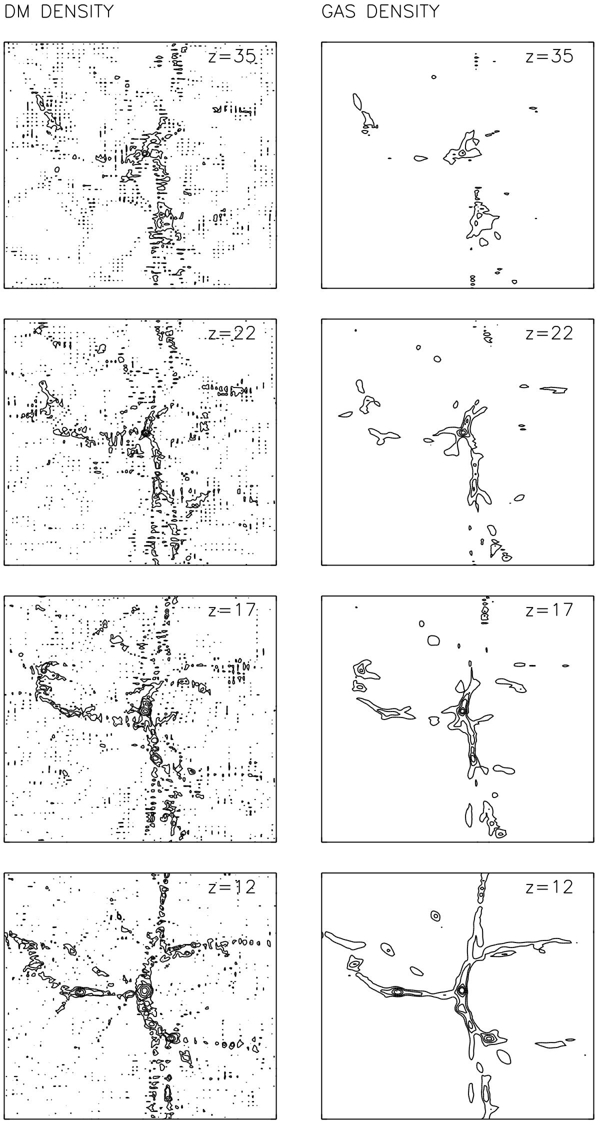

Figure 2.2

Contour surfaces showing an evolution sequence for the dark matter and baryonic gas overdensities at redshifts $z = 35$, 22, 17 and 12. Five levels (0.5, 1, 1.5, 2, 2.5) are displayed for $\log \rho/\overline{\rho}$, where $\overline{\rho}$ is the background density. Each individual plot represents a single slice intersecting the densest cell on the top grid for the 3σ run with box size $L = 512$ *kpc* (3σ512T).

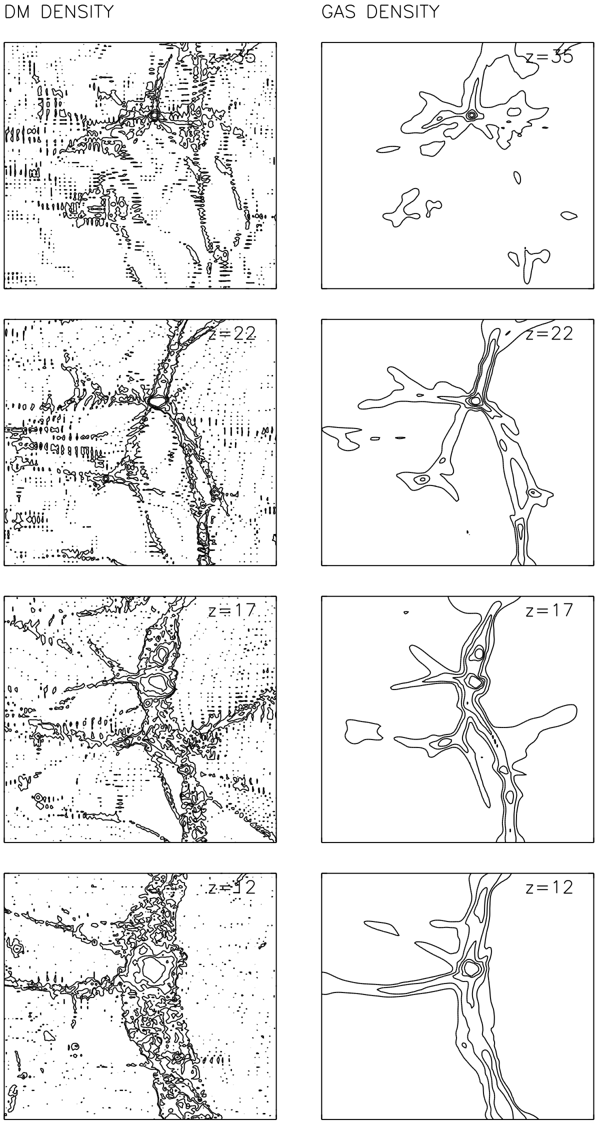

Figure 2.3

Same as in the previous figure, but for the higher resolution sub grid ($3\sigma512S$).

By redshift $z = 22$, a well developed spherical structure of total mass $\sim 4 \times 10^7\ M_\odot$ forms at the intersection of several filaments, consistent with the prediction from linear theory (see Figure 2.1). The structure continues to grow by the further collapse of nearby particles and gas, and by the merging of smaller collapsed structures. The total mass of the bound structure grows to $1.3 \times 10^8\ M_\odot$, with baryonic mass $6.8 \times 10^6\ M_\odot$ by $z = 12$. Figure 2.3 shows results analogous to those in Figure 2.2, but for the sub grid evolution. The enhanced resolution (a factor of four in length and 64 in mass) allows for more detailed and accurate studies of the collapsing structure. In fact, it is the enhanced resolution that allows the cooling flow to be modeled at all.

The top grid calculation does not have the spatial resolution required to resolve the H_2 formation/cooling region adequately.However, the subgrid calculation does, where one can see the more complex network of filamentary structure resolved. Evidently the filamentary structures observed in the gas appear also in the DM overdensity, consistent with the picture that the baryons fall into the potential well of the dark matter. In the gas overdensity (Figure 2.3) one observes how a distinct overdense region forms in the upper filament between redshifts 22 and 17, and merges then with the more massive central structure by $z = 12$. It is evident that a significant amount of mass accretes onto the central object along the filaments.

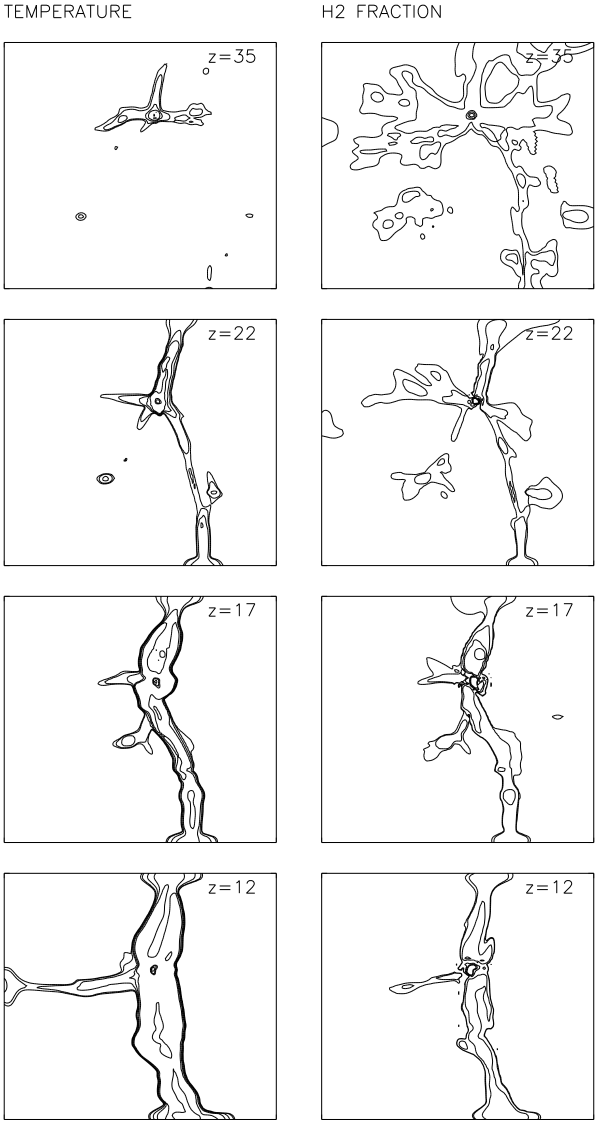

Figure 2.4

Contour surfaces showing an evolution sequence for the gas temperature and H_2 fraction n_{H2}/n_H at redshifts $z = 35$, 22, 17 and 12. Five levels are displayed for both the temperature ($\log T(eV)$ = -2.2, -2, -1.5, -1, -0.5) and the H_2 fraction ($\log n_{H2}/n_H$ = -5.05, -5, -4.5, -4, -3.5).

On the same scale as Figure 2.3, Figure 2.4 shows the evolution sequence for the gas temperature and molecular hydrogen number density fraction n_{H2}/n_H. The contour levels are $\log T(eV) = -2.2, -2, -1.5, -1, -0.5$ and $\log n_{H2}/n_H = -5.05, -5, -4.5, -4, -3.5$.

H_2 fractions exceeding the background value of $\sim 3 \times 10^{-6}$ are found only in overdense regions along the filamentary structures, and predominantly at their intersections where the densities are highest. We find typical H_2 fractions of $\sim 10^{-5}$ along the filaments, and $\gtrsim 10^{-4}$ in the spherical knots. Both of the spherical structures that are most evident in the gas contour plots of Figure 2.3, and merge between redshift 17 and 12, show H_2 fractions exceeding 3×10^{-4}. By redshift $z = 12$, the fraction of H_2 in the central structure increases to 9.1×10^{-4}, which is enough to cool the gas to $0.21eV$ ($2390K$) and allow it to collapse to a central density of ~ 100 cm^{-3}. Approximately 6% of the baryonic mass in the structure has cooled by $z = 12$, so the collapsed and cooled structure is roughly of mass 4×10^5 $M_\odot$. We note that the merger event did not destroy any molecules in the merging structures (see also Figure 2.11 below).

2.3.2 Profile Plots

In the following we present radial profile plots of various physical quantities averaged in spherical shells centered on the densest cell in the high resolution sub grid. All of these plots do not include the central zone.

Figure 2.5a shows the ratio of baryonic to total density for all of the 4σ runs versus the radius in comoving kpc. The horizontal line depicts the background (initial) value of $\Omega_B/\Omega_0 = 0.06$. Evidently the cooling at the center of the structure allows the baryons to contract, leading to an enhancement of baryons over the dark matter up to four times the background value. The radius at which the ratio of baryonic to total density starts to exceed $\Omega_B/\Omega_0 = 0.06$ coincides with the radius at which the molecular hydrogen fraction reaches 5×10^{-4}. This value agrees well with the analytical model presented in section 2.1 Note that the virial shock is located at radii larger than where the deficit is found. Hence, it is the shocked gas which eventually forms molecules, cools, and flows from the outer regions to the center of the structure that yields the baryonic to DM bias (see also Figure 2.11).

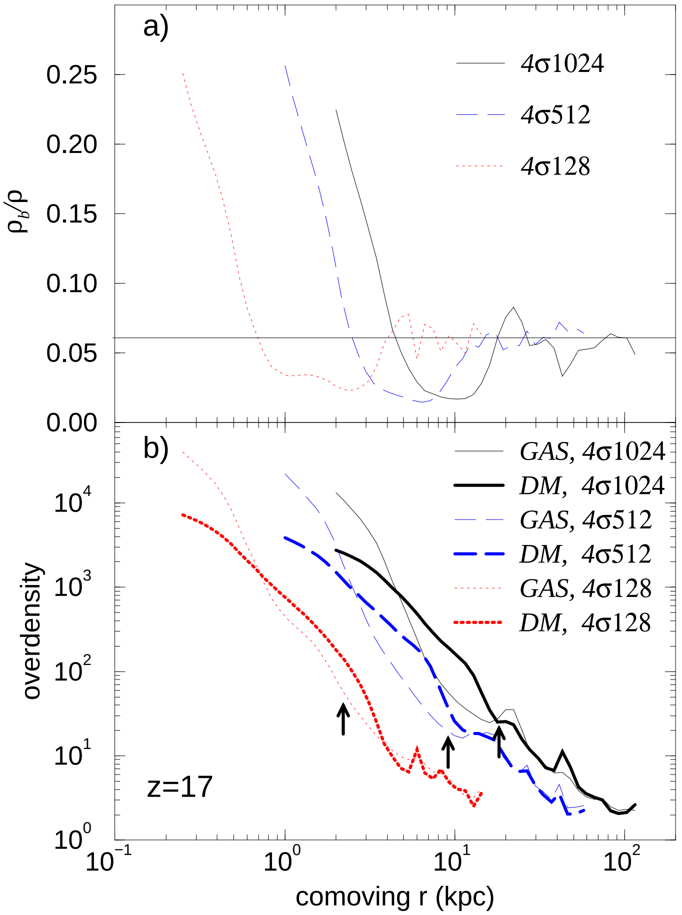

Figure 2.5

(a) Radial profiles of the baryonic fraction on the subgrid for the 4σ runs. The horizontal solid line is the average baryonic fraction $\Omega_b = 0.06$. (b) Radial profiles of the gas and dark matter overdensities for the 4σ runs. Note that the baryonic density increases substantially relative to that of the dark matter in the central core due to H_2 cooling. The arrows indicate the theoretical virial radii of the three different perturbation wavelengths we have simulated.

The baryon enhancement at the center of the structures leads to sharp overdensity profiles as shown in Figure 2.5b. The radially averaged dark matter density profile shows a complex form with apparently four regimes of different slopes. Powerlaws that fit this radial dependence have an exponent $\lesssim -1$ in the central regions, then ~ -2, -4, and again -2 in the outer regions. The arrows in Figure 2.11 indicate the theoretical viral radii of collapsed spheres with intial wavelengths corresponding to the ones we have simulated ($r_{vir} = (l/2)(18\pi^2)^{-1/3}$, where l is the perturbation wavelength). Note that, for the least massive halo, the r^{-4} feature is found just outside the virial radius, whereas for the others it is partially (4σ512S) and completely (4σ1024S) within the virial radius. This is because we plot the profiles at $z = 17$ by which time only the smallest simulated structure has fully virialized. Generally we find that the halo DM profiles within the virial radius are isothermal ($\rho \propto r^{-2}$) over a wide range of radii. This is characteristic of the universal density profile proposed by Navarro, Frenk, and White (1996, NFW hereafter),

$$\rho(r) \propto \frac{1}{(r/r_s)(1+r/r_s)^2}, \tag{2.15}$$

where r_s is some characteristic radius. They showed this formula to fit DM haloes within the virial radius of the galaxies and clusters of galaxies found in their N–body simulations. Although NFW studied DM profiles for halos with masses $\sim 10^{12}\ M_\odot$, their results are similar to what we find in our simulated halos, which are as much as 10^6 times smaller in mass. However, our DM profiles are somewhat sharper than the NFW profile, making a future high resolution study desirable to test the applicability of the universal profile to DM halos on mass scales $\lesssim 10^8\ M_\odot$, and to clarify the "feedback" of collapsing baryons to the DM density profile. Such resolution studies are in progress (Abel, Bryan, & Norman 1998)

Figure 2.6 illustrates that the central regions of collapsing small scale structure do cool by H_2 molecules that are formed using the free electrons that were left over from recombination as catalysts. It shows at $z = 27$ the radially averaged profiles for the fractional abundances of H_2 , H^- , H_2^+ , and e^-, as well as the temperature from the 3σ512S data. The molecular hydrogen formation is dominated by the H^- path, which is similar to the situation of strong shocks ($v_s \sim 100$ km/s) formed during the collapse of cosmological sheets (Anninos & Norman 1996, and Abel et al. 1997a). This is clear from Figure 2.6 since the H^- abundance always exceeds the H_2^+ abundance by more than an order of magnitude, and the fact that the dissociative attachment reaction of H^- to form H_2 is characterized by a rate coefficient that is two times greater than the charge exchange reaction of H_2^+ with H (reactions (2.4) and (2.5)). The free electron abundance is decreased only in the denser, cooler center where the radiative recombination timescales are short: the weak virialization shock is not capable of ionizing the primordial gas at this redshift. The decrease of the H^- abundance in the cooling layer is a result of the temperature decrease and the free electron depletion. Note that these results justify all the assumptions that entered the derivation of equation (2.6), further validating the analytical description given in section 2.1. Although the central parts of the structure formed hydrogen molecules solely using the residual free electrons as catalysts, the infalling material at later redshifts will be, at least partially, collisionally ionized by the stronger shock, allowing molecules to form on a faster timescale (see Figure 2.7). Furthermore, we can see that the minimal chemistry model proposed by Abel et al. (1997a) is sufficient to study the effects of primordial gas chemistry for first structure formation.

The temperature profiles at different redshifts from the 4σ512S simulation are shown in Figure 2.7. (The central temperatures can be read from Figure 2.10.) As expected, we see that the post shock temperature of the virialization shock increases towards lower redshifts as the system mass increases. It is interesting that, for the small scale structures considered here, the central region never reaches temperatures above a few thousand Kelvin. For the 4σ128S run the maximum temperature in the center of the densest structure is only ~ 900 K (see Figure 2.10). At $z = 50$, the temperature profile shows a gentle increase towards the center caused by adiabatic compression. By $z = 35$, the influence

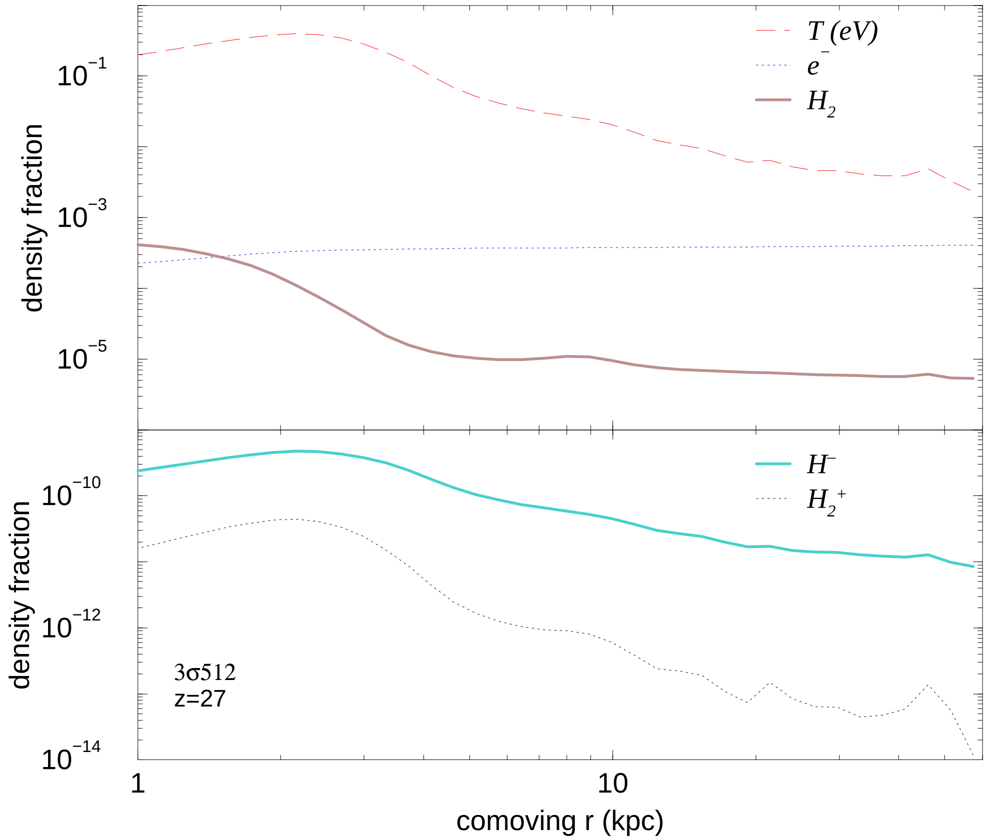

Figure 2.6

Profiles of temperature and several important species (H_2, H_2^+, H^- and e^-) at $z = 27$ for the $3\sigma512S$ run. The depletion of H^- , H_2^+ , and e^- in the H_2 forming and cooling region is evident. The virialization shock is not ionizing (yet) since the free electron fraction remains constant away from the central regions.

of radiative cooling becomes evident in the turnaround of the temperature profile in the central region. At redshifts $z \lesssim 22$, the spherically averaged post–shock temperature exceeds 10^4 K, and hence the gas becomes collisionally ionized, and more molecules form in the center to cool the gas to lower temperatures.

2.3.3 Evolution

Figure 2.8 plots versus redshift some characteristic time scales normalized to the Hubble time ($H^{-1} = H_0^{-1}(1+z)^{-3/2}$, where H_0 is the present Hubble constant) of the most important physical processes in the densest cell of the collapsing structure in the $4\sigma512$S simulation. The Bremsstrahlung and H I recombination cooling times exceed the expansion time scale by more than three orders of magnitude and are therefore not shown in the figure. The hydrogen recombination time is already close to the Hubble time at $z = 100$, allowing H_2 to form slowly. At $z \approx 50$, the gas density and temperature grow to levels that are more favorable for the creation of hydrogen molecules, and the H_2 cooling time becomes shorter than the hydrogen recombination (equation (2.7)) and dynamical ($t_{dyn} = (3\pi/(32G\rho))^{1/2} = 4.7 \times 10^7 n^{-1/2}$ years) times. The Compton cooling/heating exceeds the expansion time scale for all redshifts $\lesssim 100$ and does not influence the collapse of the central regions. The reason that the H_2 cooling time decreases monotonically with redshift, and does not start to

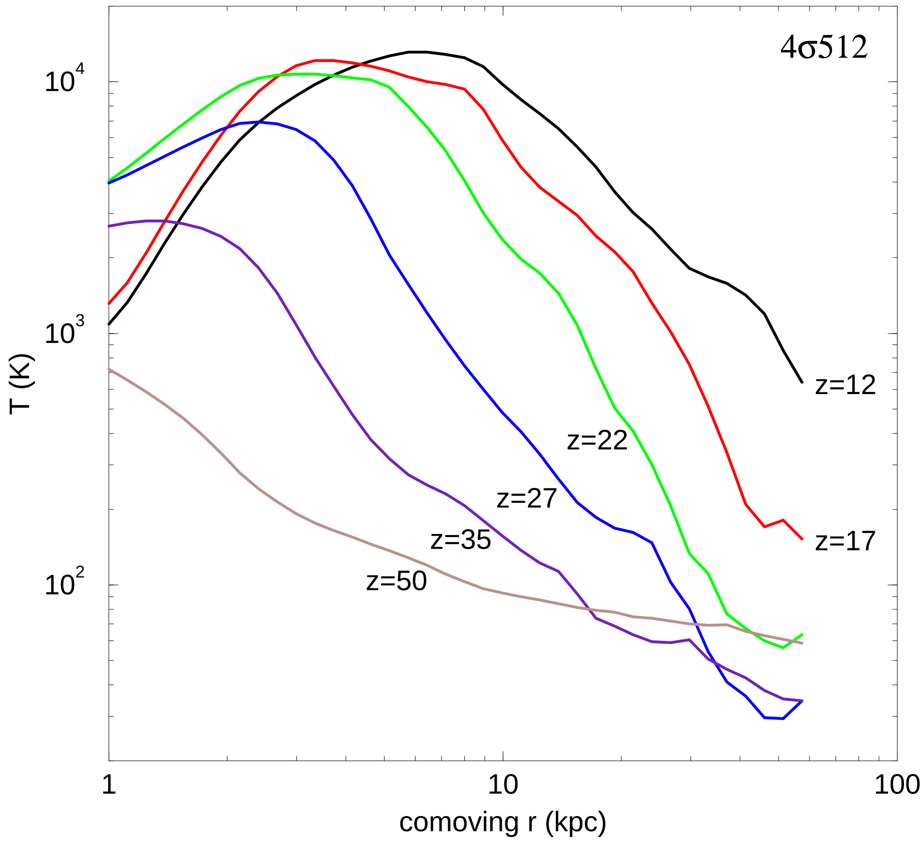

Figure 2.7

Spherically averaged radial temperature profiles for the $4\sigma512$S simulation. The adiabatic compression of the central regions is the dominant effect at redshift $z = 50$. At $z \sim 35$, H_2 cooling dominates adiabatic heating in the central regions, and effectively cools the gas. At $z \lesssim 25$ the temperature exceeds 10^4 K at a few comoving kpc from the center.

increase again, is due to the merging of small scale structures and, for the largest box sizes, an artifact of our limited numerical resolution.

The decrease in temperature and increase in density in the cores results in an even greater decrease in the Jeans mass

$$M_J = \frac{\pi}{6}\rho\lambda_J^3 = \frac{\pi}{6}\rho\left(\frac{\gamma\pi kT}{G\rho\mu m_H}\right)^{\frac{3}{2}} \approx 100T_K^{3/2}n_B^{-1/2}\ M_\odot, \tag{2.16}$$

as shown in Figure 2.9. Here n_B denotes the baryonic number density expressed in units of cm^{-3}. The background Jean's mass, plotted in Figure 2.9, is derived from the background baryon number density $1.1\times10^{-5}(\Omega_B/\Omega_0)(\Omega_0 h^2)(1+z)^3\ \mathrm{cm}^3$). Also shown in Figure 2.9 is the initial mass resolution in the coarsest grid (the parent grid with $L = 1024$ Mpc) simulations with a cell size of 8 kpc, the baryonic mass in the single densest cell of the collapsing structures, and the Jean's mass computed using the spherical collapse model with virial temperatures of 1000 K and 3000 K,

$$M_S = 100T_K^{3/2}\left(18\pi^2 n_0\right)^{-1/2}(1+z_c)^{-3/2}\ M_\odot, \tag{2.17}$$

where z_c is the collapse (virialization) redshift. The redshift at which the single cell mass curves cross the corresponding Jeans mass curves represents a limit below which the grid resolution becomes inadequate to resolve the cooling flows. In the larger mass structures (512 and 1024 kpc box sizes), the collapsed mass exceeds the Jeans mass of the cell at higher redshifts. The horizontal dashed line showing the initial mass resolution of the coarsest grid indicates that the mass resolution in

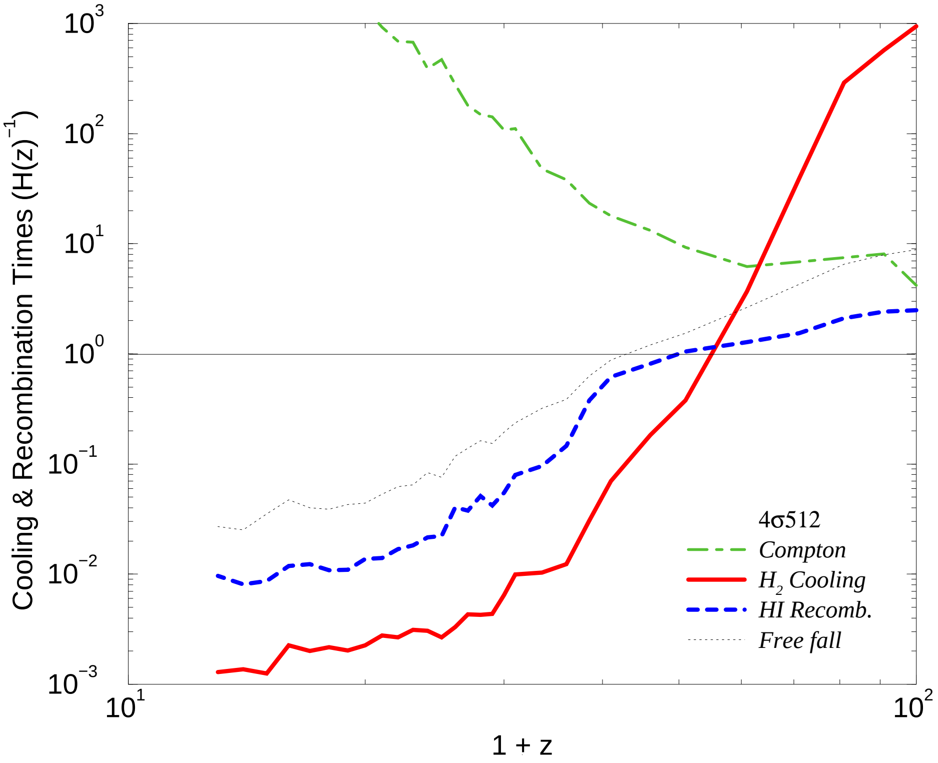

Figure 2.8

Cooling times in the densest cell found on the sub grid of the $4\sigma512$S simulation relative to the Hubble time, $H^{-1} = H_0^{-1}(1+z)^{-3/2}$, for various physical processes, including Compton and molecular hydrogen line cooling. Also shown are the hydrogen recombination and spherical free fall times.

the simulations is more than sufficient to track the baryonic Jeans mass up to the single cell mass crossing time. The minimum Jeans mass reached in the present simulations ($\sim 3 \times 10^4\ M_\odot$) suggests that the insufficient spatial resolution does not allow any predictions about fragmentation and the primordial star formation process directly. However, the physics of the initial evolution and the physical environment of primordial star forming regions are adequately captured in our numerical experiments. Clearly, higher resolution studies are desirable.

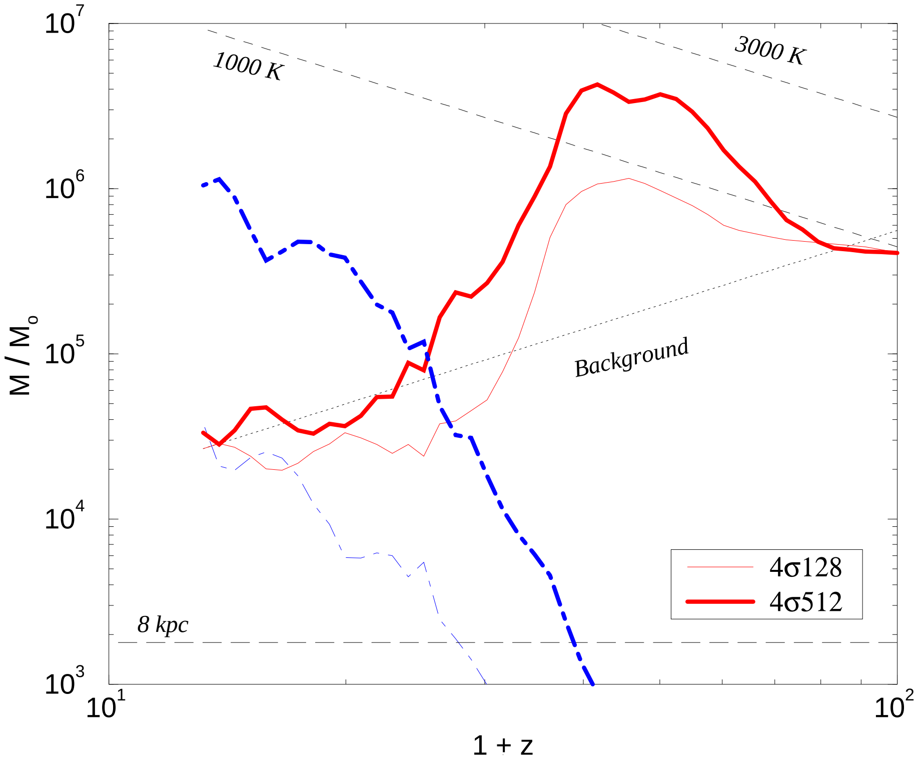

Figure 2.9

Evolution of the Jeans mass in the densest cell of the most massive structures in the 4σ128S and 4σ512S simulations (thin and thick solid lines). Also shown is the corresponding mass in the densest cell (thin and thick dot–dashed lines), the Jeans mass of the background baryonic density (dotted line), the initial baryonic mass in a single cell of the grid simulation 4σ1024T (horizontal dashed line), and the Jeans mass for spherical collapse with virial temperatures of 1000 and 3000K (dashed lines labeled with 1000K and 3000K, respectively).

2.3.4 Comparison to the Analytic Model

In the following we will test some of the assumptions used in the analytical arguments introduced in section 2.1. One typical assumption that is made (see Tegmark et al. 1997), is that a structure evolves adiabatically until virialization. However, at small wavelengths, the CDM perturbation spectrum is almost flat, causing these structures to go nonlinear almost simultaneously in time. One, therefore, expects their evolution to be marked by frequent mergers which could raise the gas to a higher adiabat by shock heating. We examine this assumption in Figure 2.10 which shows the evolution of the adiabatic invariant p/ρ^γ, the temperature, and the baryonic number density of the densest zone of the 4σ128S (thin lines) and 4σ512S (thick lines) data. Clearly, for the 4σ128 simulation, the initial contraction at $z \gtrsim 45$ is adiabatic and radiative cooling plays a role only at smaller redshifts. For the larger 4σ512 simulation box, the entropy increases in the redshift range $60 \lesssim z \lesssim 75$ due to merging, and stays roughly constant thereafter until radiative cooling becomes important at $z \lesssim 40$. H_2 cooling gives rise to a plateau in temperature until $z \lesssim 38$ when it causes the temperature to decrease. Interestingly, we see that the central regions never reach the theoretical virial temperatures which are $\sim$ 2600 K for the 4σ128, and greater than 10^4 K for the 4σ512 runs. Our simulations fail to resolve the core of these structures and hence the central density is not well defined once the gas in the

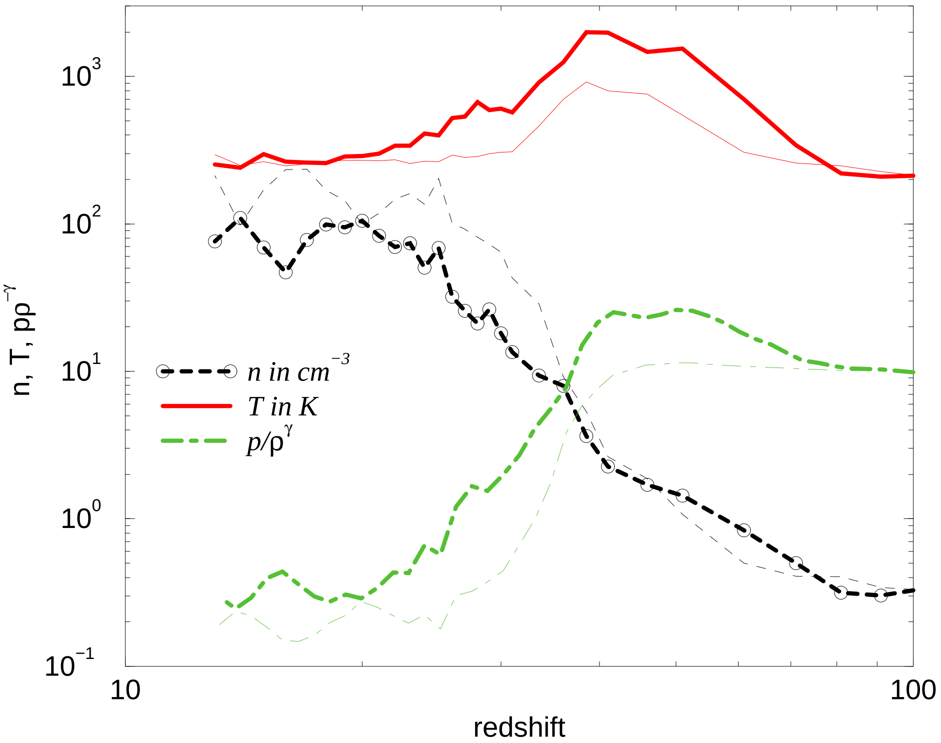

Figure 2.10

The evolution of the baryonic number density in cm^{-3} (dashed lines; circles indicate the data points), temperature in degrees Kelvin (solid lines), and the adiabatic invariant p/ρ^γ which is invariant for adiabatic processes (dot–dashed lines) for the densest zone in the $4\sigma128$S (thin lines) and $4\sigma512$S (thick lines) simulations. Here p, ρ, and γ denote the gas pressure, density, and the adiabatic index, respectively.

most central structure has cooled. Therefore, the slow growth of the density for redshifts $10 < z < 30$ does *not* indicate that the collapse is halted.

The post–shock gas has been found to evolve isobarically in the case of radiative shocks (see, for example, Shapiro & Kang 1987 and Anninos & Norman 1996). Assuming the molecular hydrogen fraction increases according to equation (2.6) (see also Figure 2.11) and isobaric evolution one can determine the temperature evolution. For the central (densest) zone of our $4\sigma128$S box, the isobaric condition predicts that the gas would be able to cool to ~ 30 K by redshift ten. The Lepp and Shull cooling function, which was used to derive the isobaric evolution, has been stated to be valid only to 100 K. However, a new study by Tiné, Lepp, and Dalgarno (1997) confirms that the H_2 cooling timescale can be short even at lower temperatures. For example they find it to be of order 1 Gyr at a temperature of 50 K, and a tenth of that at 70 K for typical H_2 fractions of 10^{-3} and $n_H \sim 100\ \mathrm{cm}^{-3}$. Hence if the gas evolves isobarically it will be able to cool to temperatures $\ll 100$ K. However, we see that the temperature and density, and hence the internal energy stay roughly constant in the final stages although the cooling time scales are short. This is due to the extensive merging in the hierarchical scenario considered here, as well as our limited numerical resolution.

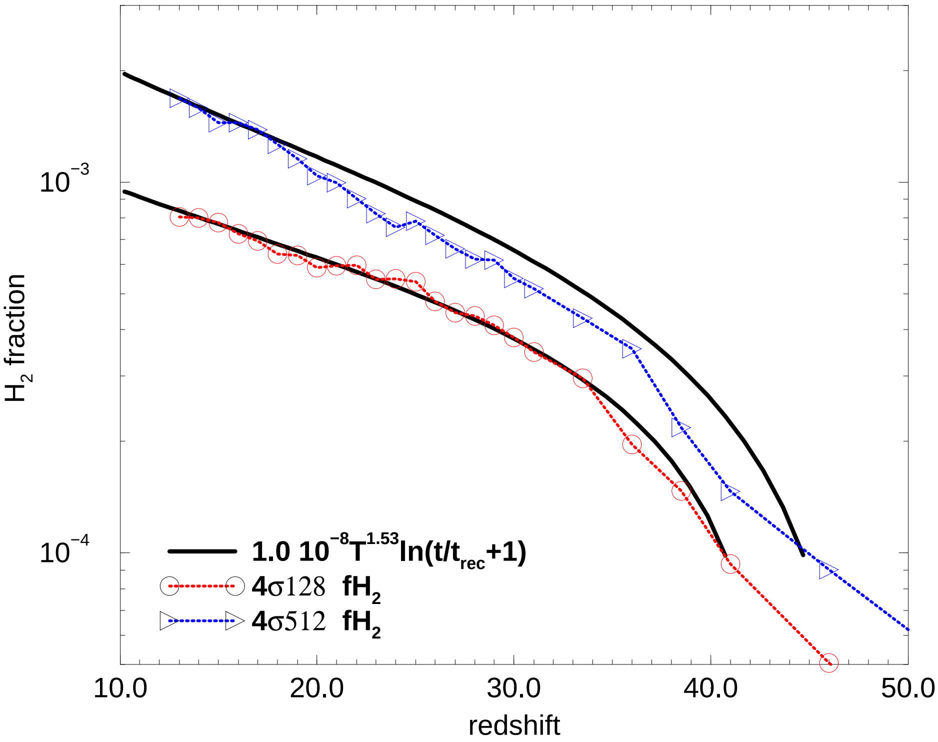

Figure 2.11

Molecular hydrogen fraction vs. redshift in the densest zone of the $4\sigma128S$ (open circles) and $4\sigma512S$ (triangles) simulations. The thick solid lines depict the approximating equation (2.6) initialized with the free electron densities, initial H_2 fraction, and temperature from the simulation.

In Figure 2.11 we compare the predictions of equation (2.6) with the results from the $4\sigma128S$ (open circles) and the $4\sigma512S$ (triangles) runs. The fit is remarkably good, although the initial temperature (or redshift) is somewhat difficult to pick out in this case since the heating due to adiabatic compression is slow, and the initial (virial) temperature is not as well defined for the larger mass scales. Analyzing the time derivative of equation (2.6) one finds for large times that $\dot{f}_{H_2} \propto T^{1.53}$ which, for the spherical collapse model, translates to $\dot{f}_{H_2} \propto M(1+z_{vir})^{1.53}$. This explains that the divergence of the two graphs in Figure 2.11 at low redshifts is due to the difference in the collapsing mass and collapse redshift.

Tegmark et al. (1997) have recently used a simple approach to derive the minimum mass scale that is able to collapse as a function of redshift. They model the density evolution in a cloud according to the predictions of the spherical collapse model, assuming the temperature increases adiabatically up to virialization and changes thereafter by radiative cooling. They simultaneously solve the rate equations for the time dependent chemistry to accurately predict H_2 formation and the subsequent cooling of the gas. We have reproduced their work with the same cooling function (Lepp & Shull 1983) used in our cosmological hydrodynamics code to compare their findings with our 3D numerical results.

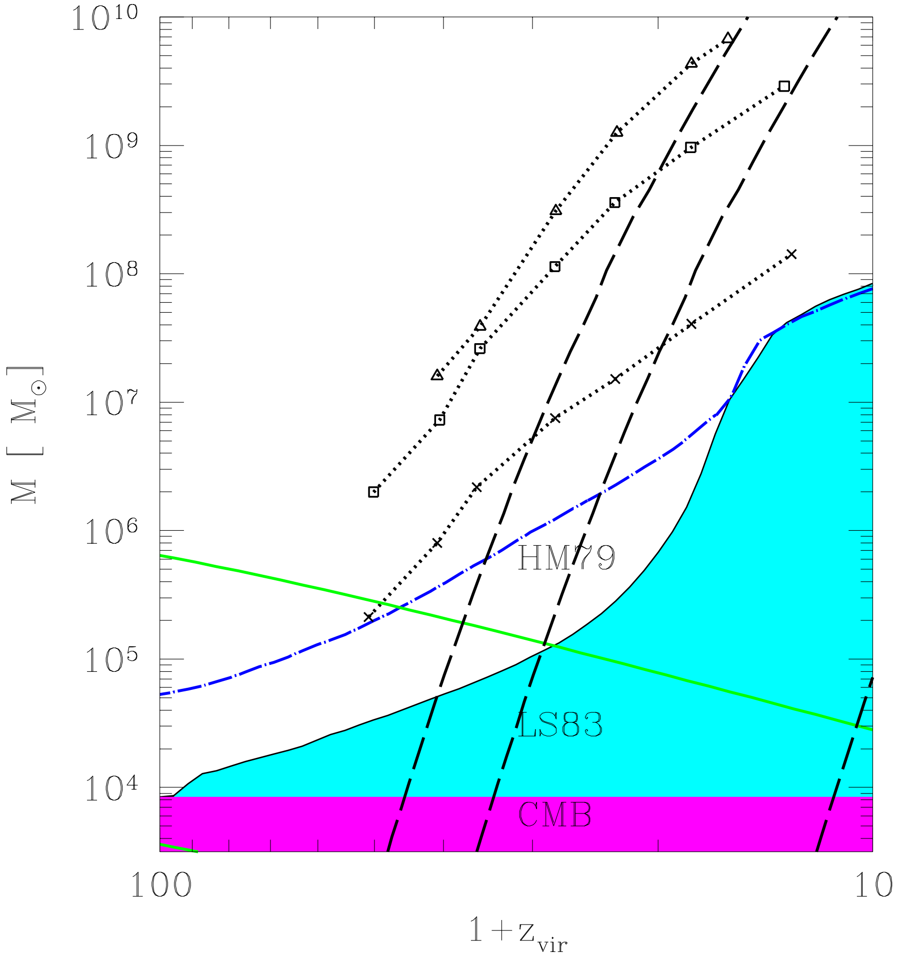

Figure 2.12

Total (baryonic and dark matter) collapsed mass vs. redshift. The horizontal dark shaded region depicts the mass scale for which the virial temperature equals the CMB temperature. The light shaded area (labeled LS83) represents the domain of parameters for which structures cannot collapse. This curve is computed assuming a spherical collapse model as in Tegmark et al. (1997), except we use the Lepp & Shull (1983) H_2 cooling function. Only above the light shaded area are structures believed to be able to collapse and cool via H_2. The dotted lines show M_{200} from our 4σ128S (crosses), 4σ512S (squares) and 4σ1024S (triangles) runs. The three dashed upward sloping lines depict the collapse redshift given by linear theory for the standard CDM spectrum scaled appropriately for 1σ, 3σ, and 4σ perturbations. The gray solid downward sloping line represents the Jeans mass at $18\pi^2$ times the background density. The dot–dashed line is the original delimiting line computed by Tegmark et al. based on a modified form of the Hollenbach and McKee (1979) H_2 cooling function.

Figure 2.12 is analogous to Figure 6 of Tegmark et al. (1997) with our numerical results superimposed. The dotted lines are found by adding up all the mass in the 3σ simulations within spherical shells on the sub grid in which the mean enclosed overdensity is 200. The collapse redshift agrees reasonably well with the predictions of linear theory, represented by the two dashed upward sloping lines. The use of different cooling functions has a very strong influence on the mass that can collapse, as evidenced by the difference in the two regions labeled HM79 (the Tegmark et al. result) and

LS83 (our result). However, we note that although the quantitative results are very different, the shape for these two different $M_c(z)$ curves is rather similar at redshifts $30 < z < 100$. Their slope is consistent with $M_c \propto (1+z)^{-3/2}$, indicating a constant virial temperature since $T_{vir} \propto M^{2/3}(1+z)$. For the case in Tegmark et al. , the virial temperature in that redshift interval ($30 < z < 100$) is approximately 1000 K. A constant virial temperature, in turn, implies a constant final H_2 fraction given by equation (2.6) which yields $f_{H_2} \sim 5 \times 10^{-4}$ for $T_{vir} \sim 1000$ K. Comparing the cooling time scale to the dynamical time, they further argued that this H_2 fraction represents a universal value for which, if exceeded, the cloud will collapse at the free fall rate. This argument depends strongly on which cooling function is assumed. Using the Lepp and Shull H_2 cooling function, we find that the minimum virial temperature needed to produce enough molecules so that the gas can cool faster than its dynamical time is ~ 200 K for redshifts > 30. This is five times smaller than the value derived from the modified Hollenbach and McKee (1979) cooling function used by Tegmark et al. (1997). This smaller minimum virial temperature for the Lepp and Shull cooling function translates to a critical H_2 fraction of only $\sim 3 \times 10^{-5}$. In our simulations, we find that the radius at which the baryonic overdensity exceeds the DM overdensity (see Figure 2.5) is coincident with the radius at which the fractional abundance of H_2 molecules exceeds $\sim 5 \times 10^{-4}$. It is therefore a coincidence that we recover the same critical H_2 fraction computed by Tegmark et al. (1997), although we used the Lepp and Shull cooling function in our simulations.

2.4 DISCUSSION AND SUMMARY

We have performed several three–dimensional numerical simulations of the first bound objects to form in a CDM model from high σ fluctuations. In addition to evolving the dark and baryonic matter components, we have also solved a reaction network of kinetic equations for the chemistry important to the production of hydrogen molecules. As these objects form prior to the onset of the metagalactic UV background we do not need to consider it. The coupled system of chemical reactions and radiative cooling have been solved self–consistently, without recourse to any equilibrium or other simplifying assumptions. The accurate modeling of non–equilibrium cooling is crucial in determining the abundance of hydrogen molecules that form in the cores of collapsed objects. A range of baryonic mass scales $10^3 - 10^8$ $M_\odot$ (set by the range of box sizes) and formation epochs $15 \lesssim z \lesssim 70$ (set by both the mass scale and the normalization σ) have been investigated in this chapter. The baryonic gas evolves to a complex network of sheets, filaments and knots with typical baryonic overdensities in the filaments of roughly an order of magnitude lower than at their intersections where $\rho/\overline{\rho} > 200$. At all epochs and mass scales covered in our simulations, the heated gas in the filaments have characteristic temperatures that are typically a few times lower than in the spherical knots. Although we find the abundance of hydrogen molecules is enhanced throughout all the overdense or collapsed structures, the lower densities and temperatures of the filaments result in the lower fractional abundances of $n_{H2}/n_H \lesssim 5 \times 10^{-5}$ along the filamentary structures as compared to typical concentrations of $\gtrsim 5 \times 10^{-4}$ in the spherical knots at the intersections of the filaments. This is understood from the analytical H_2 fraction evolution given in equation (2.6) which implies that hydrogen molecules form at slower rates in gas with lower initial temperatures and baryon densities. Since the H_2 cooling timescale in the low–density limit is proportional to $1/(n_H f_{H_2})$, it is clear why significant cooling is observed only at the cores of the highest density spheroidal structures, and not along the filaments. On the other hand, most of the volume in the simulations consists of expanding underdense voids. In these regions, the H_2 fraction equals the primordial background value of $\sim 3 \times 10^{-6}$ since the densities and temperatures there are too low to further produce H_2 .

Our numerical results confirm the analytical reasoning of Abel (1995) and Tegmark et al. (1997) that the molecular hydrogen fraction formed in structures at high redshifts arises initially solely through the residual free electrons left over from the incomplete recombination of the universe. Furthermore, we confirm the rule of thumb derived by Tegmark et al. that can be stated as: "Once the H_2 fraction is $\gtrsim 5 \times 10^{-4}$ in a spherical primordial gas cloud and the gas temperature is well above 100 K, the gas will be able to cool on timescales $\lesssim$ its dynamical one."

We have not observed hydrogen molecules to trigger the initial collapse of perturbations at high redshifts. The adiabatically compressed core densities and temperatures in the initial phases of collapse are not high enough for the chemistry to generate a large abundance of hydrogen molecules. The gas therefore cannot cool before it collapses gravitationally and shock heats to temperatures greater than a few hundred degrees Kelvin. Our results thus confirm the conclusions of Haiman et al. (1996b) who found, using one–dimensional spherical models, that radiative cooling by H_2 affects the collapse of the baryonic gas only after it has fallen into the potential well of the dark matter halos and virialized. We note that Haiman et al. (1996b) overestimated the background H_2 fraction since they underestimated the photo–dissociation of H_2^+ molecules at high redshifts through the CBR. This overestimation of the H_2 fraction in the background primordial gas, by two orders of magnitude, causes them to find that structures with virial temperatures as small as 120 K would be able to cool via H_2 . Consequently, their results on the history of H_2 formation in the virialized system cannot be correct. However, since they find that H_2 molecules cannot trigger the collapse of primordial structure despite the overestimated H_2 fraction, this result, which has been confirmed in this study, is robust. Although H_2 cooling does not trigger the collapse, it significantly influences the time evolution by keeping the temperatures in the central regions of the spherical knots to below the theoretical virial temperatures by at least a factor of a few, and thereby enhancing the baryon overdensities resulting in a gas to DM bias in the central regions.

Primordial stars can only form in the fraction of gas that is the able to cool. The fraction of cooled to total baryonic mass in the collapsed structures is only few percent. This is illustrated in Figure 2.13 which shows the ratio of cooled mass to M_{200} as a function of redshift, where M_{200} is the mass found within a spherical structure with a mean overdensity of 200. The amount of cooled gas is computed by adding up all the mass within the radius at which the temperature of the radially averaged profiles starts to decrease. The bigger the box the more gas is able to finally cool, in agreement with the analytical picture where higher virial temperatures lead to larger molecular hydrogen abundances and hence shorter cooling timescales.

Padoan et al. (1997) put forward a theory for the origin of globular clusters (GCs) in which the non-equilibrium formation of H_2 filters mass scales $\gtrsim 10^8$ $M_\odot$ out of a CDM spectrum. In their model, these clouds convert about 0.3% of their total mass into a gravitationally bound stellar system and $\sim$ 2% into halo stars. The remaining gas is enriched with metals and dispersed away from the GC by supernova explosions. Some of their assumed initial conditions are in agreement with what we find in our simulations. At redshift $z \sim 30$, a baryonic mass of about 10^3 $M_\odot$ has cooled to $T \sim 300$ K (in the 4σ128S simulation). Although our numerical experiments fail to resolve the hydrodynamics within the cooled component, this sub–Jeans mass cold cloud may well host a complex supersonic random velocity field produced by isothermal shocks which are triggered by merger events with smaller surrounding structures. The gas stays isothermal since the H_2 cooling time scale is short, as can be

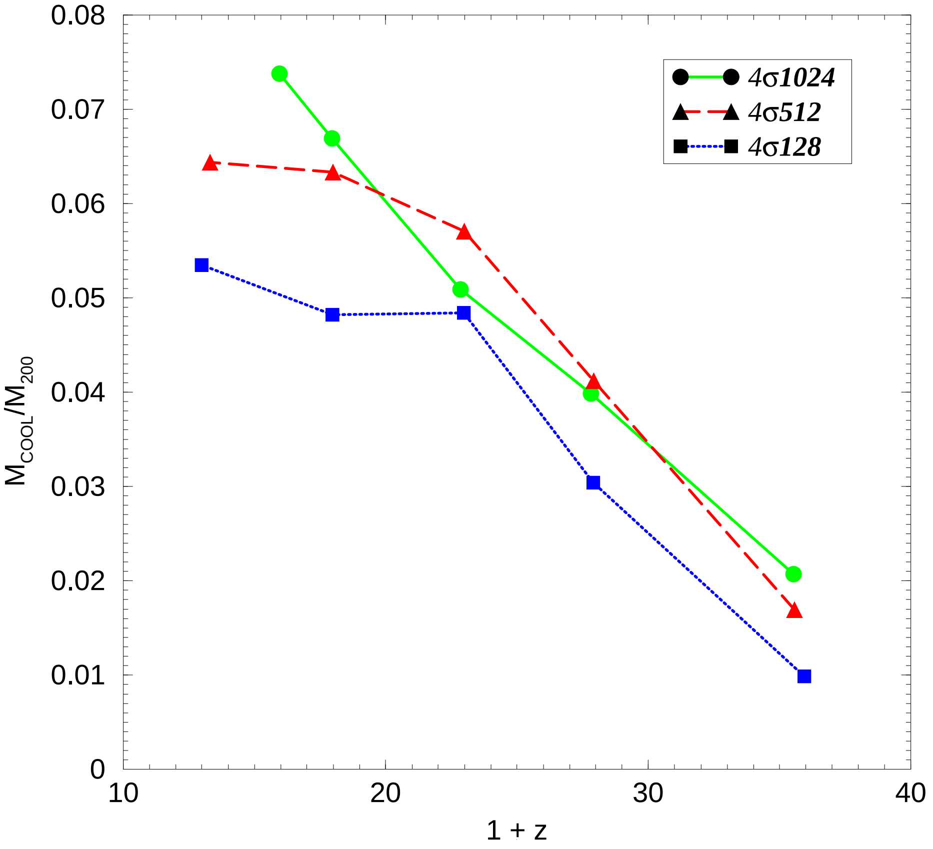

Figure 2.13

Evolution of the ratio of the cooled baryonic mass to the baryonic M_{200} is shown for the 3 different (128, 512, & 1024 kpc box size) 4σ subgrid simulations. The fraction of gas which cools approaches 5 to 8% towards the lower redshifts.

seen in Figure 2.8. Therefore, this small cloud can likely form stars through the mechanism suggested by Padoan (1995). A perturbation of total mass M contains $\Omega_B M$ baryons, of which a fraction f can cool. Defining the star formation efficiency as ϵ, the resulting mass in stars can be written as $M_s = \Omega_B f \epsilon M = 5 \times 10^{-5} M(\Omega_B/0.05)(f/0.05)(\epsilon/0.02)$. If one adopts the value of Padoan et al. (1997) for the star formation efficiency ($\epsilon = 0.02$) the mass in stars formed in the smallest simulated structures of total mass $\sim 10^6\ M_\odot$ (mas within the initial density peak of the 128 kpc box sizes) might be quite small, $\sim 50\ M_\odot$. Hence, the first stellar systems formed in hierarchical structure formation scenarios, might be much smaller than thought previously.

Finally we note that none of the investigations which have implemented a self–consistent treatment of the H_2 chemistry and cooling with the hydrodynamics of collapsing structures (*ie.* Anninos & Norman, 1996; Haiman et al. 1996; this work; Abel et al. 1998) have formed baryonic overdensities greater than 10^5. For some of these studies, this can perhaps be attributed to the lack of numerical resolution. However, we would like to stress that currently no self–consistent model of primordial star formation exists. In the following chapter we present similar simulations employing the Berger and Colella (1989) adapted mesh refinement (AMR) scheme that provides dramatic improvements for the covered dynamic range of both mass and length scales.

Chapter 3

Fragmentation of Primordial Molecular Clouds

ABSTRACT

Many questions in physical cosmology regarding the thermal history of the intergalactic medium, chemical enrichment, reionization, etc. are thought to be intimately related to the nature and evolution of pregalactic structure. In particular the efficiency of primordial star formation and the primordial IMF are of special interest. We present results from high resolution three–dimensional adaptive mesh refinement simulations that follow the collapse of primordial molecular clouds and their subsequent fragmentation within a cosmologically representative volume. Comoving scales from 128 kpc down to 0.5 pc are followed accurately. Dark matter dynamics, hydrodynamics and all relevant chemical and radiative processes (cooling) are followed self-consistently for a cluster normalized CDM structure formation model. Primordial molecular clouds with $\sim 10^5$ solar masses are assembled by mergers of multiple objects that have formed hydrogen molecules in the gas phase with a fractional abundance of $\lesssim 10^{-4}$. As the subclumps merge cooling decreases the temperature to $\sim$ 200 Kelvin in multiple "cold pockets" of the merger product. Within these cold pockets, quasi–hydrostatically contracting cores with masses $\sim 100\ M_\odot$ and number densities $\gtrsim 10^5\ \mathrm{cm}^{-3}$ are found. We find that less than 1% of the primordial gas in such small scale structures cools and collapses to sufficiently high densities to be available for primordial star formation. Our results constrain various scenarios discussed in the literature. We conclude that the very first smallest objects are unlikely to form of very massive objects, or massive black holes. Also fragmentation of a large fraction of baryons into brown dwarfs or Jupiter size fragments within the smallest first structures, seems very unlikely. Furthermore, it is worthwhile to note that this study achieved the highest dynamic range covered by structured adaptive mesh techniques in cosmological hydrodynamics to date.

In this *Chapter* we present first results from three–dimensional adaptive mesh cosmological hydrodynamics following the collapse and fragmentation of the very first objects formed in hierarchical, CDM–type models of structure formation. With an effective dynamical range of 262,144 the numerical simulations presented achieve $\sim$ 1000 times more dynamic range than the results presented in the previous chapter (refered to as AANZ98 hereafter).

3.1 SIMULATIONS

The three dimensional adaptive mesh refinement calculations presented here use for the hydrodynamic portion an algorithm very similar to the one described by Berger and Collela (1989). The code utilizes an adaptive hierarchy of grid patches at various levels of resolution. Each rectangular grid patch covers some region of space in its parent grid needing higher resolution, and may itself become the parent grid to an even higher resolution child grid. The general implementation of AMR places no restriction on the number of grids at a given level of refinement, or the number of levels of refinement. Additionally the dark matter is followed with methods similar to the ones presented by Couchman (1991). Furthermore, the algorithm of Anninos et al. (1997) to solve the accurate time–dependent chemistry and cooling model for primordial gas of Abel et al. (1997). Detailed description of the code are given in Bryan & Norman (1997,1998), and Norman & Bryan (1997,1998).

The simulations are initialized at redshift 100 with density perturbations of a sCDM model with $\Omega_B = 0.06$, $h = 0.5$, and $\sigma_8 = 0.7$. The abundances of the 9 chemical species (H, H^+ , H^- , He, He^+ , He^{++} , H_2 , H_2^+ , e^-) and the temperature are initialized as discussed in Anninos and Norman (1996). After a collapsing high–σ peaks has been identified in a low resolution simulation the simulations is reinitialized with multiple refinement levels on the Lagrangian volume of the collapsing structure. The mass resolution in the initial conditions within this Lagrangian volume are 0.53 $M_\odot$ in the gas and 8.96 $M_\odot$ for the dark matter component. The refinement criterium ensures the local Jeans length to be resolved by at least 4 grid zones as well as that no cell contains more than 4 times its initial mass of 0.53 $M_\odot$. We limit the refinement to 12 levels within a 64^3 top grid which translates to a maximum dynamical range of $64 \times 2^{12} = 262,144$.

3.2 RESULTS

We find that primordial molecular clouds are only formed at the intersection of filaments in agreement of the results of AANZ98. The evolution of these primordial molecular clouds is marked by frequent mergers yielding highly complex velocity and density fields within the "virial" radius. The chemo–thermal instability caused by the gas–phase production of H_2 yields multiple cold pockets on scales of roughly a tenth of the virial radius. These pockets are approximately isothermal at temperatures at $\sim$ 200 K and a few thousand times the mean density of the universe at that redshift.

3.2.1 Morphology and Dynamics

Visualizations of the gas density and temperature on two different scales at $z = 19.1$ are shown in the color plate 3.3. In the upper left panel also the velocity field is shown. The 5×10^5 $M_\odot$ structure forms at the intersection of $\sim$ 10 times overdense filaments. Most of the mass accretion occurs from these filaments. The complexity of the velocity field is evident. The accretion shock is highly aspherical and of varying strength. Within the virializing object cooled regions are also dense. Multiple shocks are evident within the accretion shock. At a 10 times smaller scale (right panels) far within the virialized structure one fragment becomes visible[1]. This $\gtrsim 10^6$ times overdense fragment with a mass of $\sim 200\ M_\odot$ is formed due the Bonnor–Ebert instability of the surrounding close to isothermal cool "pocket" of gas at $T \sim 200$ K.

---

[1] Note that the smallest resolution element (0.02 pc) in the simulations is still 1600 times smaller than the slice shown in the right panels.

3.2.2 Formation of the First Objects

To illustrate the physical mechanisms at work during the formation of the first cosmological object in our simulation volume we show various physical quantities at the point of largest gas density as a function redshift in Figure 3.1. In panel d) the evolution of the dark matter and baryonic density with redhsift are shown. Clearly before the virialized object has reached a mass of $\sim 10^5\ M_\odot$ the dark matter collapsed to densities $\sim 10^3$ times larger than the baryons. This is due to the finite gas pressure of the baryons. Down to redhsift ~ 23 the gas evolves adiabatically and the central temperature and densities are set by the mass of the virialized objects.

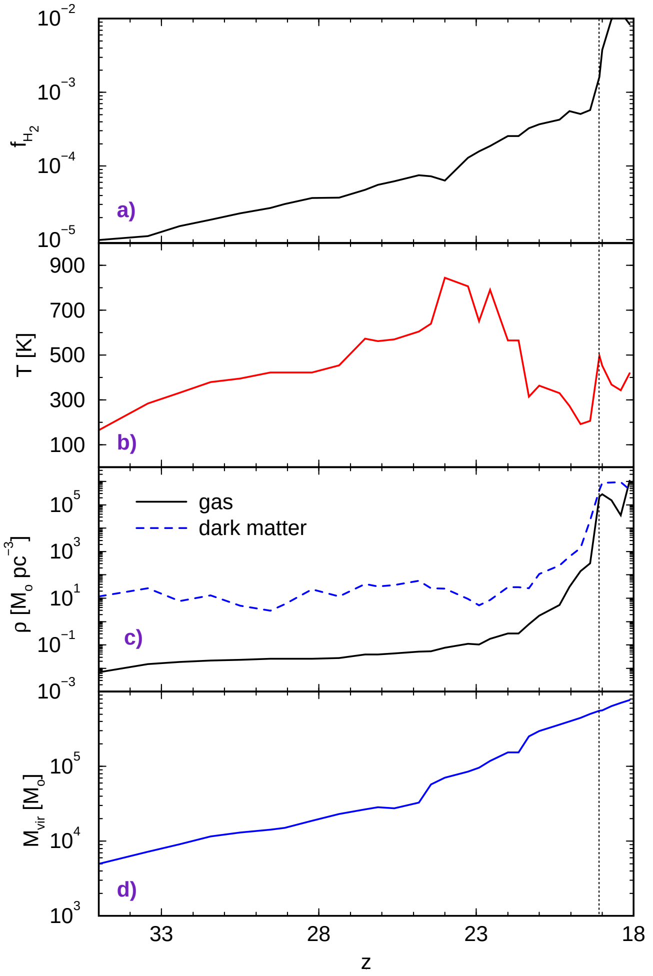

Figure 3.1

Various physical quantities at the point with the largest baryon density found in the simulation volume as function of redshift. Panel a) and b) give the mass fraction of hydrogen molecules and temperature, respectively. In panel c) the gas (solid line) and dark matter densities (dashed line) are shown. Clearly the finite gas pressure prevents baryons from clumping as much as the dark matter at redshifts $\gtrsim 23$. The bottom panel d) shows the evolution of the virialized gas mass which contains the largest peak in the baryon density. The vertical line at $z = 19.1$ indicates where the code stoped to refine and does not resolve the evolution further.

At the point where the H_2 fraction exceeds a few times 10^{-4} cooling becomes important and the central temperature decreases and the gas can settle deeper into the potential well. These results agree well with the findings of AANZ98. Therefore we kindly refer the reader to the previous chapter for a more detailed discussion. At $z = 19.1$ the maximum gas density in the simulations exceeds 10^7 cm^{-3}. At this density 3–body formation of hydrogen molecules will become dominant (see Palla et al. 1983). Eventually then the assumption of optical thin cooling will break down and radiative transfer effects will need to be included for a realistic simulation. Therefore, only simulation results at and above this redshift will be discussed. It is worthwhile to note that the simulations presented here are *not* resolution but physics limited.

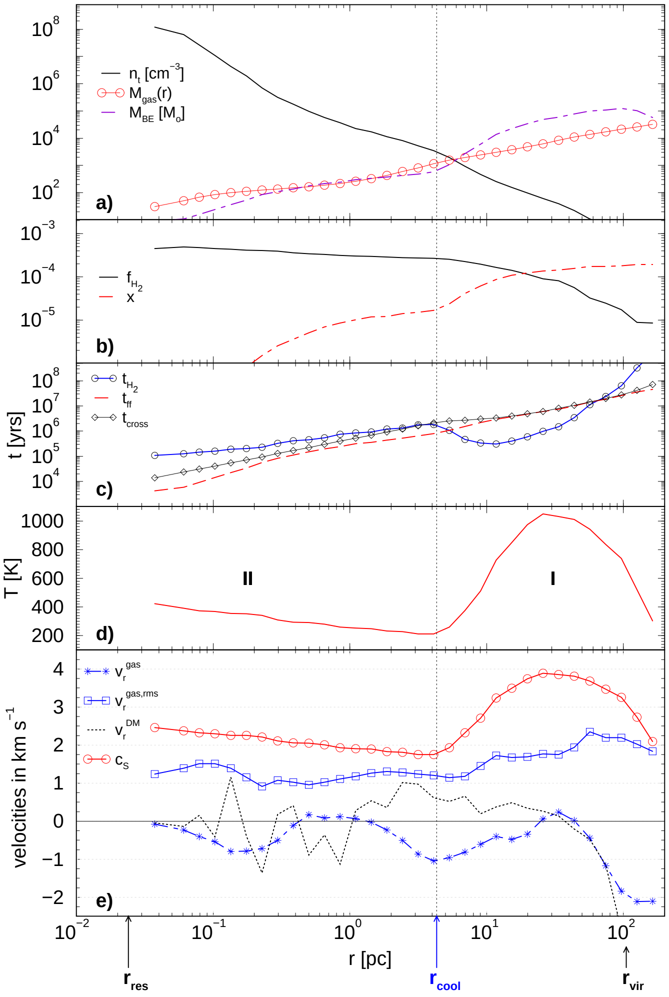

Figure 3.2

Spherically averaged mass weighted profiles around the baryon density peak shortly before a well defined fragment forms (z=19.1). Panel a) shows the baryonic number density, enclosed gas mass in solar mass, and the local Bonnor–Ebert mass ($\approx 300\ M_\odot T_K^{1.5}/\sqrt{n}$). Panel b) plots the molecular hydrogen number fraction f_{H_2} and the free electron number fraction x. The H_2 cooling time t_{H_2}, the time it takes a sound wave to travel to the center, t_{cross}, and the free–fall time $t_{ff} = [3\pi/(32G\rho)]^{1/2}$ are given in panel c). Panel d) gives the temperature in Kelvin as a function of radius. The bottom panel gives the local sound speed, c_s (solid line with circles), the rms radial velocities of the dark matter (dashed line) and the gas (dashed line with asterisks) as well as the rms gas velocity (solid line with square symbols). The vertical dotted line indicates the cooling radius ($\sim 5pc$). The virial radius of the $5.6 \times 10^6\ M_\odot$ halo is 106 pc . The cell size on the finest grid corresponds to 0.024 pc . Note that the simulation box size corresponds to 6.4 proper kpc.

The increase in dynamic range of a factor of ~ 1000 of the simulations presented here as compared to AANZ98 allow us to also investigate the detailed morphology of the first objects.

3.2.3 Profiles

Despite the complex structure of the primordial molecular clouds much of their physics can be understood from spherical profiles of the physical quantities. Figure 3.2 shows various mass weighted, spherically averages of hydrodynamic and diagnostic quantities around the densest cell found in the simulation at redshift 19.1. In panel c) we indicate two distinct regions. Region I) ranges from the virial radius to $r_{cool} \sim 5$ pc , the radius at which the infalling material has cooled down to $T \sim 200$ K. For most of this region the H_2 cooling time t_{H2} is shorter than the free–fall time, $t_{ff} = [3\pi/(32G\rho)]^{1/2}$, as is illustrated in panel b) of Figure 3.2. The H_2 number fraction rises from 7×10^{-6} to 2×10^{-4} as the free electron fraction drops from 2×10^{-4} to 2×10^{-5} (panel a). At r_{cool} the free–fall time becomes smaller than the cooling time. Also at r_{cool} the time it takes a sound wave to travel to the center, $t_{cross} = r/c_s = 7.6 \times 10^6 r_{pc}/\sqrt{T_K}$ yrs , becomes shorter than the cooling time. This suggests that the cooled region is contracting quasi–hydrostatically on the cooling time scale, which approaches its constant high–density value at small radii[2]. This constant cooling time of $\sim 10^5$ years set the time scale of the evolution of the fragment until it can turn fully molecular via three body associations.

From the time scales one would conclude that below r_{cool} the gas should evolve quasi–hydrostatically on the cooling time scale. This is, however, not strictly true. It turns out that centrifugal forces play an important role in the collapse. As can be directly seen from the radial gas velocity (dashed line with asterisks) in panel e) of Figure 3.2.

3.3 DISCUSSION

Multiple interesting features of the collapsing and fragmenting "primordial molecular cloud" are identified. Most notably is the fact of the existence of an initially quasi–hydrostatically contracting core of $\sim 100\ M_\odot$ which becomes Bonnor–Ebert unstable. Within this core the number densities increase from 10^5 to 10^8 cm^{-3}. For densities $\gtrsim 10^6$ cm^{-3}, however, three–body formation of H_2 becomes the dominant formation mechanism transforming all hydrogen into its molecular form (Palla et al. 1983). Our chemical reaction network does not include this reaction and the solution cannot be correct at $r \lesssim 0.1$ pc . The most interesting effect of the tree–body reaction is that it will increase the cooling rate by a factor $\sim 10^3$ leading to a further dramatic density enhancement within the core. This will decrease the dynamical timescales to $\ll 100$ years effectively "decoupling" the evolution of the fragment from the evolution of its "host primordial molecular cloud". Silk (1983) has argued that (due the enhanced cooling from the 3–body produced H_2) fragmentation of this core might continue until individual fragments are opacity limited (i.e. they become opaque to their cooling radiation). Verifying this possibility will have to await yet higher resolution simulations including the physics of the radiative transfer of the cooling radiation. However, only the gas in the $\sim 100\ M_\odot$ cores can participate in population III star formation.

---

[2] This effect is due to the transition from non-LTE to LTE populations of the H_2 rotational/vibrational states (e.g. Lepp and Shull 1983).

If it were to form an open star cluster with 100% efficiency about 6×10^{63} UV photons would be liberated during the average life time of massive star ($\sim 5 \times 10^7$ years). This is about hundred times more than the $\sim 4 \times 10^{61}$ hydrogen atoms within the virial radius. However, the average recombination time $(nk_{rec})^{-1} \sim 5 \times 10^5$ years within the virial radius is a factor 10 less than the average lifetime of a massive star. Hence, very small or zero UV escape fractions for these objects are plausible. However, the first supernovae will severly change the subsequent hydrodynamic and chemical evolution as well as the star formation history of these objects. More detailed understanding of the role of such local feedback will have to await yet more detailed simulations. Although, one might ask whether all the non–linear physics of star formation and feedback within these objects could ever be modeled in sufficient detail to make reliable predictions on their star formation history, etc.

3.4 CONCLUSIONS

We have reported first results from an ongoing project that studies the physics of fragmentation and primordial star formation in the cosmological context. The discussed results clearly illustrate the advantages and power of structured adaptive mesh refinement cosmological hydrodynamic methods to cover a wide range of mass, length and timescales reliably. All findings of AANZ98 are confirmed in this study. Among other things, these are that 1) a significant number fraction of hydrogen molecules is only found in structures at the intersection of filaments 2) only a few percent of the gas in a virialized halo are cooled to $T \ll T_{vir}$.

The improvement of a factor ~ 1000 in resolution over AANZ98 has given new insights in the details of the fragmentation process and constraints on the possible nature of the first structures: 1) Only $\lesssim 1\%$ of the baryons within a virialized object can participate in population III star formation. 2) The formation of super massive black holes or very massive objects in small halos seem very unlikely. 3) If the gas were able to fragment further through 3–body and/or opacity limited fragmentation only a small fraction of the gas will be converted into small mass objects. 4) The escape fraction of UV photons above the Lyman limit or in the Lyman Werner band should initially be small due to the high column densities of HI ($N_{HI} \sim 10^{23}$ cm^{-2}) and H$_2$ ($N_{H_2} \sim 10^{20}$ cm^{-2}) in the surrounding of star forming regions.

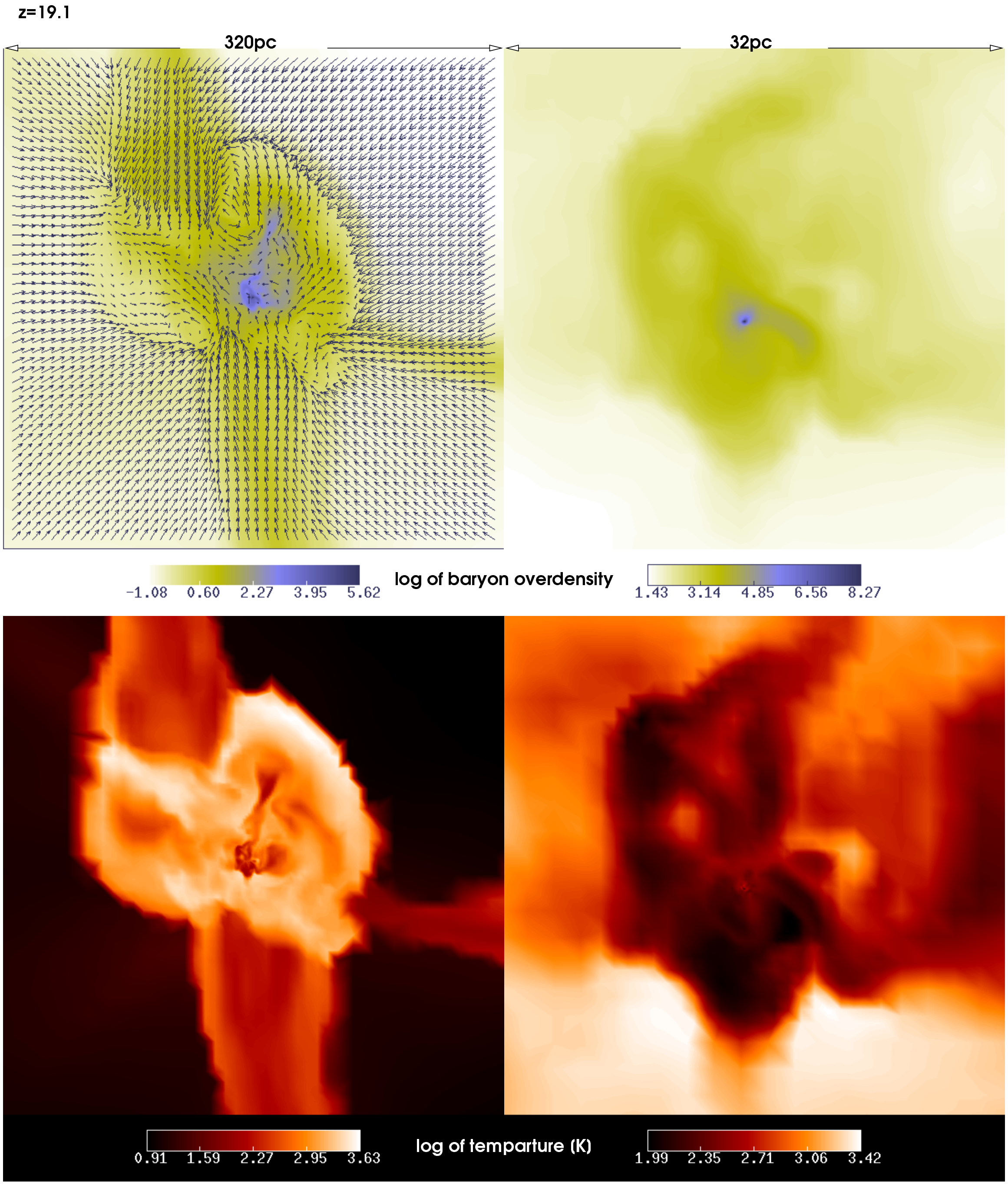

Figure 3.3

Gas density and temperature in the first cosmological objects expected to form in hierarchical structure formation scenarios at two different scales. The upper panels show the log of the baryonic overdensity in a slice through the point of highest gas density at a scale of 320 pc and 32 pc . The lower panels give the corresponding plots of the log of the gas temperature. Additionally the velocity field is also visualized in the upper left panel.

Chapter 4

First Structure Formation with Cosmic Strings + HDM?

4.1 Introduction

One of the more interesting unknowns in cosmology is what happened during the "dark ages", the period of time between the last scattering of the background radiation photons ($z \sim 10^3$), and the formation of the first objects we see, QSO's ($z \sim 5$). As observational techniques improve, we are able to examine objects in the universe at earlier and earlier cosmological epochs (cf. Wampler et al. 1996, Abraham et al. 1996, and references therein). There is strong evidence that objects the size of very large present-day galaxies existed at $z \sim 4$. The plethora of early objects found suggest that the dark ages were not completely quiescent. However the dark ages could not have been too active a period since the spectrum of the Cosmic Microwave Background Radiation (CMBR), being extremely close to a blackbody spectrum, precludes the presence of a large amount of hot gas ($\gg 10^3$K) at these early times. This leaves the possibility of small sub-galactic objects, with small virial temperatures, being formed at very early times, $z \gg 5$.

Most inflationary models for the origin of inhomogeneities in the universe predict that the primordial density field will be Gaussian random noise with a nearly scale-invariant Harrison-Zel'dovich spectrum. The shape of the spectrum combined with the Gaussian statistics cause object formation to turn on fairly rapidly with very few precursor objects. In contrast, the non-Gaussian nature of inhomogeneities seeded by topological defects allow for a much greater number of precursor objects of a given mass to collapse long before the rms fluctuation on that mass scale has gone non-linear. Such precursor objects may play an important role in early star formation, producing metals to increase the efficiency of cooling in subsequent objects, and perhaps even triggering star-bursts via the shock waves produced by supernovae.

In the cosmic string model, these precursor objects can form around the wakes of cosmic strings which move through the primordial gas at all epochs (see Vilenkin and Shellard 1994 for a review of cosmic strings). It has been argued that star formation can take place in these wakes as early as $z \sim 10^2$ (Rees 1986, Hara 1987, Hara 1996a) and that one might form black holes as well (Hogan 1984, Hara et al. 1996b). However the analysis which has led to these conclusions has not been sufficiently detailed to determine convincingly how, when, and whether these events occur. In this chapter we examine some of these scenarios with hydrodynamical simulations. In particular we look at the most easily posed problem of a single cosmic string wake in a flat universe with hot dark matter (HDM). We emphasize at the outset that our conclusions do not apply to wakes in a universe with cold dark mater (CDM), or one with a mixture (MDM), or a universe without non-baryonic dark matter (so called BDM). We are also only considering the wakes *before* the neutrinos begin to collapse. Here we do not consider the collapse of the neutrinos themselves which will happen after the events we describe take place. There is ample literature on this subject (Stebbins et al. 1987; Brandenberger, Kaiser, & Turok 1987; Bertschinger & Watts, 1988; Scherrer, Melott, & Bertschinger 1989; Perivolaropolous, Brandenberger, & Stebbins 1990; Colombi 1993; Zanchin, Lima, & Brandenberger 1996, Moessner and Brandenberger 1997, Sornborger 1997).

Of course it is difficult to demonstrate, using the hydrodynamical simulation techniques available today, the nature of star formation in a given cosmological scenario. However we are attempting the easier task of determining where stars *do not* form. In the cosmic string + HDM scenario, just after recombination, the gas is smoothly distributed since small scale perturbations are damped by photon diffusion (Silk damping) while the HDM is smoothly distributed because of it's large velocity dispersion (i.e. damping due to free-streaming). Thus in this scenario we can hope to resolve all relevant scales in the problem, or at least before things collapse too much. Clearly stars cannot form unless the gas density grows enormously over the ambient density. One might expect this to happen due to a cooling instability. However, if the gas does not undergo an instability leading to very large over-densities, then we can be fairly certain that stars will not form in that region. Employing the comprehensive non–equilibrium cooling and chemistry model of Abel et al. 1997a, our study implements the details of molecular hydrogen formation and cooling accurately. Since our results indicate that instabilities generally do not occur, we do not need to worry about secondary effects which may be produced by star formation.

To study this problem we have used a version of ZEUS–2D (Stone and Norman 1992), a Eulerian finite difference hydrodynamics code, that was modified to simulate nonequilibrium reactive flows in cosmological sheets by Anninos & Norman (1996). The code incorporates the methods developed by Anninos et al. (1997), and the comprehensive 9-species chemistry model of Abel et al. (1997). For this study we have further modified the code to account for the net force imparted on the baryons from Compton scattering with the CMBR), the so called *Compton drag.*

In the next section we presage the numerical results and give analytical arguments why a cooling instability is not found in the cosmic string + HDM model. Then we will describe our numerical methods and results in section 4.3. We refer the interested reader to our **WWW page** [1] that also shows visualizations and movies of the 2–D simulations. Section 4.6 gives a brief summary of our results and discusses the implications for the cosmic string + HDM model.

4.2 ANALYTICAL ARGUMENTS

In this section we present some simple analytical arguments on the evolution of baryonic wakes. The velocity perturbations in the primordial gas induced by a moving string will cause the baryons to shock heat at the position of the string's world sheet. For a "planar string" the velocity perturbations show reflection symmetry along the world sheet. Hence the evolution of the baryons will show the same symmetry unless hydrodynamic or thermo–gravitational instabilities affect the flow.

Throughout this chapter we assume a hot dark matter component that fills the universe with $\Omega_{HDM} + \Omega_B = 1$. The velocity dispersion of particles that were thermally produced in the early universe is given by (Kolb & Turner, 1990)

$$\langle v_{HDM}(z)\rangle \approx 23\ \mathrm{km/s}\left(\frac{m_\nu}{30\ \mathrm{eV}}\right)^{-\frac{4}{3}}\left(\frac{1+z}{10}\right), \tag{4.1}$$

where m_ν denotes the mass of the HDM particle. Since we are interested in early structure formation ($z \gg 5$), we can safely assume that the HDM component is distributed homogeneously and is not therefore dynamically important. Hence, Ω_{HDM} will only enter in the evaluation of the cosmological scale factor $a(t)$.

The trajectory of a gas particle (characterized by the comoving length $\triangle_Q$) after recombination and outside of the shocked region is the same as for a collisionless particle, which for a flat universe is given by (Stebbins et al. 1987)

---

[1] `http://lca.ncsa.uiuc.edu/~abel/Strings/`

$$\triangle_Q(z) = \frac{1}{(p_+ + p_-)}\frac{v_{\rm kick}}{H_0\sqrt{\Omega_0}} \times \tag{4.2}$$

$$\left[\frac{(1+z_{\rm kick})^{p_+-1/2}}{(1+z)^{p_+}} - \frac{(1+z)^{p_-}}{(1+z_{\rm kick})^{p_-+1/2}}\right], \tag{4.3}$$

where

$$p_+ = \frac{1}{4}\left(\sqrt{1+24\Omega_B/\Omega_0}-1\right), \tag{4.4}$$

$$p_- = \frac{1}{4}\left(\sqrt{1+24\Omega_B/\Omega_0}+1\right) \tag{4.5}$$

where Ω_B, $v_{\rm kick}$, and $z_{\rm kick}$ denote the fraction of closure density in baryons, the initial kick velocity, and the kick redshift respectively. Since this result was derived using the Zel'dovich approximation we know it is exact in one dimension. Taking the time derivative, we find for the evolution of the peculiar velocity of the gas particles with respect to the cosmological frame, $u = (1+z)^{-1}d\triangle_Q/dt$. In Figure 4.1 we show the evolution of the velocity perturbation induced by a string at redshift 900 as a function of both redshift and Ω_B for the case of a flat background universe. We see that for all cases with $\Omega_B \lesssim 0.5$, the infall velocity will be smaller at the present time than the initial kick velocity, illustrating that the wake was not able to acquire high enough surface densities to overcome the "drag" from the Hubble expansion.

From the Rankine–Hugoniot relations (Rankine 1870, Hugoniot 1889) we know that a strong adiabatic shock in an ideal gas will travel outwards with a fraction $\frac{1}{2}(\gamma-1)$ ($=1/3$ for the mono–atomic ideal gas with adiabatic index $\gamma = 5/3$) of the infall velocity. The maximum velocity difference at the shock is given by the peculiar velocity u with respect to the cosmological frame, yielding a maximum post-shock temperature of $kT = \mu u^2/3$. The immediate post–shock density equals $(\gamma+1)/(\gamma-1)$ ($=4$ for $\gamma = 5/3$) times the pre–shock density, $\rho_w = \rho_B(\gamma+1)/(\gamma-1) = \rho_0(1+z)^3(\gamma+1)/(\gamma-1)$, where ρ_0 denotes the present mean density of baryons in the universe.

Abel (1995) and Tegmark et al. (1997) showed how one can, for a Lagrangian fluid element, integrate the kinetic rate equations of molecular hydrogen formation for applications where the collisional ionization of hydrogen atoms is unimportant, i.e. low velocity shocks with post–shock temperatures $\lesssim$ 6000 K. For redshifts $\lesssim$ 100 they find the H_2 fraction after one initial recombination time to be given by

$$f_{H_2} = 1\times10^{-3}\left(\frac{T_0}{2000\ {\rm K}}\right)^{1.53} \ln(x_0 n_H k_{\rm rec} t + 1), \tag{4.6}$$

where T_0 is the immediate post–shock temperature, x_0 the initial free electron fraction, $k_{\rm rec}$ the hydrogen recombination rate coefficient, and n_H the number density of neutral hydrogen atoms. This formula describes remarkably well the numerical results of Abel et al. 1998. For redshifts greater than 100, this solution can be used as an estimate for the absolute maximum amount of H_2 that actually forms. We see that it takes at least one initial recombination time ($t_{\rm rec} = (k_{\rm rec}x_0 n_H)^{-1}$) to form a significant abundance of H_2 . Using $x_0 = 1.2\times10^{-5}\sqrt{\Omega_0}/(h\Omega_B)$ (Peebles 1993), $k_{\rm rec} = 1.8\times10^{-10}T^{-0.65}$ cm^3 s^{-1}, and the post–shock conditions derived above, we find that the minimum time to form hydrogen molecules is given by

$$t_{\rm min} = 3.1\times10^{15}\ {\rm s}\left(\frac{v_{\rm kick}}{10\ {\rm km/s}}\right)^{1.3}\left(\frac{1+z}{100}\right)^{-3}. \tag{4.7}$$

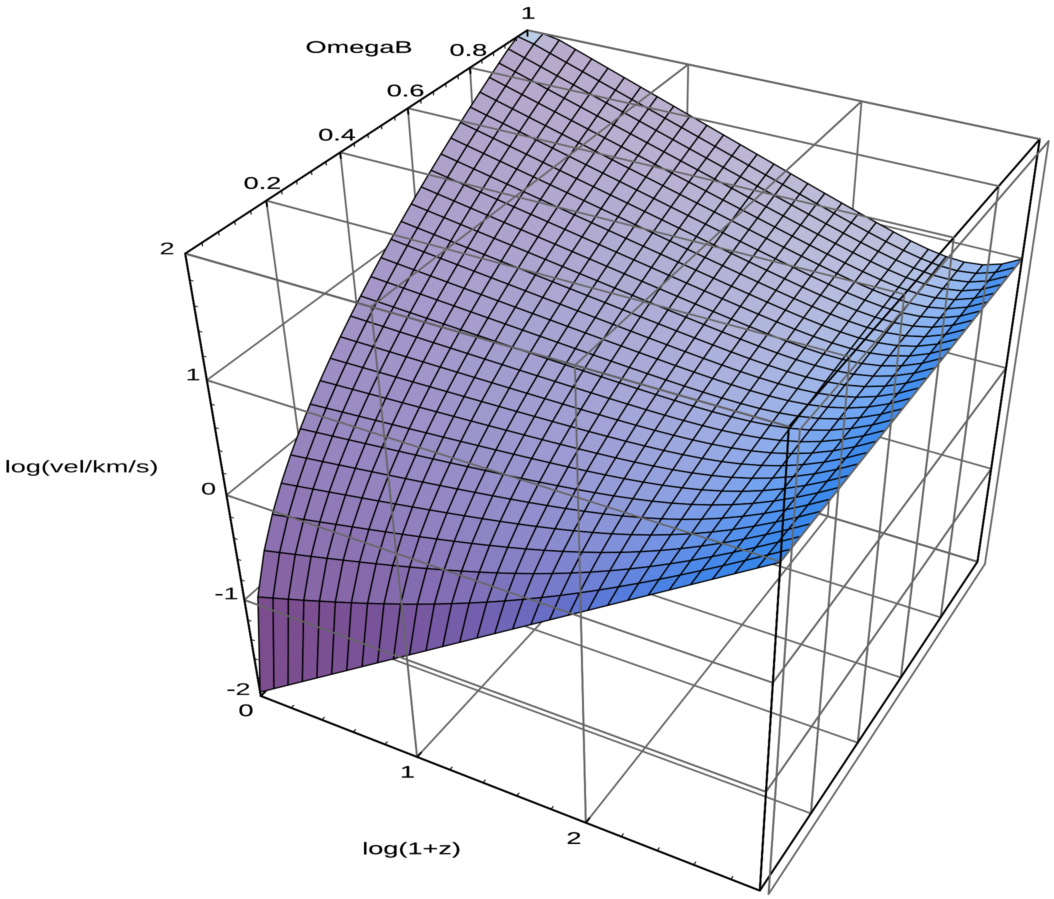

Figure 4.1

The peculiar velocity evolution for a string wake seeded at $z_{\rm kick} = 900$ and $v_{\rm kick} = 10$ km/s. The x–axis depicts the logarithm of redshift plus one, the y–axis the fraction of closure density in baryons, and the z–axis shows the logarithm of the peculiar velocity outside the shocked region. Note that for $\Omega_B = 0$ the velocity simply decays $\propto (1 + z)$ due to the cosmological expansion. Note also that changing the initial velocity kick only shifts this surface along the z-axis but does not change its shape.

Hence we see that, contrary to the case of ionizing shocks, there is a significant time lag between when the shock passes by and when enough H_2 can be formed to enable the gas to cool appreciably. At redshifts greater than 100, this time delay is longer due the photo-dissociation of the intermediaries H^- and H_2^+ by the CMBR. This is the essential reason why the radiative shock instability analyzed by Chevalier and Immamura (1982), is not found for primordial gas when the shock does not ionize the gas. However, this instability can be observed for models with $\Omega_B > 0.5$ since these models do produce shocks with velocities faster than the initial kick velocity (see Figure 4.1) and reach the part of the cooling curve that allows the instability.

In summary one does not expect to find radiative shock instabilites in realistic low Ω_B cosmologies. Furthermore, the baryonic wakes in the Cosmic String + HDM model should show infall velocites that are monotonically decreasing with time as long as $\Omega_B < 0.5$. Nevertheless small scale structure on the string as well as the details of the gas cooling might allow interesting cosmological structures to form. To investigate this latter possibility we use detailed hydrodynamical simulations which we describe in the following.

4.3 METHODS AND INITIALIZATION PARAMETERS

A numerical code with high spatial and mass resolution is required to model the hydrodynamics of a cosmic string wake and the micro–physics of chemical reactions and radiative cooling. We can achieve high dynamical ranges with the two–dimensional hydrodynamics code of Anninos and Norman (1996) which includes the 9 (H, He, H^+ , H^- , He^+ , He^{++} , H_2 , H_2^+ , and e^-) species chemistry and cooling model of Abel et al. (1997) and Anninos et al. (1997). However, we have replaced the ground state H_2^+ photo-dissociation rate of Abel et al. (1997) with the LTE rate using the equilibrium constant given by Sauval & Tatum (1984) to account for the close coupling between the CMBR and the H_2^+ molecule at high redshifts. We also account for the fact that the baryonic fluid motion at high redshift is slowed by the scattering of CMBR photons off the residual free electrons, the so called Compton Drag. This additional force can be expressed by a "drag time", $t_{\rm d} = v/\dot{v}$, where v denotes the peculiar velocity of the free electrons. For a gas with fractional ionization $x_{\rm e} = n_{\rm e}/n_{\rm t}$ and density $\rho_{\rm b} = n_{\rm t}\mu m_{\rm p}$, where $n_{\rm e}$ is the free electron number density, $n_{\rm t}$ is the total particle number density and μ is the mean molecular weight in units of proton mass $m_{\rm p}$, one may write this "drag time" as

$$t_{\rm d} = \frac{3}{4}\frac{1}{x_{\rm e}}\frac{\mu m_{\rm p}}{\sigma_{\rm T}\, c\, \rho_\gamma} = 2.4\times 10^5\,\frac{\mu}{x_{\rm e}}\left(\frac{1000\,{\rm K}}{T_\gamma}\right)^4 \ \text{years}, \tag{4.8}$$

where c is the speed of light, $\sigma_{\rm T}$ is the Thomson cross section, and T_γ is the CMBR temperature in Kelvin. Equation (4.8) is only valid in the optically thin limit, since in an optically thick medium the photons and baryons act as one fluid on scales much greater than the photon mean free path. In the code, we simply modify the updated velocity according to the first order–accurate discretization $\Delta \mathbf{v} = -\mathbf{v}\boldsymbol{\Delta}\mathbf{t}/\mathbf{t}_{\rm d}$, where Δt is the timestep defined by the minimum of the hydrodynamic Courant, gravitational free–fall, and cosmological expansion times. This will be sufficiently accurate as long as the "drag time" is much longer than the Courant time step. We start all our simulations at redshift $z = 1100$ with an initial H_2 fraction of 10^{-10} and evolve the uniform background to the "kick redshift". For the other eight species, we use the same initialization as in Anninos and Norman (1996). Furthermore, this procedure ensures that the temperature at the kick redshift $z_{\rm kick}$, is correctly derived from the balance of adiabatic expansion cooling and Compton heating.

An infinitely long and straight string traveling with a speed v_S causes a velocity boost $v_{\rm kick}$ towards the sheet given by (Stebbins et al. 1987, but see §4.4)

$$|v_{\rm kick}| = 4\pi\frac{G\mu}{c^2}v_S\left[1-\left(\frac{v_S}{c}\right)^2\right]^{-1/2}, \tag{4.9}$$

where G is the gravitational constant and μ is a mass per unit length of the string. Measurements of the CMBR anisotropy by the COBE satellite indicate that $G\mu/c^2 \lesssim 1.5\times 10^{-6}$ (Bennett, Stebbins, & Bouchet 1992, Coulson et al. 1994, Allen et al. 1996). Hence, for typical string velocities of $v_s \sim 0.8c$, one finds $v_{\rm kick} \sim 6$ km/s.

To simulate the idealized situation of a perfectly straight and infinite string, it is sufficient to perform one–dimensional simulations since the sheet traced out by the moving string is translation symmetric. Throughout this study we use a logarithmically refined grid spanning a physical domain of 0.4 comoving Mpc , with 200 zones arranged such that the zone size decreases from 18 kpc in the outermost zones to 1.4 pc in the central zone along the collapsing direction. The neighboring cells have a constant refinement ratio of $r = 1.1$. We also set $\Omega_{HDM} = 0.94$, $\Omega_B = 0.06$ and $h = 0.5$ in all the simulations.

4.4 WIGGLY STRINGS

It has been known for some time that cosmic string networks, while generally having a coherence length close to the cosmological horizon, also have structure on scales much smaller than the horizon (Vilenkin & Shellard 1995, and references therein). These wiggles do not extend to arbitrarily small scales, as they are damped by the emission of gravitational radiation. While the rms speed of cosmic string segments must be close to the speed of light, the "bulk velocity" of a long length of string, including the oscillating wiggles, can be significantly less. A particle located at a distance from the wiggly string that is greater than the extent of the wiggles would experience a net gravitational attraction greater than indicated by equation (4.9). However if one is interested in the gas dynamics in a small region around a segment of the string, a region smaller than the scale of the wiggles, the gravitational forces will be dominated by the force of that one segment and equation (4.9) will give a good indication of the velocity perturbation of the passing string.

Now we determine which regime we should be working in. For a non-wiggly string, $v_{\rm kick} \sim 10G\mu/c$ and the velocity of the strong shock wave produced would be $\frac{1}{3}$ of this, so the comoving width of the baryonic wakes is $\sim 5(1+z)\,G\mu t/c$. The comoving gravitational back-reaction scale for the strings, the scale of the smallest wiggles, is estimated to be $\sim 100(1+z)\,G\mu t/c$ (Vilenkin & Shellard 1995, and reference therein). While the two are the same order in $G\mu$, the numerical factors point to the wiggles being larger than the width of the baryonic wakes. If this is the case, then a purely planar wake might provide a sufficient description for the wakes. However, the effects of gravitational back-reaction are not completely understood and there may be other numerical factors which might cause these two scales to be more comparable. We allow for this in two ways in our simulations: first we consider kick velocities up to 20km/sec, which is greater than what would be expected for a straight piece of string, but might be more typical for the net effect of a wiggly string; secondly, in our 2–d simulations, we consider the flow onto a non-uniform string world-sheet, effectively modulating the value of $v_{\rm kick}$. More specifically we have modeled the initial flow as a potential flow, and one whose divergence $\nabla \cdot \mathbf{v}_{\rm kick}$ is non-zero on the planar string world-sheet, just as in the 1-d case. However in the 2-d case we allow the divergence to vary in one direction along the world sheet. More specifically, this divergence is drawn from a random distribution given by the positive square root of the sum of the square of two identically distributed real Gaussian random noise variables. From the perturbed surface density we compute the spatially varying velocity perturbations which show reflection symmetry about the string worldsheet. The variation along the wake was numerically captured with up to 128 grid points and the box size in this direction varied from 640 to 32 comoving kpc. We note, however, that introducing a spatially non-uniform second dimension does not lead to significantly higher overdensities than in the 1-d case.

4.5 Results

We investigate wakes from infinitely long and fast moving straight strings with different initial data: $v_{\rm kick}$ =20, 15, 10, 5 km/s, and $z_{\rm kick}$ = 900, 500, 100, and 50. We discuss here only the results from one particular one–dimensional simulation, with $z_{\rm kick}$ =900 and $v_{\rm kick}$ =20 km/s. This optimistic case of an early string with a very high kick velocity is the most promising candidate to form the first structures in the cosmic string + HDM model and, indeed, led to the highest over densities ($\sim$ 200) in all the simulated cases.

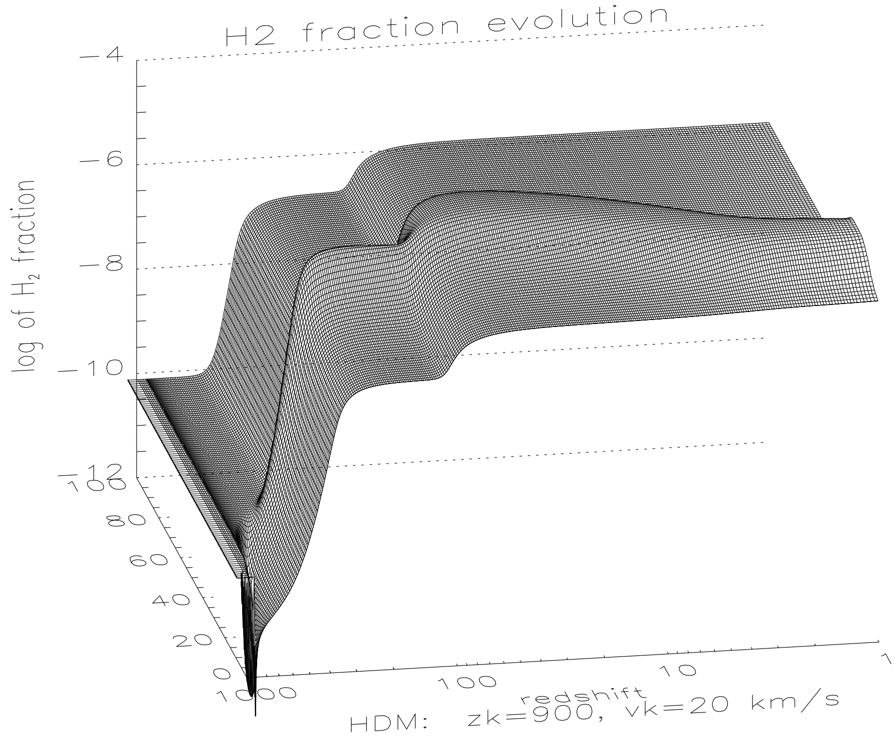

Figure 4.2

The evolution of the H_2 fraction for a string with $z_{\rm kick}$ = 900 and $v_{\rm kick}$ = 20 km/s. The x–axis depicts the redshift, the y–axis the cell number in the 1–d simulation and the z–axis shows the logarithm of the H_2 fraction.

Figure 4.2 shows, for one side of the perfectly symmetric wake, the evolution of the mass fraction of hydrogen molecules vs. cell number (distance from the string worldsheet), and also vs. redshift on the x–axis. At the kick redshift $z = 900$, a shock forms that runs outwards. Two distinct steps are evident: the first at redshift $z \sim 500$, and the second at $z \sim 120$. The plateau before the first step is an artifact of our too high initialization of H_2 and is not physical. This, however, does not influence the subsequent evolution and results. The first step is due to the H_2^+ chemistry, and occurs when the formation of H_2 molecules starts to dominate the destruction of H_2^+ compared to its photo–dissociation by the CMBR. In the shocked region, it is evident that the $v_{\rm kick} = 20$ km/s shock is initially capable of destroying some hydrogen molecules. Shortly after $z_{\rm kick} = 900$, however, the decaying infall velocity, the steadily rising H_2^+ abundance, and the increasing H_2 formation rate lead to an overall enhanced H_2 fraction. The second step is due to the H^- path, which occurs slightly earlier in the denser, shocked regions than in the background. This is easily understood from the equilibrium abundance of H^- which is given by $n_{H^-} = n_e n_H k_7/(k_{23} + k_8 n_H)$, where k_7, k_8, and k_{23} denote the reaction rates for the photo–attachment of H^- , the dissociative attachment reaction of H^- (H_2 formation), and the photo–detachment by the CMBR of H^- , respectively (the notation is taken from Abel et al. 1996). The second step originates when $k_{23} \gtrsim k_8 n_H$, and n_{H^-} is roughly proportional to $n_H n_e$ which is higher in the shocked gas than in the background, contributing to the enhanced H_2 formation rate. Another, and at first surprising, effect is that the central regions of the wake form fewer hydrogen molecules than regions further away. This is because the gas closer to the string world–sheet shocks at redshifts $z > 110$, at which H^- is still destroyed efficiently by the CMBR and H_2 cannot form. The higher density in this shocked component leads to an increased hydrogen recombination which leaves fewer free electrons as catalysts for H_2 formation at lower redshifts. Consequently, this H_2 depression in the central layers are not observed for simulations with kick redshifts $\lesssim 110$.

Compton Drag never becomes dynamically important even in the high kick velocity cases where the shock ionizes the gas. This is because the wakes do not become self–gravitating until very late redshifts. In other words, the post shock gas continues to expand with the Hubble flow and the gas shows no motion with respect to the rest frame of the background photons. Hence, there will be no net force on the baryons independent of their ionized fraction. Since the self-gravity of the gas plays little role in the evolution of the wake at early times, we should expect that inhomogeneities in the wake should have little effect since they will not be amplified.

Shapiro and Kang (1987) presented calculations of steady–state shocks of 20, 30, and 50 $\mathrm{km/s}$ occurring at redshifts 100 and 20 with and without external radiation fields. Taking their results as upper limits on the possible H_2 formation and cooling we find our simulations agree with their findings at the low redshifts and high kick velocities where they are comparable.

4.6 CONCLUSION

The Jeans mass, which is proportional to $T^{3/2} n^{-1/2}$, will for adiabatic evolution ($T \propto n^{2/3}$) scale as $M_J \propto \sqrt{n}$. Hence the collapse of a super Jeans mass cloud will eventually be halted by internal pressure forces. However, if the gas can cool the Jeans mass will decrease allowing the cloud to collapse to high densities. Efficient cooling is thus a crucial requirement for star formation.

We investigated structure formation at high redshift in the wakes of fast, long, and straight, as well as fast, long, and wiggly cosmic strings in a hot dark matter dominated universe. To see whether the conditions in such cosmic string wakes allow for primordial star formation we followed the detailed non–equilibrium primordial gas chemistry and cooling behaviour. It is found that insufficient amounts of H_2 molecules are formed, and the gas does not cool appreciably. Due to the fact that the baryonic cosmic string wakes do not become significantly self–gravitating to allow the infall velocities to exceed the initial kick velocity (see Figure 1.), we find the maximum overdensities reached in all the simulations we have carried out are $< 10^3$, corresponding to hydrogen number densities less than $\sim 1 \times 10^{-4} (\Omega_B h^2/0.025)(1+z)^3\ \mathrm{cm}^{-3}$. Thus no primordial stars can be formed in the studied wakes.

This leads us to conclude that, in the cosmic string + HDM model, one must wait for the neutrinos to collapse before anything like star formation can take place. In this work we have explicitly considered gauge (local) cosmic strings, but we expect these conclusions will apply to global cosmic strings as well. The baryonic structures considered above will be destroyed if and when they become enveloped in the collapse of the neutrinos, which will happen on much larger scales and involve much larger velocities. It has been suggested that neutrino collapse may happen as early as $z \sim 100$ (Zanchin, Lima, & Brandenberger 1996; Sornborger 1997) but other studies (Colombi 1993) find non-linear collapse only for $z \lesssim 5$. Thus it is still an unsettled issue whether cosmic strings could have brought light to the dark ages, at least in the HDM scenario.

Chapter 5

On the radiative Feedback of the first Cosmological Objects

ABSTRACT

We discuss in detail the photo–dissociation of intergalactic H$_2$ and the qualitative structure of cosmological H$_2$ photo–dissociation regions. In particular we discuss the transfer properties of photons with energies below the hydrogen Lyman Limit in the intergalactic medium prior to reionization. We also asses how a soft UV background, might influence subsequent structure formation.

5.1 INTERGALACTIC H$_2$ PHOTO–DISSOCIATION

To illustrate the physics we will first discuss an isolated source of UV photons embedded in a uniformly expanding homogeneous IGM. The relevant photo–dissociation process of H$_2$ is pre–dissociation of H$_2$ by photons in the energy range $11.1 < h\nu/\,\mathrm{eV} < 13.6$. An Einstein de–Sitter Universe is assumed throughout this chapter.

5.1.1 Level distribution of intergalactic H$_2$

To know which UV–photons will be absorbed we first need to know the rotational level distribution of the intergalactic H$_2$. The level population, N_J of a rotational state J is proportional to

$$N_J \propto (2\,J+1)\exp\left[-B_e\,J(J+1)\,hc/(k\,T)\right] \tag{5.1}$$

where the rotational constant $B_e = 60.80\ \mathrm{cm}^{-1}$ for the $X\,{}^1\Sigma_g^+$ ground state of H$_2$. In para (ortho) H$_2$ only even (odd) rotational quantum numbers (J) are allowed. From this we find for para H$_2$ that for temperatures less than 100 K the lowest rotational state is at least by an order of magnitude more abundant than the next allowed higher energy rotational state. For ortho H$_2$ the $J=3$ state is at least 10,000 times less common than the $J=1$ state for $T < 100$ K. Therefore, we can assume all intergalactic H$_2$ to be at its lowest ro–vibrational level for redshifts $z \lesssim 30$ where the molecule excitation is less than 100 K.

We assume a thermal ortho to para H$_2$ ratio of 3:1. This does not have to be the true as we explain in the following:

Most of the intergalactic H$_2$ is formed via the associative detachment reaction of H$^-$ (Lepp & Shull 1984),

$$H \;+\; H^- \;\rightarrow\; H_2^-({}^2\Sigma_u) \;\rightarrow\; H_2(v,J) \;+\; e^-. \tag{5.2}$$

This process populates preferentially highly excited vibration–rotation levels which then cascade towards the ground vibrational state by quadrupole radiative transitions. In the freeze–out process of intergalactic H$_2$ formation this must not lead to a thermal ortho to para H$_2$ ratio. Although, this ratio could be computed using the rate coefficients of Launay et al. (1991), we do not attempt this here but simply assume a thermal ortho to para H_2 ratio of 3:1.

5.1.2 Relevant Lyman–Werner Bands

All the intergalactic H_2 will be in the lowest states vibrational and rotational states of the ground electronic state. Hence only v=0 with J=0 (para) and 1 (ortho) are populated. There are now more than 70 possible Lyman Werner band transitions that can yield photo-dissociation (decay to the continuum). These are typically classified as R or P transitions depending whether the rotational quantum number changes by -1 or +1 from the electronic ground to the electronic excited state (angular momentum must change due to parity conservation). Hence, assuming that para and ortho hydrogen molecules, in their ground states, are abundant, all transitions called R(0) (i.e. $J = 0 \rightarrow J = 1$) R(1) (i.e. $J = 1 \rightarrow J = 2$) and P(1) (i.e. $J = 1 \rightarrow J = 0$) and all of these for each excited vibrational level, are possible. The above is true for Lyman and Werner Bands. For the Werner Band ($X\,^1\Sigma_g^+ - C\,^1\Pi_u$), however, there is an additional Q–branch in which $\triangle J = 0$ allowed[1]. Figure 5.1 illustrates all possible transitions from the lowest energy states of ortho and para H_2 .

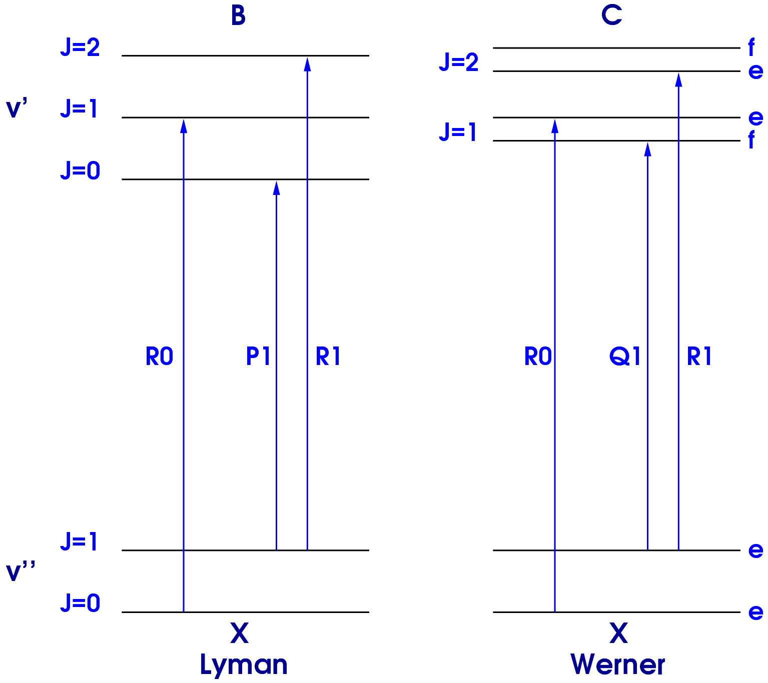

Figure 5.1

Illustration of all possible absorption lines from the lowest energy states of ortho and para H_2 .

Considering only absorption lines from the lowest ro-vibrational state of ortho and para molecular hydrogen that are below the Lyman limit of atomic hydrogen one ends up with 76 possible transitions. Their wavelengths, oscillator strengths, and dissociation fraction, are summarized in Table 5.1.2. The J–dependent dissociation fractions were taken from Abgrall et al. (1992). From their work one sees that the dissociation fractions of the Werner Q–branch (which couples to the Π^- state) are extremely small. For the R–branch, however, the f_{diss} are quite significant (especially for $v' = 3$ of the Werner band).

---

[1] this is due to the different orbital angular momentum along the internuclear axis of the two states, i.e. $\Sigma - \Pi$ for the Werner but $\Sigma - \Sigma$ for the Lyman transition (Λ doubling)

Table 5.1. Relevant Lyman Werner Bands of $X\,^1\Sigma_g^+$ H_2

	λ [Angstroem]	λ [eV]	f	A [s]	f_{diss}	Transition
1	911.9681	13.5954	1.312(-3)	7.439(8)	6.364(-1)	B19P1
2	914.3973	13.5592	2.598(-2)	1.090(9)	1.334(-3)	C5R0
3	914.6071	13.5561	1.299(-2)	1.090(9)	3.713(-3)	C5R1
4	915.4009	13.5444	1.298(-2)	1.090(9)	5.583(-6)	C5Q1
5	917.2478	13.5171	4.821(-3)	7.702(8)	6.090(-1)	B18R0
6	917.9190	13.5072	3.212(-3)	7.702(8)	6.057(-1)	B18R1
7	918.4107	13.5000	1.605(-3)	7.702(8)	6.111(-1)	B18P1
8	923.9829	13.4186	5.892(-3)	7.990(8)	6.064(-1)	B17R0
9	924.6429	13.4090	3.925(-3)	7.990(8)	6.061(-1)	B17R1
10	925.1741	13.4013	1.962(-3)	7.990(8)	6.062(-1)	B17P1
11	929.5321	13.3385	3.874(-2)	1.105(9)	2.873(-3)	C4R0
12	929.6869	13.3362	1.937(-2)	1.105(9)	5.284(-3)	C4R1
13	930.5765	13.3235	1.935(-2)	1.105(9)	2.277(-6)	C4Q1
14	931.0626	13.3165	7.186(-3)	8.301(8)	5.507(-1)	B16R0
15	931.7324	13.3070	4.787(-3)	8.301(8)	5.461(-1)	B16R1
16	932.2663	13.2993	2.392(-3)	8.301(8)	5.559(-1)	B16P1
17	938.4671	13.2115	8.732(-3)	8.640(8)	5.596(-1)	B15R0
18	939.1230	13.2022	5.817(-3)	8.640(8)	5.580(-1)	B15R1
19	939.7068	13.1940	2.907(-3)	8.640(8)	5.603(-1)	B15P1
20	946.1693	13.1039	5.472(-2)	1.121(9)	1.396(-1)	C3R0
21	946.3841	13.1009	2.735(-2)	1.121(9)	5.735(-2)	C3R1
22	947.4205	13.0866	2.733(-2)	1.121(9)	1.838(-8)	C3Q1
23	946.4251	13.1004	1.055(-2)	9.003(8)	3.481(-1)	B14R0
24	946.9797	13.0927	7.029(-3)	9.003(8)	4.497(-1)	B14R1
25	947.5134	13.0853	3.513(-3)	9.003(8)	5.397(-1)	B14P1
26	954.4127	12.9907	1.266(-2)	9.391(8)	5.097(-1)	B13R0
27	955.0655	12.9819	8.436(-3)	9.391(8)	5.072(-1)	B13R1
28	955.7080	12.9731	4.215(-3)	9.391(8)	5.111(-1)	B13P1
29	962.9778	12.8752	1.504(-2)	9.804(8)	5.199(-1)	B12R0
30	963.6071	12.8668	1.002(-2)	9.804(8)	5.084(-1)	B12R1
31	964.3096	12.8574	5.008(-3)	9.804(8)	5.233(-1)	B12P1
32	964.9836	12.8484	6.982(-2)	1.139(9)	1.599(-3)	C2R0
33	965.0642	12.8474	3.491(-2)	1.139(9)	8.201(-3)	C2R1
34	966.0954	12.8336	3.487(-2)	1.139(9)	.3205(-9)	C2Q1
35	971.9860	12.7559	1.764(-2)	1.025(9)	4.071(-1)	B11R0
36	972.6320	12.7474	1.176(-2)	1.025(9)	4.112(-1)	B11R1
37	973.3441	12.7381	5.873(-3)	1.025(9)	4.063(-1)	B11P1
38	981.4383	12.6330	2.036(-2)	1.072(9)	4.100(-1)	B10R0
39	982.0736	12.6248	1.356(-2)	1.072(9)	4.096(-1)	B10R1
40	982.8346	12.6151	6.775(-3)	1.072(9)	4.103(-1)	B10P1
41	985.6335	12.5792	7.284(-2)	1.159(9)	3.891(-4)	C1R0
42	985.6441	12.5791	3.642(-2)	1.159(9)	1.278(-3)	C1R1
43	986.7977	12.5644	3.638(-2)	1.159(9)	.2197(-9)	C1Q1
44	991.3785	12.5064	2.299(-2)	1.122(9)	4.125(-1)	B9R0
45	992.0157	12.4983	1.531(-2)	1.122(9)	4.122(-1)	B9R1
46	992.8092	12.4883	7.651(-3)	1.122(9)	4.133(-1)	B9P1
47	1001.823	12.3760	2.524(-2)	1.177(9)	3.121(-1)	B8R0
48	1002.451	12.3682	1.681(-2)	1.177(9)	3.331(-1)	B8R1
49	1003.296	12.3578	8.400(-3)	1.177(9)	3.016(-1)	B8P1

TABLE 5.1. (continued)

	λ [Angstroem]	λ [eV]	f	A [s]	f_{diss}	Transition
50	1008.498	12.2941	2.380(-2)	1.180(9)	3.680(-4)	C0R1
51	1008.551	12.2934	4.760(-2)	1.180(9)	1.353(-4)	C0R0
52	1009.770	12.2785	2.377(-2)	1.180(9)	1.218(-9)	C0Q1
53	1012.812	12.2417	2.674(-2)	1.236(9)	2.054(-1)	B7R0
54	1013.436	12.2341	1.781(-2)	1.236(9)	2.003(-1)	B7R1
55	1014.326	12.2234	8.899(-3)	1.236(9)	2.074(-1)	B7P1
56	1024.373	12.1035	2.705(-2)	1.301(9)	3.331(-2)	B6R0
57	1024.987	12.0963	1.802(-2)	1.301(9)	3.895(-2)	B6R1
58	1025.934	12.0851	9.002(-3)	1.301(9)	3.123(-2)	B6P1
59	1036.545	11.9614	2.572(-2)	1.372(9)	1.861(-2)	B5R0
60	1037.149	11.9544	1.714(-2)	1.372(9)	2.009(-2)	B5R1
61	1038.156	11.9428	8.559(-3)	1.372(9)	1.779(-2)	B5P1
62	1049.367	11.8152	2.251(-2)	1.450(9)	1.282(-3)	B4R0
63	1049.959	11.8086	1.500(-2)	1.450(9)	1.222(-3)	B4R1
64	1051.032	11.7965	7.491(-3)	1.450(9)	1.325(-3)	B4P1
65	1062.882	11.6650	1.756(-2)	1.536(9)	1.506(-4)	B3R0
66	1063.460	11.6587	1.170(-2)	1.536(9)	1.951(-4)	B3R1
67	1064.605	11.6461	5.843(-3)	1.536(9)	1.308(-4)	B3P1
68	1077.138	11.5106	1.156(-2)	1.632(9)	1.198(-5)	B2R0
69	1077.698	11.5046	7.706(-3)	1.632(9)	1.225(-5)	B2R1
70	1078.925	11.4916	3.848(-3)	1.632(9)	1.183(-5)	B2P1
71	1092.194	11.3519	5.792(-3)	1.741(9)	3.478(-7)	B1R0
72	1092.732	11.3464	3.860(-3)	1.741(9)	3.630(-7)	B1R1
73	1094.051	11.3327	1.928(-3)	1.741(9)	3.250(-7)	B1P1
74	1108.127	11.1887	1.690(-3)	1.868(9)	1.486(-6)	B0R0
75	1108.633	11.1836	1.126(-3)	1.868(9)	1.470(-6)	B0R1
76	1110.062	11.1692	5.623(-4)	1.868(9)	1.580(-6)	B0P1

Figure 5.2 gives an overview of the most relevant Lyman Werner bands for intergalactic H_2 photo–dissociation. The quantity $f_{osc} \times f_{diss}$ quantifies the contribution of an individual line to the overall photo–dissociation. Clearly photons with $h\nu \lesssim 11.9$ eV will not contribute much to the dissociation anymore. Also all Werner bands with $v' \neq 3$ do not contribute much to the dissociation rate.

Having identified the relevant micro–physics let us now turn to effects of the cosmological radiative transfer.

5.1.3 Cosmic Line Transfer

Draine and Bertoldi considered the static transfer in a homogeneous slab in which velocities (if considered at all) are turbulent and add only to the line broadening. This is perfectly correct as long as the scales over which the velocity changes are much smaller than the scale at which the optical depth becomes unity. In the cosmological case the following difference arises. Due to the Hubble expansion the relative velocity of emitter and absorber increases linearly with their distance. Or, in the reference frame of the absorber, the photons are redshifted.

For a flat universe the distance from the source at which a photon of wavelength λ_e emitted at

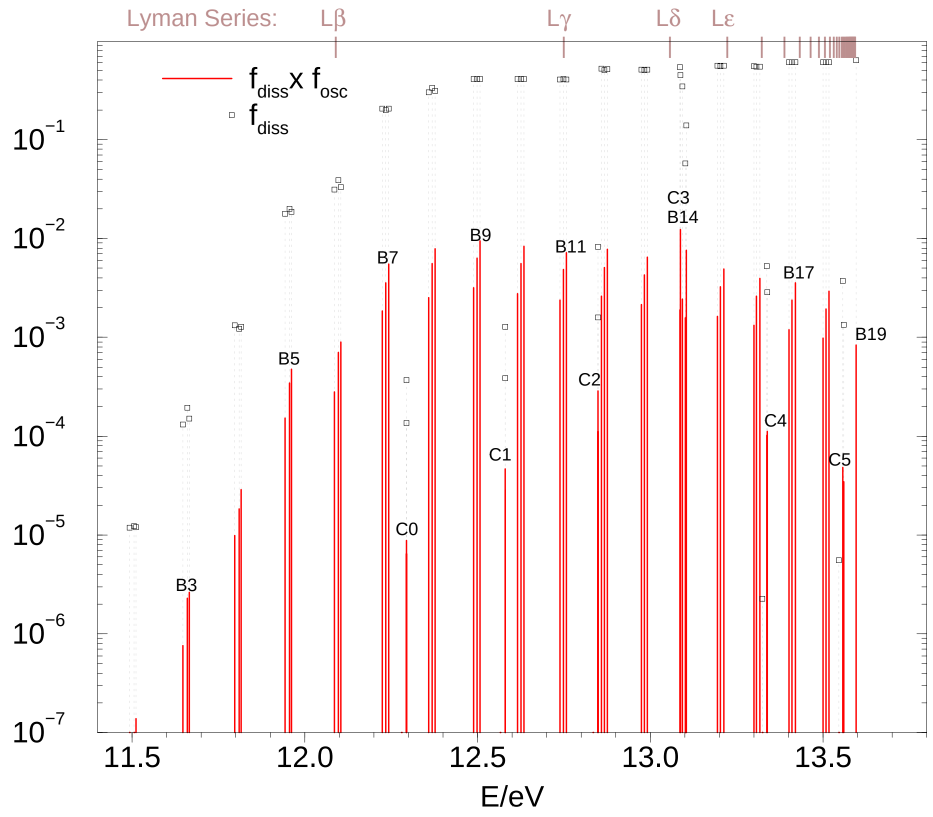

Figure 5.2

The relevant Lyman Werner bands for intergalactic H_2 photo-dissociation. The solid columns indicate the value of $f_{diss} \times f_{osc}$ and the dotted ones show the dissociation fractions. Lines of the Lyman (Werner) system are labeled by Bv' (Cv') where v' is the vibrational quantum number of the excited state. On the top x–axis we have indicated the positions of the Lyman series of atomic hydrogen.

redshift z_e is redshifted to λ is given by,

$$r = 12\,\mathrm{Mpc}\,h^{-1}\left(\frac{1+z_e}{31}\right)^{-3/2}\left(\left(\frac{\lambda}{\lambda_e}\right)^{3/2} - 1\right). \tag{5.3}$$

Hence there is a finite distance over which a photon is shifted across the width of the absorption line.[2] Self–shielding can only occur if the optical depth across this distance is greater or similar to unity. To compute this optical depth recall that the line absorption coefficient is given by,

$$\kappa(\lambda) = \sigma_{cl} f_{mn}\phi(\lambda) n = \frac{\pi e^2}{mc} f_{mn}\phi(\lambda)\, n = 2.654 \times 10^{-2} f_{mn}\phi(\lambda)\, n, \tag{5.4}$$

where f_{mn} is the oscillator strength of the considered transition, $\phi(\lambda)$, the line profile, n the number density of the absorbing material, and σ_{cl} the classical total cross section . The optical depth for absorption at redshift z in a line with f_{mn} of profile $\phi(\lambda)$ for a photon λ_e emitted at z_e is given by,

---

[2] For cold H_2 no significant absorption occurs in the Lyman Werner bands longward of 1110 Å . This is because the Lyman 0–0 P(2), P(3), P(4), etc. have very small oscillator strengths and originate from excited rotational levels that are not populated at low temperatures. Therefore, at $r \sim 4\,\mathrm{Mpc}/h$, 912 Å photons will have redshifted passed 1110 Å and the photo–dissociation rate will drop by many orders of magnitude.

$$\begin{aligned}
\tau(\lambda_e, z_e, z) &= c\int_{t_e}^{t} \kappa\left(\lambda\,(t/t_e)^{2/3}\right)\,dt && (5.5)\\
&= \frac{c}{H_0}\int_{z}^{z_e} \kappa\left(\lambda_e(1+z_e)/(1+z)\right)\,(1+z)^{-5/2}\,dz && (5.6)\\
&= \frac{\sigma_{cl} f_{nm} n_0\, c}{H_0}\int_{z}^{z_e} (1+z)^{1/2}\phi\left(\lambda_e(1+z_e)/(1+z)\right)\,dz && (5.7)\\
&= \frac{\sigma_{cl} f_{nm} n_0\, c}{(1+z_e)^{-3/2} H_0}\int_{\delta}^{1} \delta^{1/2}\phi\left(\lambda_e/\delta\right)\,d\delta, && (5.8)
\end{aligned}$$

where $\delta = (1+z)/(1+z_e)$, H_0 is the Hubble Constant, and n_0 the comoving number density (i.e. average number density today) of the absorbing material.

Absorption in the Wings

For a Lorentz line profile the integral in equation (5.8) has an analytic solution. Figure 5.3 shows a plot of this solution versus ν_e/ν_{mn} for varying δ. Interestingly it has its maximum if the emission frequency is right at the line center. This is due to the rapid $(1+z)^3$ dilution of the number density

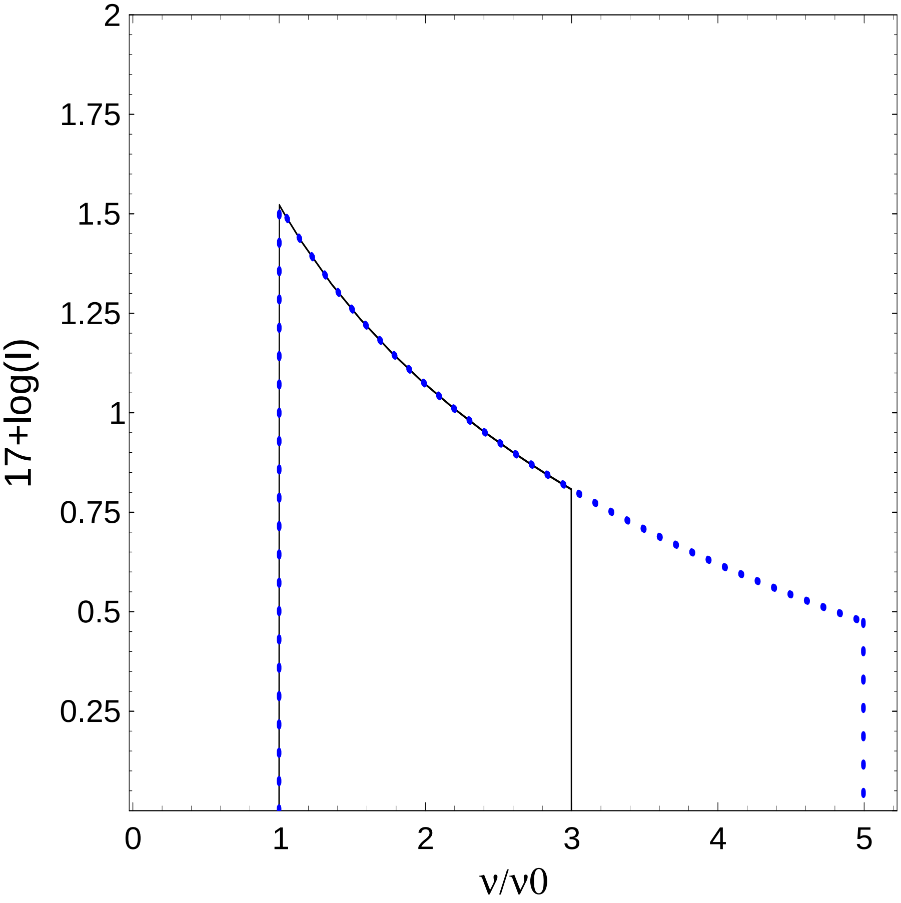

Figure 5.3

The value of the integral of equation (5.8) as a function of ν_e/ν_{mn} for $\delta = 1/5$ (dotted line) and $\delta = 1/3$ (solid line). Evidently the integral and hence the optical depth is maximal if the emission frequency is right at the line center.

(expansion). The maximum value of the integral is 1.67×10^{-16}. Hence the maximal optical depth is given by,

$$\begin{aligned} \tau_{max} &\approx \frac{1.67 \times 10^{-16} \sigma_{cl} f_{nm} n_0 \, c}{(1+z_e)^{-3/2} H_0} && (5.9) \\ &\approx 4 \times 10^{-3} h^{-1} \left(\frac{n_0}{10^{-13} \mathrm{cm}^{-3}} \right) \left(\frac{1+z_e}{30} \right)^{3/2} \frac{f_{mn}}{10^{-2}}. && (5.10) \end{aligned}$$

Hence for a Lorentz profile the optical depth is always much less than unity since the strongest Lyman Werner lines have oscillator strengths of $\sim 2 \times 10^{-2}$.

So we have learned that at the wings of any realistic line there will be no significant absorption or shielding will occur. However, the line center is typically dominated by Doppler broadening.

Absorption in the Core of the Line

Unfortunately we could not find any analytic solution to the integral of equation (5.8) using a Doppler profile. However, we can estimate what happens close to the line center. Let us first recall the Doppler profile,

$$\begin{aligned} \phi(\nu) &= \frac{1}{\sqrt{2\pi}\sigma} \exp\left(-\frac{(\nu - \nu_{mn})^2}{2\sigma^2} \right), && (5.11) \\ \sigma &= \nu_{mn} \sqrt{\frac{kT}{Mc^2} + \frac{v_{turb}^2}{2c^2}}. && (5.12) \end{aligned}$$

Assuming that thermal broadening dominates the at the line center is given by,

$$\phi_{max} = \phi(\nu = \nu_{mn}) = \frac{1}{\sqrt{2\pi}\sigma} \approx 4.37 \times 10^{-10} \left(\frac{3 \times 10^{15} \mathrm{Hz}}{\nu_{mn}} \right) \sqrt{\frac{M}{m_p T}}, \quad (5.13)$$

where m_p denotes the proton mass. Hence the maximal absorption cross section is given by,

$$\sigma_{max} = \sigma_{cl} f_{mn} \phi_{max} = 1.2 \times 10^{-11} \left(\frac{3 \times 10^{15} \mathrm{Hz}}{\nu_{mn}} \right) \sqrt{\frac{M}{m_p T}} f_{mn}. \quad (5.14)$$

The line width is approximately given by $\triangle\nu \approx 1/\phi_{max}$. To reach optical depth unity within the distance over which a photon is redshifted by $\triangle\nu$ a column density of $N \sim 1/\sigma_{max}$ is required. This places a lower limit on the comoving number density of the absorbing material,

$$\begin{aligned} h \, n_0 &> \frac{1}{\sigma_{max} \, r \, (1+z)^3} && (5.15) \\ &\approx 6.0 \times 10^{-12} \left(\frac{10^{-2}}{f_{mn}} \right) \left(\frac{\nu_{mn}}{3 \times 10^{15} \mathrm{Hz}} \right) \left(\frac{1+z_e}{31} \right)^{-3/2} \mathrm{cm}^{-3}. && (5.16) \end{aligned}$$

Evidently for molecular hydrogen with a comoving number density of $\sim 10^{-13}$ cm^{-3} even the strongest Lyman Werner absorption lines never become optically thick.

In summary we found that for the expanding homogeneous intergalactic medium the molecular hydrogen absorption lines in the Lyman Werner bands never become optically thick for the redshifting photons.

5.1.4 Ratecoefficients

Now that we have seen that the Lyman Werner bands of intergalactic H_2 are optically thin due to the Hubble expansion let us compute the corresponding rate coefficient. Let N_{ph} be the number of photons per Hertz per second and per cm^{-2}. Then the photo–dissociation rate coefficient is given by,

$$k = \sigma_{cl} \int N_{ph}(\nu) \sum_i f^i_{diss} f^i_{osc} \phi(\nu) d\nu, \tag{5.17}$$

where σ_{cl}, and $\phi(\nu)$ gain denote the classical crossection and the line profile. Assuming N_{Ph} to be constant over the small frequency interval of interest and appropriately weighting for a thermal ortho to para ratio we get the optical thin rate,

$$k_{thin} = \sigma_{cl} N_{Ph} \sum_i f^i_{osc} f^i_{diss} = \langle J \rangle \sum_i \frac{f^i_{osc} f^i_{diss}}{h\nu_i} \approx 1.01 \times 10^8 \langle J \rangle \ \mathrm{s}^{-1}, \tag{5.18}$$

where the average flux in the Lyman Werner bands $\langle J \rangle = N_{ph} \times 12.8 \ \mathrm{eV}$ is expressed in units of $\mathrm{erg\ s^{-1}\ cm^{-2}\ Hz^{-1}}$. This rate is in perfect agreement with the one quoted by Abel et al. (1997).

In section 5.1.3 we have discussed how individual photons are redshifted as a function of distance. This translates now to a distance dependent rate coefficient from the source since the higher energy lines cannot contribute to the dissociation anymore. This is because the photons above the Lyman limit are absorbed by the atomic hydrogen closer to the source.

Using equation (5.3) one finds when a $13.6 \ \mathrm{eV}$ photon shifts across a Lyman Werner lines which results in a decrease of the photo–dissociation rate. The ratio of the actual rate coefficient to the optically thin rate is plotted in Figure 5.4. As expected the effect of redshifting plays only a role at significant distances compared to the cosmic horizon. However, here we assumed only H_2 to be present. In realistic situations the Lyman series of atomic hydrogen will be the dominant source of opacity for soft UV photons.

5.1.5 Does intergalactic H_2 significantly modulate a soft UV background?

Given a point source that radiates N_{LW} photons per seconds in the Lyman Werner bands one finds that the photo–dissociation time ($1/k_{diss}$) will become longer than the Hubble time ($2(1+z)^{-3/2}/(3H_0)$) at a proper critical radius

$$r_{crit} = 4.5 \ \mathrm{kpc}\, h^{-1/2} \left(\frac{1+z}{15}\right)^{-3/4} \frac{N_{LW}}{10^{48} \ \mathrm{s}^{-1}}. \tag{5.19}$$

This is the maximum radius of the H_2 PDR caused by an individual UV source. Nevertheless, the mean free path of a photon is much larger than the PDR. Hence one expects that such sources establish a UV background below the Lyman Limit even before all primordial H_2 is dissociated.

Assuming a uniform soft UV background the photo–dissociation time of molecular hydrogen will become shorter than the Hubble time once the UV flux in the Lyman Werner Bands exceeds,

$$J_{crit} = 2.2 \times 10^{-4} J_{21} h \left(\frac{1+z}{15}\right)^{3/2}, \tag{5.20}$$

where $J_{21} = 10^{-21} \ \mathrm{erg\ s^{-1}\ Hz^{-1}\ cm^{-2}\ sr^{-1}}$. This corresponds to a photon number density, n_γ of

$$n_\gamma^{crit} \approx J_{crit} \times 12.8 \ \mathrm{eV}/c = 3.6 \times 10^{-25} h \left(\frac{1+z}{15}\right)^{3/2} \ \mathrm{cm}^{-3}, \tag{5.21}$$

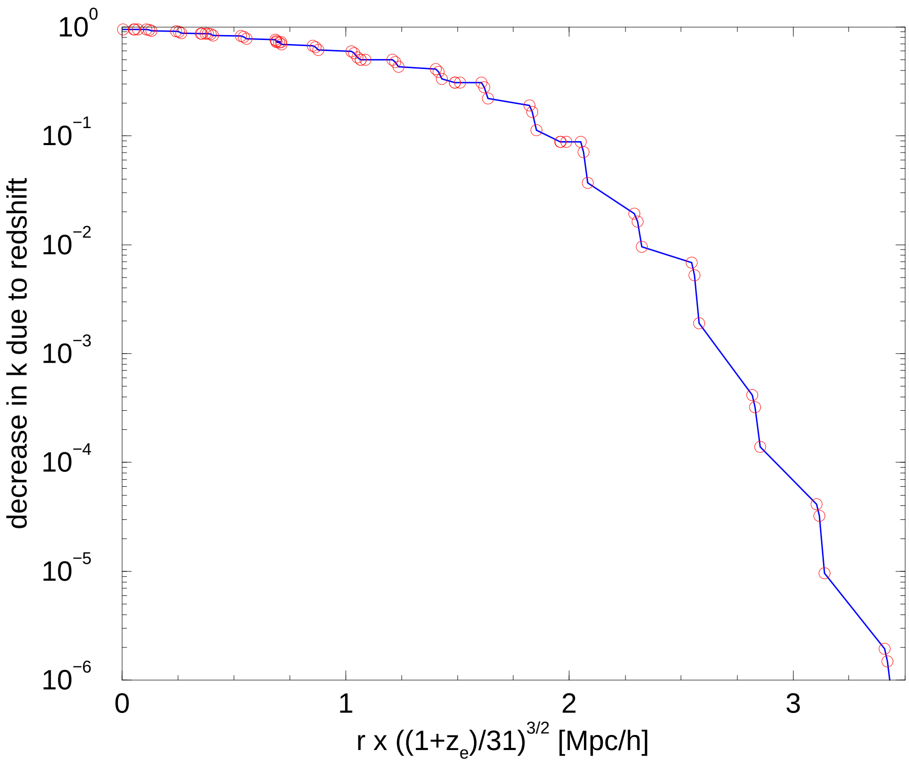

Figure 5.4
Decrease of the H_2 photo–dissociation rate due to redshift as a function of radius. Note that this is does not include the geometrical r^{-2} drop of the flux nor optical depth effects.

At values larger than this critical value of the soft UV background will lead to the destruction of all primordial H_2 . Soon after this critical flux has been exceeded all intergalactic H_2 will be dissociated and the dominant opacity are only scattering in the Lyman series of neutral hydrogen.

5.2 THE STRUCTURE OF COSMOLOGICAL H_2 PHOTO–DISSOCIATION REGIONS

A schematic sketch of four distinct regions in the radial structure of an H_2 photo–dissociation region is shown in Figure 5.6 which summarizes the above discussion. Region I extends to the usual H I ionization front or Strömgren radius. Inside this region, the temperature is high ($\sim 10^4$K), hydrogen is ionized, H_2 is photo–dissociated, and the H_2 abundance tends to zero. Region II is defined to extend from R_i to the radius $R_\mathrm{p} \sim 2.5\,h^{-1/2}(1+z)_{30}^{-3/4} N_{LW,47}^{1/2}$ kpc, where the H_2 photodissociation time becomes longer than the Hubble time. Here $N_{LW,47} = N_{LW}/10^{47}\mathrm{s}^{-1}$ is the photon number flux in the Lyman Werner bands per second. In this region the temperature is that

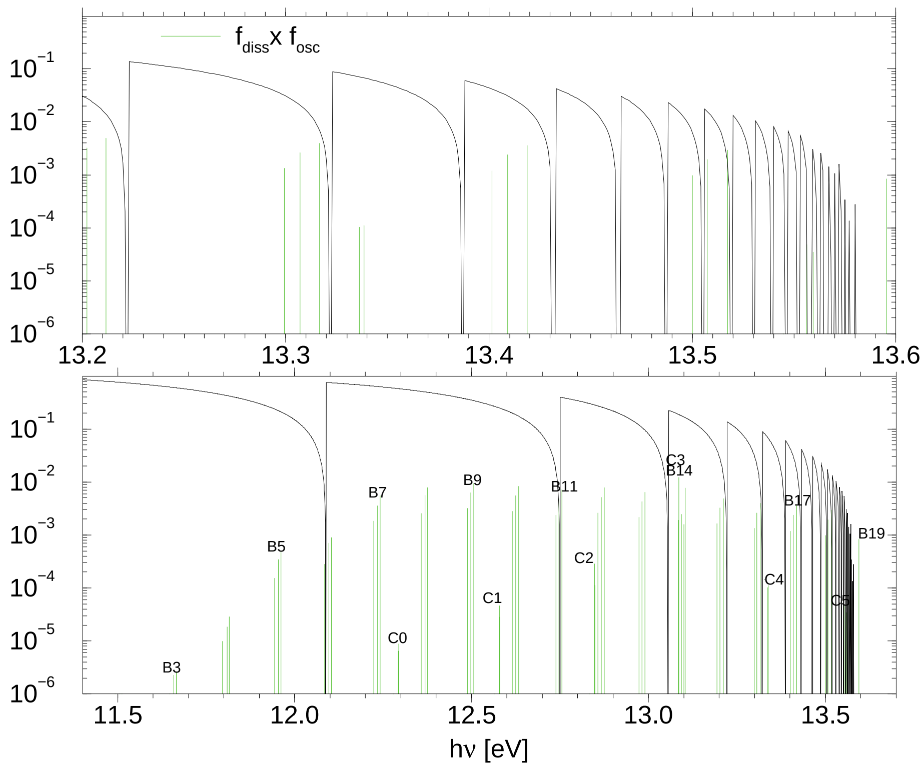

Figure 5.5

The typical shape of the spectrum of the soft UV background (Haiman, Abel, and Rees 1999). Again the positions of the relevant Lyman Werner bands are indicated.

of the IGM, and the H_2 fractions are still low, but slowly rise to its background value of $\sim 2 \times 10^{-6}$. Since the optical depth in the Lyman Werner lines are very small, the dissociation front is significantly diluted. Region III is defined to extend from $R_{\rm p}$ to the radius $R_{\rm s} \approx 2h^{-1}[(1+z)/31]^{-1.5}$ Mpc where Lyman γ shifts to Lymanβ. In this region, the source contributes to the soft UV background, but its flux is diminished by absorption into the atomic Lyman series. In region IV beyond $R_{\rm s}$, all photons in the Lyman Werner bands are absorbed by an atomic Lyman line. Hence, at such large scales, an individual source does not contribute to the UVB and intergalactic H_2 dissociation.

5.3 THE INFLUENCE OF A SOFT UV BACKGROUND ON STRUCTURE FORMATION

Given a noticeable soft UV background has formed one is interested whether objects with low virial temperatures ($< 10^4$ K) will be able to still form H_2 and dissipate its gravitational energy. First we could try to estimate an equilibrium abundance of H_2 as follows.

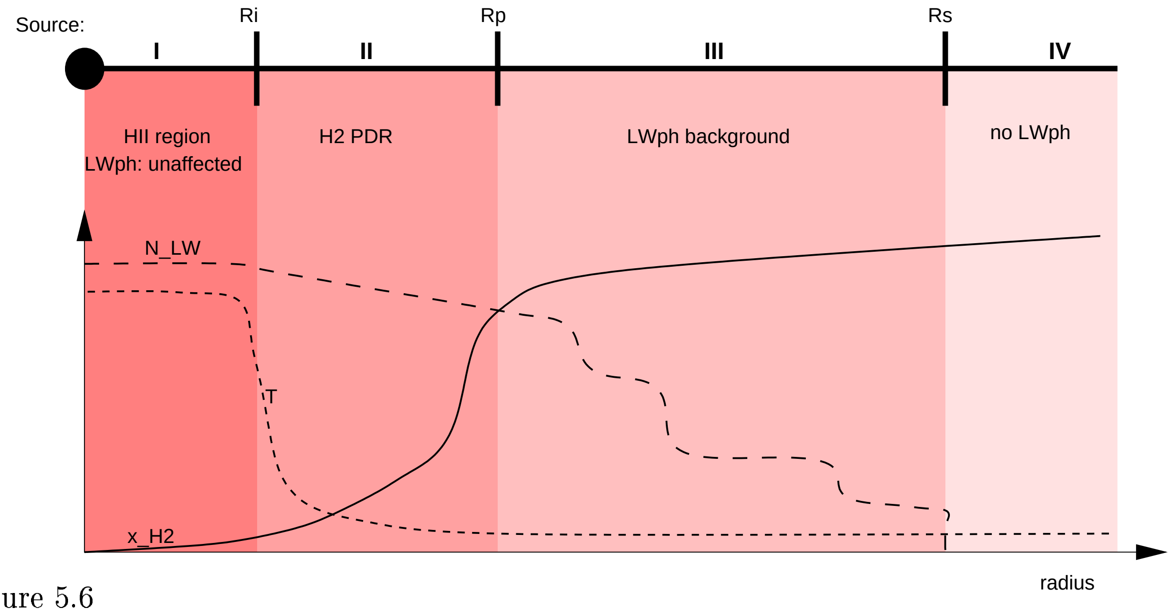

Figure 5.6

Schematic sketch of the radial structure of a cosmological photo–dissociation region. Region I is the usual Strömgren sphere, bounded by the H I ionization front at R_i. Inside this region, the temperature is high ($\sim 10^4$K) hydrogen is ionized, and the H_2 abundance tends to zero. Region II extends from R_i to the radius R_p where the H_2 photodissociation time becomes longer than the Hubble time. Here the temperature is that of the IGM, the H_2 fractions are still low, but slowly rise to the background value of $\sim 2\times 10^{-6}$. Region III extends from R_p to the radius R_s, where Lyγ shifts to Lymanβ. In this region, the source contributes to the soft UV background, but its flux is diminished by absorption into the atomic Lyman series. In region IV beyond R_s, all photons in the Lyman Werner bands are absorbed by an atomic Lyman line. Hence, at such large scales, an individual source does not contribute to the UVB and intergalactic H_2 dissociation.

5.3.1 Equilibrium Arguments

From Abel et al. (1997) we know that at temperatures below 6000 K no collisional process is important for H_2 destruction. Knowing also that the the dominant H_2 formation mechanisms is the associative detachment of H^- (k_8), we have the simple rate equation for the number density of H_2 ,

$$\dot{n}_{H_2} = k_8\, n_{H^-}\, n_H - k_{PD}\, n_{H_2}. \tag{5.22}$$

Assuming now that the flux at $h\nu > .755$ eV is low we can substitute the equilibrium abundance of H^- with $n_{H^-} = k_7\, n_e / k_8$ where $k_7 \approx 1.8\times 10^{-18}$ cm^3 s^{-1} is the rate for radiative attachment to H^- . If we now derive the equilibrium H_2 abundance by requiring $\dot{n}_{H_2} = 0$ and using $x \equiv n_e/n$, and $f_{H_2} = n_{H_2}/n$ we find,

$$f_{H_2} = \frac{k_7}{k_{PD}}\, x\,(1-x)\, n \approx \frac{k_7}{k_{PD}}\, x\, n, \quad \text{for } x \ll 1. \tag{5.23}$$

5.3.2 Time dependent analysis

For constant temperature and density ($\dot{n} = 0$) and small ionized fractions we can solve the rateequation for the time–dependent H_2 fraction directly.

$$\dot{f}_{H_2}(t) = k_7\, x\,(1-x)\, n - k_{PD}\, f_{H_2} \approx k_7\, x\, n - k_{PD}\, f_{H_2}\,, \quad \text{for } x \ll 1. \tag{5.24}$$

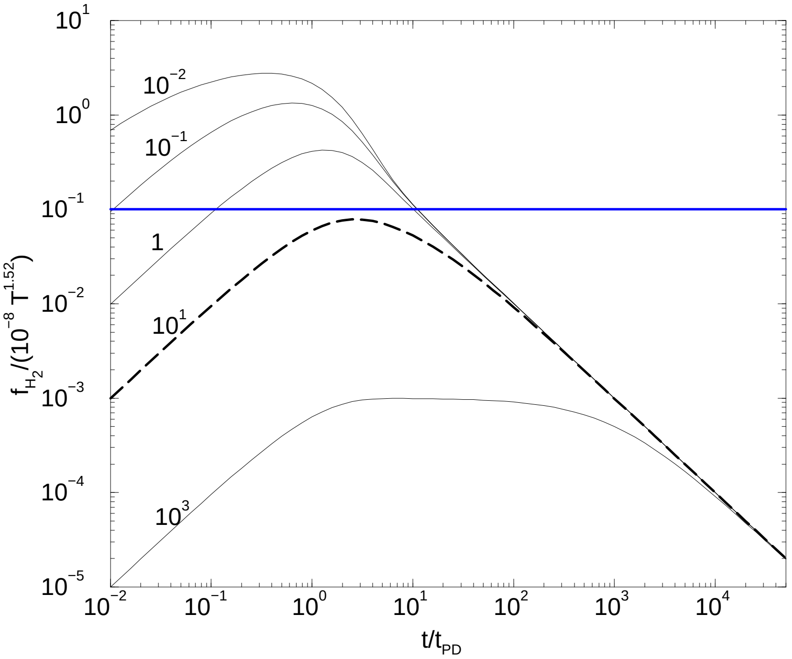

Figure 5.7

Time dependent evolution of the H_2 fraction in the presence of a soft UV background. In terms of the definitions in equation (5.26) f_{H_2}/r_3 is plotted as a function of r_1 for various values of r_2 given by the labels of the individual curves.

A longer calculation yields,

$$\frac{f_{H_2}(r_1)}{r_3} = e^{-r_1-r_2}\left[E_i(r_1+r_2) - E_i(r_2)\right]\ , \quad \text{for } f_{H_2}(t=0)=0, \tag{5.25}$$

where,

$$\begin{array}{llll} r_1 & = \frac{t}{t_{PD}} \approx 1.3\times 10^{-12}\, J_{LW}\, t; & r_2 & = \frac{t_{rec}}{t_{PD}} \approx 0.56\frac{J_{LW}^{21}}{n\, x(t=0)}\, T^{0.64}; \\ r_3 & = \frac{t_{rec}}{t_{H^-}} \approx 10^{-8}\, T^{1.52}; & E_i & = -\int_{-x}^{\infty} \frac{e^{-t}}{t}\, dt. \end{array} \tag{5.26}$$

Figure 5.7 plots the solution of equation (5.25) for various values of r_2. From Abel (1995) and Tegmark et al. (1997) we know that r_3 is approximately the the H_2 fraction reached within a few recombination times if there is no soft UV flux present. Therefore, we can interpret the abscissa of Figure 5.7 as a suppression factor caused by the UV photons. Since the maximum fraction of H_2 formed in the gas phase is $\sim 5\times 10^{-3}$ but $\sim 5\times 10^{-4}$ is required for efficient cooling (Tegmark et al. 1997) only for $f_{H_2}/r_3 > 0.1$ can we expect structures to form unimpressed by the UV photons. From Figure 5.7 we see that this is only possible for $r_2 < 10$. This translates into a constraint on the UV flux of $J_{LW}^{21} \lesssim 20 n\, x(t=0)\, T^{-0.64}$. This leads for the parameters of interest ($n \lesssim 10^{-2}$ cm^{-3}, $x(t=0) \lesssim 10^{-4}$, and $T \sim 1000$ K) a yet more stringent limit than equation (5.20) which we derived from requiring the photo–dissociation time to be less than the Hubble–time. This is simply due to the effect of the typically rather long H_2 formation time scales. Please note that the limit derived here assumed no photo–detachment of H^- . Furthermore, we did not take into account the effect that the level population of H_2 in collapsed objects is different from the cold IGM. This latter effect would also rather increase the photo–dissociation rate than lower it, requiring the UV flux yet to be lower than the upper limit derived here.

However, one might still argue that radiative transfer effects could still allow H_2 to form.

5.3.3 Could Self–shielding play a role?

In static H_2 photo–dissociation regions it is typically found that H_2 starts to self–shield at molecular column densities $\gtrsim 10^{14}\ \mathrm{cm}^{-2}$. Using the spherical collapse model to estimate the initial H_2 column density we find,

$$N_{H_2} \approx f_{H_2} r_{vir} n_{vir} \approx 2.1\times10^{13}\left(\frac{V_c}{10\ \mathrm{km/s}}\right)\left(\frac{f_{H_2}}{2\times10^{-6}}\right)\left(\frac{1+z}{10}\right)^{3/2}\left(\frac{\delta}{18\pi^2}\right)\left(\frac{\Omega_B h^2}{0.0125}\right)\ \mathrm{cm}^{-2}. \tag{5.27}$$

From this one concludes that even in optimistic cases self–shielding will not play a role. Nevertheless, a smaller mass high density core might form H_2 if a realistic density profile is assumed. Such a more realistic density profile is given by the truncated isothermal sphere of Shapiro, Iliev, and Raga (1998). Their density profile can be fitted with

$$\tilde{\rho}(\zeta) = \frac{\rho}{\rho_0} = \frac{21.38}{9.08+\zeta^2} - \frac{19.81}{14.62+\zeta^2}, \quad \zeta = \frac{r}{r_0}, \tag{5.28}$$

where the central density ρ_0 and the core radius r_0 are given by

$$\rho_0 = 3.376\times10^{-25}(1+z_{coll})^3 h^2\ \mathrm{g/cm^3}, \tag{5.29}$$

$$r_0 = 63.7\left(\frac{M}{10^6\ M_\odot}\right)^{1/3}(1+z_{coll})^{-1}h^{-2/3}\ \mathrm{pc}\ . \tag{5.30}$$

This profile is defined up to the truncation radius at $\zeta = 29.4$. Figure 5.8 shows the density profile and mass fractions within a given radius. Evidently the core contains 0.5% of the total mass of the object. If this core manages to self–shield itself from a soft UV background it still might form stars. Noting that the density in the core is approximately constant and using the analytical solution

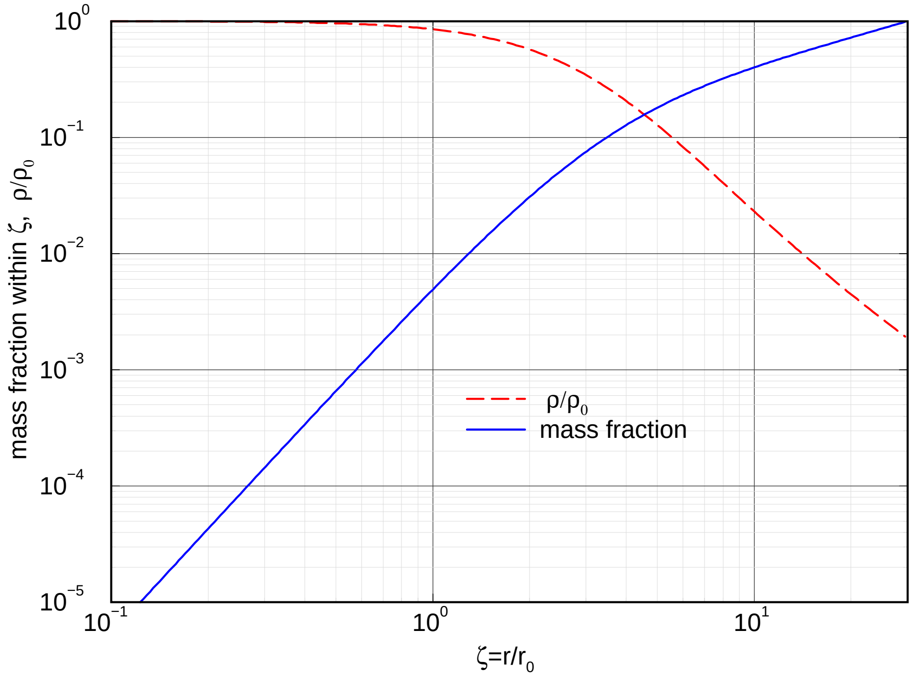

Figure 5.8
The density profile and mass fraction within a given radius for the truncated isothermal sphere profile of Shapiro, Iliev and Raga (1998).

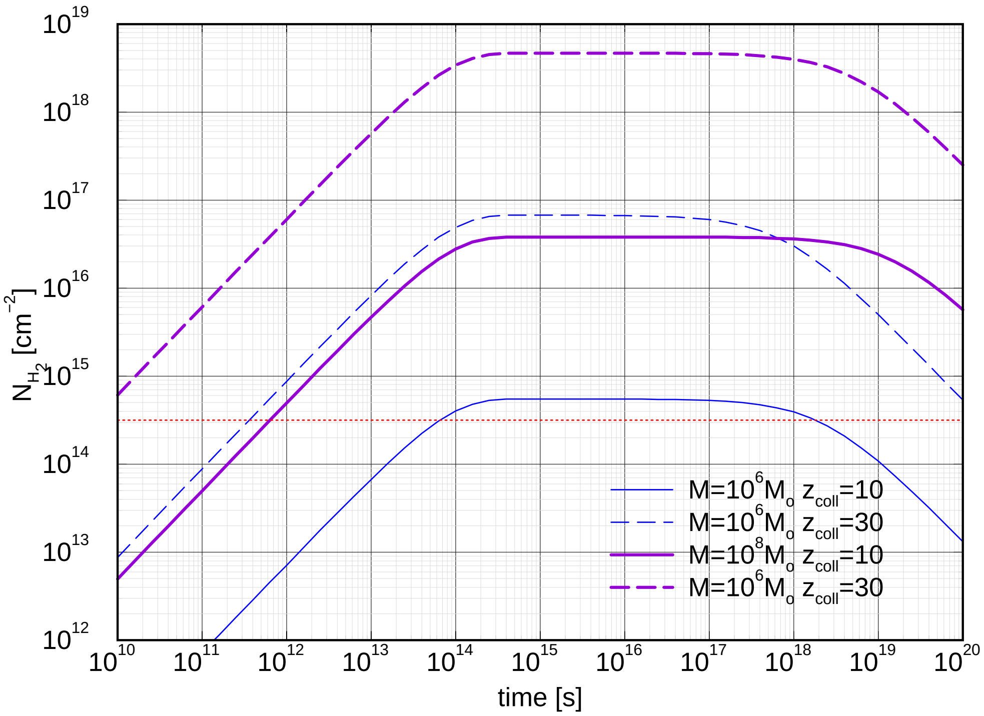

Figure 5.9

Analytical solution of the time evolution of the H_2 column density in the core of a truncated isothermal sphere. Here we assumed $x = 10^{-4}$ and $J^{21}_{LW} = 0.01$

to the time evolution of the H_2 fraction of equation (5.25) we can compute whether the core ever becomes self–shielding or not. Figure 5.9 shows the time evolution of the H_2 fraction in the core of a truncated isothermal sphere for various masses and collapse redshifts. Here we assumed an initial ionized fraction of $x = 10^{-4}$ and a soft UV flux of $J^{21}_{LW} = 0.01$. Clearly the H_2 columndensity of the core will exceed $5 \times 10^{14}\ \mathrm{cm}^{-2}$ for all the cases shown. The column–density decreases for large times because all electrons have recombined switching off H_2 formation. Note, however, that we assumed the density to stay constant. This is certainly not the case once H_2 is self–shielded and its cooling allows the core to contract to yet higher densities.

We conclude that if the central densities of a truncated isothermal sphere are reached and $J^{21}_{LW} \lesssim 0.01$ that small scale structure is still able to collapse and cool via H_2 .

5.4 SUMMARY AND CONCLUSIONS

In summary we can conclude that given that H_2 photo–dissociation regions overlap newly formed objects with virial temperatures less than 10^4 K are unlikely to be able to form H_2 cool appreciably. This is the negative feedback effect described by Haiman, Rees and Loeb (1997) and Haiman, Abel, and Rees (1999). These objects are possible the explanation of the large number of Lyman Limit systems at high redshifts (Abel and Mo 1998).

However, Haiman, Abel and Rees (1999) have also shown that if some hard X–ray photons were produced by an early generation of quasars that the radiative feedback might be positive. I.e. since hard X–rays enhance the free electron fraction in the cores of collapsed objects they enable more H_2 to form and finally allow the gas to cool.

Chapter 6

Lyman Limit Absorption Systems at high redshifts

ABSTRACT

We propose that a large fraction of the QSO Lyman limit absorption systems (LLS) observed at high redshift ($z \gtrsim 3$) originate from gas trapped in small objects, such as minihalos, that form prior to reionization. In the absence of a strong UV flux, the gas is predominantly neutral and may form clouds with HI column density $N_{\rm HI} \gtrsim 10^{18}\ {\rm cm}^{-2}$. Due to their high densities and high HI column densities, these clouds are not destroyed by the onset of the UV background at a later time. Thus, if not disrupted by other processes, such as mergers into larger systems or 'blow away' by supernovae, they will produce LLS. We show that the observed number density of LLS at high redshifts can well be reproduced by the survived 'minihalos' in hierarchical clustering models such as the standard cold dark matter model. The number density of LLS in such a population increases with z even beyond the redshifts accessible to current observations and dies off quickly at $z \lesssim 2$. This population is distinct from other populations because the absorbing systems have small velocity widths and a close to primordial chemical composition. The existence of such a population requires that the reionization of the universe occurs late, at $z \lesssim 20$.

6.1 INTRODUCTION

Lyman limit absorption systems (LLS), observed as breaks in quasar spectra at the rest-frame wavelength of the Lyman continuum edge, are produced by gaseous clouds optically thick to Lyman continuum photons. These systems can be observed over a wide range of redshift, from $z \sim 0$ to approximately that of the highest-redshift quasars. Thus, such systems can be used to probe the gas in the Universe at various redshifts. Due to their relatively high HI column density ($N_{\rm HI} \gtrsim 10^{17}\ {\rm cm}^{-2}$), these systems are usually thought to arise from photoionized clouds in gaseous galactic halos (see e.g. Steidel 1990, Mo & Miralda-Escudé 1996). There is now direct observational evidence that some of the LLS are indeed associated with galaxies (see e.g. Steidel 1995), at least at redshift $z < 3$. This is not surprising, because any HI disk like that of our own Galaxy will produce a LLS when intersecting a sightline to a quasar. However, the observed rate of incidence (i.e. the number of systems per sightline per unit redshift) of LLS is large and increases rapidly with redshift (Stengler-Larrea et al. 1995); there is no indication of a reversal of this trend even for the LLS with the highest redshift $z \sim 4.5$ observed so far (Storrie-Lombardi et al. 1994). The observed rate of incidence of LLS at $z \sim 4$ is about 30 times larger than that expected from the local number density of galaxies with absorption cross sections given by the optical Holmberg radius. Thus, if LLS at $z \gtrsim 4$ were also associated with galaxies, it would mean that (1) most galaxies have already formed at that redshift, and (2) the absorption cross sections of galaxies are much larger at high redshifts. However, in a hierarchical model of structure formation, such as the standard cold dark matter (CDM) model and its variants, the number density and sizes of galaxies are small at high redshifts, because most gas has not yet been assembled into large galaxies (Mo & Miralda-Escudé 1996). It is therefore unlikely that LLS observed at high redshifts are due to galactic populations.

It is possible that a large fraction of the observed LLS at high redshifts are produced by photoionized clouds in small halos. Recent hydrodynamic simulations show that low column density absorption systems can be produced by gas in filamentary structures that arise from the gravitational collapse of initial density fluctuations (e.g. Cen et al. 1994; Zhang, Anninos, & Norman 1995; Hernquist et al. 1996; Haehnelt, Steinmetz & Rauch 1996; Miralda-Escudé et al. 1996). The number densities of LLS given by these simulations were, however, found to be lower by a factor of about ten than what is observed (e.g. Katz et al. 1996). The discrepancy at $z \lesssim 2$ may be explained by the population of pressure-confined clouds in gaseous halos that are not resolved by current simulations (Mo & Miralda-Escudé 1996). The discrepancy at $z \gtrsim 3$, however, was not explained by previous investigations based on photoionization models in hierarchical cosmogonies (e.g. Gardner et al. 1996).

It is also possible that the flux of the UV background may drop substantially at $z > 3$ and the HI column density of a cloud could be underestimated in models assuming a constant UV flux. However, recent observational results based on the proximity effect show that the UV flux at the Lyman continuum edge is about $(1-5) \times 10^{-22} \mathrm{erg\,s^{-1}\ cm^{-2}\,Hz^{-1}\,sr^{-1}}$ at $z \sim 4.5$ (Williger et al. 1994; Giallongo et al. 1996; Lu et al. 1996). This value of the UV flux is already comparable to, or even higher than, the ones used in most of the model considerations mentioned above.

In this chapter we suggest the possibility that the discrepancy between model predictions and observations of the LLS at high redshifts ($z \gtrsim 3$) is a result of the neglect of the contribution of minihalos that collapsed prior to reionization. The gas in such small systems is predominantly neutral and may form clouds with H I column density $N_{\mathrm{HI}} \gtrsim 10^{18}\ \mathrm{cm}^{-2}$. Because of their high density and high HI column density, these clouds will not be destroyed, or ionized by the onset of the UV background at a later time. They will therefore produce LLS at lower redshifts, if not disrupted by other processes.

We present our model for the LLS observed at high redshifts and compute their number per unit redshift in Section 6.2. A brief discussion of our model is given in Section 6.3.

6.2 A NEW POPULATION OF LYMAN LIMIT SYSTEMS

For simplicity we assume the Universe to be flat with the cosmic density parameter $\Omega_0 = 1$. The Hubble constant is written as $H_0 = 100h\ \mathrm{km/s\ Mpc^{-1}}$.

6.2.1 Physical properties

Prior to the epoch of reionization the physical properties of cosmological structures can be estimated from the spherical collapse model (see e.g. Padmanabhan, 1993). The gas in a collapsing dark matter perturbation is shock heated to the virial temperature

$$T_{vir} \equiv \frac{\mu V_c^2}{3k} \approx 4.0 \times 10^3 \text{ K} \left(\frac{V_c}{10 \text{ km/s}}\right)^2 \left(\frac{\mu}{m_P}\right), \tag{6.1}$$

where V_c is the three dimensional virial velocity of the halo, m_P the proton mass, and μ the mean mass per particle.

The total H number density in a dark matter halo that collapses at a redshift, z, with an overdensity δ at virialization reads

$$\begin{aligned} n_{vir} &= \frac{\Omega_B \rho_{\text{crit}} \delta}{m_P}(1+z)^3 \approx 9.7 \times 10^{-3} \\ &\times \left(\frac{\Omega_B h^2}{0.0125}\right)\left(\frac{1+z}{10}\right)^3 \left(\frac{\delta}{18\pi^2}\right) \text{ cm}^{-3}, \end{aligned} \tag{6.2}$$

where ρ_{crit} denotes the closure density. Assuming that dark halos are singular isothermal spheres with density profile $\rho(r) \propto r^{-2}$, the virial radius r_v, defined as the radius within which the mean mass overdensity is $18\pi^2$, can be written:

$$r_{vir} = \frac{V_c t}{2\pi} \approx 350 \text{ pc } h^{-1} \frac{V_c}{10 \text{ km/s}} \left(\frac{1+z}{10}\right)^{-3/2}, \tag{6.3}$$

where $t = (2/3H_0)(1+z)^{-3/2}$ is the cosmic time at z.

For halos with $T_{vir} \lesssim 10^4$ K ($V_c \lesssim 15$ km/s) the gaseous component cannot be collisonally ionized and will remain neutral. Due to the high collapse redshifts ($z > 5$) considered here, the recombination time scale in minihalos is shorter than the Hubble time, and the gas in clouds with $V_c \gtrsim 15$ km/s before reionization will also be neutral shortly after their formation. As a result, the column density of neutral hydrogen atoms, N_{HI}, is given by

$$\begin{aligned} N_{\text{HI}} &\approx 2 r_{vir} n_{vir} \approx 2.1 \times 10^{19} \left(\frac{V_c}{10 \text{ km/s}}\right) \\ &\times \left(\frac{1+z}{10}\right)^{3/2} \left(\frac{\delta}{18\pi^2}\right) \left(\frac{\Omega_B h^2}{0.0125}\right) \text{ cm}^{-2}. \end{aligned} \tag{6.4}$$

The corresponding total mass of such a halo is

$$\begin{aligned} M = \frac{V_c^3 t}{2\pi G} &\approx 7.9 \times 10^6 \left(\frac{V_c}{10 \text{ km/s}}\right)^3 \\ &\times \left(\frac{1+z}{10}\right)^{-3/2} h^{-1} M_\odot. \end{aligned} \tag{6.5}$$

It is clear that the optical depth at the photoionization threshold,

$$\begin{aligned} \tau = \sigma(\nu_{\text{TH}}) N_{\text{HI}} &\approx 130 \left(\frac{V_c}{10 \text{ km/s}}\right) \left(\frac{1+z}{10}\right)^{3/2} \\ &\times \left(\frac{\delta}{18\pi^2}\right) \left(\frac{\Omega_B h^2}{0.0125}\right) \text{ cm}^{-2}, \end{aligned} \tag{6.6}$$

exceeds unity for a wide range of collapse redshifts and virial velocities.

To determine what happens to the clouds once the UV background switches on we analyze the equilibrium equation of the ionized fraction for a pure hydrogen gas, $x \equiv n_e/n$, where n_e and n denote the free electron and total baryonic number density, respectively. This fraction is given by

$$0 = k_{Ph} n(1-x) - k_{Rec} n^2 x^2, \tag{6.7}$$

where $k_{Ph} = 4\pi \int_{\nu_{TH}}^{\infty} (J/h\nu) \exp[-N_{\rm HI}\sigma(\nu)]\sigma(\nu) d\nu$ and k_{Rec} denote the rate coefficients for photoionization of neutral hydrogen and radiative recombination to H I, respectively. Motivated by the indirect measurements from the proximity effect (see Giallongo et al. 1996, and references therein) we assume the background UV flux to be given by a powerlaw

$$J(\nu) = 10^{-21} J_{21} \left(\frac{h\nu}{1{\rm Ryd}}\right)^{-\alpha} \;{\rm erg\ cm^{-2} (\ Hz\ s\ sr)^{-1}}, \tag{6.8}$$

where h is Planck's constant and $h\nu_{TH} = 1{\rm Ryd} \equiv 13.6\ {\rm eV}$ is the H I ionization threshold. In the optical thick limit the photoionization rate coefficient can be approximated by a power law $k_{Ph} \approx J_{21} k^0_{Ph} [N_H(1-x)]^{-\beta}$, where N_H is the total column density of hydrogen nuclei. The exponent β has a non–trivial dependence on α and is determined numerically to vary from 1.35 to 1.69 for $1 < \alpha < 2$. Inserting this approximate expression for the photoionization rate into the equilibrium equation for the free electron fraction [equation (6.7)] yields the implicit solution for x

$$f(x) \equiv \frac{x^2}{(1-x)^{1-\beta}} = \frac{J_{21} k^0_{Ph} N_H^{-\beta}}{n k_{Rec}} \equiv C, \tag{6.9}$$

which for $\beta = 0$ reduces to the more familiar optical thin case. We adopt $\alpha = 1.8$ for the spectral index, with which the photoionization rate can be approximated by $k_{Ph} \approx 4.1 \times 10^{-15} J_{21} (N_{\rm HI}/10^{19}\ {\rm cm^{-2}})^{-\beta}\ {\rm s^{-1}}$ with $\beta = 1.6$.

The right hand side of equation (6.9) has a maximum at $x = x_{max} \approx 0.8$ with a value of $f(x_{max}) \approx 0.25$. The existence of this maximum shows that ionization equilibrium cannot be achieved for $J_{21} k^0_{Ph} N_H^{-\beta}/(n k_{Rec}) > f(x_{max})$. In this case photoionization overcomes recombination and ionizes the gas until a new, highly ionized, equilibrium state is reached at column densities $\ll 10^{17}\ {\rm cm^{-2}}$. As discussed in Mücket and Kates (1997), the evolution of such systems from one equilibrium state to another can be rapid. The recombination rate[1] suitable for an equilibrium temperature of 10^4 K is $k_{Rec} \approx 2.6 \times 10^{-13}\ {\rm cm^3\ s^{-1}}$ (Ferland et al. 1992). Thus, for a given J_{21}, the maximum of $f(x)$ can be used to derive a critical total hydrogen column density N_H^{crit}. Note that this column density is calculated at the edge of the cloud and is approximately equal to $r_{vir} n_{vir}$ [see equation (6.2) and equation (6.3)]. We can therefore define a minimum collapse redshift, z_{crit}, for halos of a given virial velocity, so that they will remain optically thick if they form at $z > z_{crit}$. This minimum collapse redshift can be written as

$$\begin{aligned} 1 + z_{crit} &\approx 7.2 \left(\frac{J_{21}}{0.5}\right)^{5/27} \left(\frac{V_c}{10\ {\rm km/s}}\right)^{-8/27} \\ &\times \left(\frac{\delta}{18\pi^2} \frac{\Omega_B}{0.05}\right)^{-13/27} \left(\frac{h}{0.5}\right)^{-2/3}. \end{aligned} \tag{6.10}$$

As we will show below, minihalos (with $V_c \sim 10$ km/s) in current hierarchical models have typical collapse redshifts higher than this critical value; they can therefore retain their high initial H I column densities.

---

[1] Note that the Case B recombination rate is used for the optical thick case considered here.

To check the robustness of the above derivation for the critical collapse redshift we have integrated the time-dependent chemistry and cooling model presented in Abel et al. (1997a). We found good agreement between the numerical results and the analytic expression of the critical redshift given by equation (6.10).

The density of gas contained in minihalos considered here is quite high due to their high collapse redshifts. The recombination time scale for the gas is short, about 0.1 Myr, which makes them stable against photoionization from internal stellar sources. On the other hand, only a few supernova explosions may be able to blow out most of the gas from the halos (see Ciardi & Ferrara, 1997, and references therein) if star formation can happen in them. However, systems that form in halos with $V_c \lesssim 15$ km/s at $z \lesssim 15$ are not be able to cool since H_2 formation is inefficient in these halos at such redshifts (see Tegmark et al. 1997, and Abel et al. 1997b). Also the UV flux of the first structures in the universe may lead to H_2 photodissociation prior to H I reionization (Haiman, Rees and Loeb 1997), inhibiting line cooling by H_2 . Furthermore H I line cooling is not efficient due to the low virial temperature ($\sim 10^4$ K). Thus these systems may not form stars and hence are not subject to "blow away". The gas can only be gravitationally confined in the dark matter halo if the typical particle velocity is less than the escape velocity of the halo. The mean particle velocity of hydrogen atoms in a Maxwellian distribution is $V_H(T) = (3kT/m_P)^{1/2}$ for a neutral gas, and the escape velocity is given roughly by $V_{esc} \approx \sqrt{3}V_c$. Hence only systems with $V_c \gtrsim V_H(10^4\ \mathrm{K})/\sqrt{3} \approx 9$ km/s are stable against evaporation. These considerations suggest that minihalos with $V_c = 10\text{-}20$ km/s are most likely to produce LLS.

6.2.2 The predicted number density of LLS

The typical collapse redshift of halos with $V_c \lesssim 30$ km/s in current cosmogonies such as the standard CDM model exceeds the critical redshift given in equation (6.10). Such small halos are also abundant at high redshift in these models. It is therefore possible that minihalos contribute a substantial part of the total number of LLS at high redshifts. Here we examine this possibility.

We assume that minihalos which form at $z > z_{crit}$ and do not merge into larger systems by a redshift z_s will contribute to the absorption cross section at z_s. The conditional probability, $p(M_2, z_2|M_1, z_1)dM_2$, that a halo of mass M_1 selected at redshift z_1 will have merged to form a halo of mass between M_2 and $M_2 + dM_2$ at a later redshift z_2, can be calculated from the extended Press-Schechter formalism (Bond et al. 1991; Bower 1991). As in Lacey & Cole (1994), halos are assumed to be destroyed by redshift z_s, if they have merged into halos of twice their initial mass by that redshift. The fraction of minihalos that form at z_1 and survive merging until z_s, f_s, can then be obtained from

$$f_s(M_1, z_1, z_s) = 1 - \int_{2M_1}^{\infty} p(M_2, z_s|M_1, z_1)dM_2. \tag{6.11}$$

The absorption cross section of a minihalo is assumed to be spherical with radius given by equation (6.3). The result for a standard CDM model normalized to $\sigma_8 = 0.7$ is given for three different bins of virial velocities in Figure 1. In the calculation z_1 is chosen as the redshift at which the comoving number density of halos prediced by the Press-Schechter formalism peaks. This corresponds to the collapse redshift of a $\sim 1.5\sigma$ peak. In all cases, $z_1 > z_{crit}$.

Clearly, the total number of systems with $10\ \mathrm{km/s} \lesssim V_c \lesssim 15$ km/s is sufficient to explain the observed number of LLSs at $z \gtrsim 3$. This is consistent with the observational evidence that LLS at low redshift are associated with galaxies (see Steidel et al. 1996). As shown in Mo & Miralda-Escudé (1996), clouds pressure-confined in galactic halos can indeed give a sufficiently large cross section to explain the number density of LLS at $z \lesssim 2$. Note that for current low-Ω cosmogonic models having smaller power on small scales than the standard CDM model, the number density of

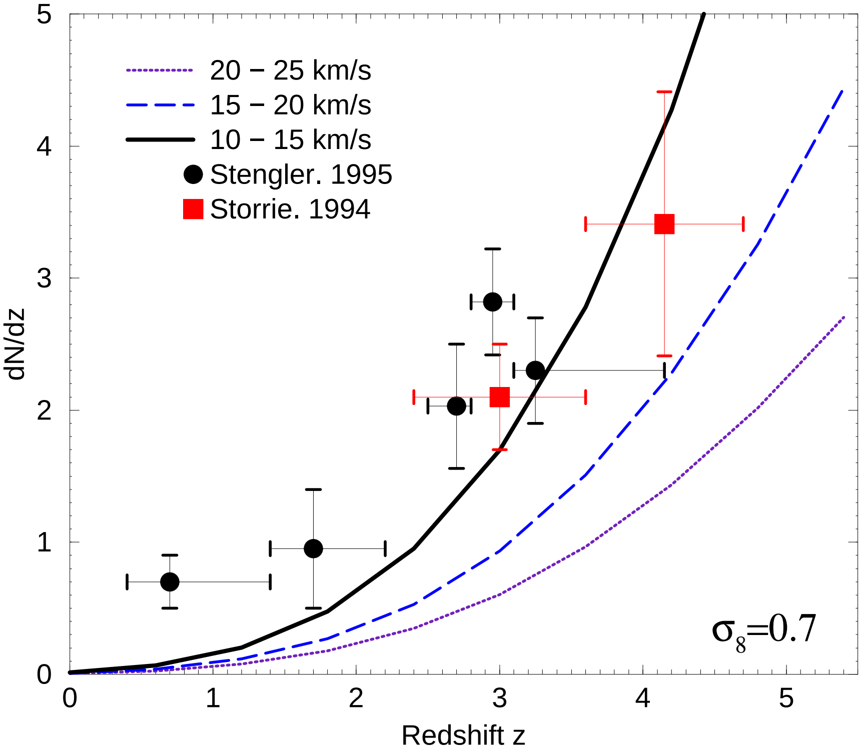

Figure 6.1

The number of LLS per unit redshift. The curves show the prediction of the Standard CDM model with $\sigma_8 = 0.7$. Results are given for minihalos in three V_c bins. The proposed minihalo LLSs provide a significant fraction of all LLS only at redshifts $z \gtrsim 2$. The observational data is taken from Stengler-Larrea et al. (1995) (filled circles) and Storrie–Lombardi et al. (1994) (filled squares).

minihalos may be reduced. However, the predicted number of absorption systems per unit redshift may not be reduced substantially, because it depends also on dl/dz (the proper distance per unit redshift) and the virial radius, both are larger in a low-Ω model. The dependence on cosmological parameters cannot be examined in detail until more detailed hydrodynamical calculations are able to determine the physical sizes of the absorbers.

It is important to realize the difference between our model and the minihalo model proposed by Rees (1986) for Lyman alpha forest systems. In the model of Rees, minihalos are optically thin, highly ionized and have an HI column density of $\ll 10^{17}$ cm^{-2}, characteristic for Lyman alpha forest systems. This assumption is correct for minihalos that collapse after reionization from an already ionized intergalactic medium at redshifts $z < z_{crit}$ [see equation (6.10)].

6.3 DISCUSSION

As shown in Thoul and Weinberg (1996), after reionization the collapse of gas can only happen in halos with $V_c \gtrsim 30\ \mathrm{km/s}$, and so minihalos (with $V_c \lesssim 30\ \mathrm{km/s}$) that form after reionization are not expected to give a significant contribution to the LLS. In contrast, prior to reionization the collapse of gas can even happen in halos with V_c as small as about $0.1\ \mathrm{km/s}(1+z_{coll})$. Our model for the LLS envisages a hierarchical cosmogony where a large number of minihalos (with $V_c \lesssim 30\ \mathrm{km/s}$) can form prior to the epoch of reionization. We show that the gas trapped in such minihalos is, due to its high density, able to withstand photoionization by the UV background set on at a later time and reaches thermal and chemical equilibrium at a temperature $\sim 10^4\ \mathrm{K}$. By including these systems, the discrepancy in the number of LLS between the observational result and earlier theoretical predictions based on CDM models can be reconciled. The model predicts the number density of LLS to keep increasing towards higher redshifts.

The minihalo population is assumed to form at a time when the gas in the IGM is largely primordial. As a result, the absorbing gas in these systems should also have a close to primordial composition. Although later accretion of gas from the enriched IGM may increase the metallicity, we expect the metallicity of such LLS to be low.

Minihalos with $10\ \mathrm{km/s} \lesssim V_c \lesssim 15\ \mathrm{km/s}$ are expected to dominate the total cross section of LLS at high redshifts, because (i) they can form in the low-pressure IGM prior to reionization, (2) they are stable against evaporation, (3) they cannot cool by H_2 or H I to form stars and so are not subject to supernova explosion or internal photoionization, and (4) their total cross section is large in hierarchical models. Thus, the minihalo population of the LLS should be observed to have a narrow range of velocity widths (with H I Doppler parameters of $\lesssim 20\ \mathrm{km/s}$). This can be tested by high-resolution spectroscopy of LLS at high redshifts. The two LLS at redshifts 3.32 and 2.80 studied by Tytler et al. (1996) using the HIRES spectrograph on the KECK telescope have Doppler parameters and velocity offsets between individual components less than $20\ \mathrm{km/s}$. This is consistent with our model. Obviously more high-resolution data at high redshifts are needed to constrain the fraction of LLS in the minihalo population. The sizes for the minihalo absorbers are typically about 1 kpc, which may be tested by the spectra of gravitationally-lensed quasar pairs at high redshifts.

Much theoretical work remains to be done to model the hydrodynamic and radiative-transfer processes to obtain more accurate predictions for the properties of the minihalo Lyman limit systems proposed here.

Chapter 7

Radiative Transfer Effects during photo–heating of the IGM

ABSTRACT

The thermal history of the intergalactic medium (IGM) after reionization is to a large extent determined by photoheating. Here we demonstrate that calculations of the photoheating rate which neglect radiative transfer effects substantially underestimate the energy input during and after reionization. The neglect of radiative transfer effects results in temperatures of the IGM which are too low by a factor of two after He II reionization. We briefly discuss implications for the absorption properties of the IGM and the distribution of baryons in shallow potential wells.

7.1 INTRODUCTION

The absence of a Gunn-Peterson trough (Gunn & Peterson 1965, Scheuer 1965) in the spectra of high-redshift objects is solid evidence that the Universe has been reionized before $z \sim 5$. Hydrodynamical simulations have shown convincingly that at redshifts $z \sim 3$ most baryons are still contained in a photoionized IGM which is responsible for the Lyα forest in the absorption spectra of high-redshift QSO's (Cen et al. 1994, Petitjean, Mücket & Kates 1995; Zhang, Anninos & Norman 1995; Hernquist et al. 1996). However, the detailed distribution of the baryonic component as well as the absorption properties of the IGM will depend on the thermal history of the IGM and thus the heat input due to photoheating (Efstathiou 1992, Miralda-Escude & Rees 1994, Navarro & Steinmetz 1997, Haehnelt & Steinmetz 1998, Bryan et al. 1999; Theuns et al. 1999). Most numerical simulations so far adopted the optically thin limit when calculating photoheating rates. This is, however, a bad approximation during reionization when the optical depth is large. As we will argue later in the case of helium it is also a bad approximation after He II reionization (see also Giroux & Shapiro 1996). Here we investigate radiative transfer effects during and after reionization and discuss implications for the thermal history and absorption properties of the IGM and the distribution of baryons in shallow potential wells. We assume an Einstein-de-Sitter Universe and a Hubble constant of $50\ \mathrm{km/s\ Mpc^{-1}}$.

7.2 PHOTOHEATING

7.2.1 Optical thin *vs* optical thick

In the optically thin limit the mean excess energy of ionizing photons is given by

$$\langle E_{\mathrm{ph}}^{\mathrm{thin}} \rangle = \frac{\int_{\nu_{\mathrm{th}}}^{\infty} \frac{J(\nu)}{h\nu} \sigma(\nu)(h\nu - h\nu_{th}) d\nu}{\int_{\nu_{\mathrm{th}}}^{\infty} \frac{J(\nu)}{h\nu} \sigma(\nu) d\nu} \tag{7.1}$$

where $J(\nu)$ is the flux of ionizing photons $\sigma(\nu)$ is the crossection for ionization, ν_{th} the threshold energy for ionization, and h Planck's constant. For a powerlaw spectrum $J(\nu) = J_0\,(\nu/\nu_{th})^{-\alpha}$ and a powerlaw approximation ($\propto \nu^{-3}$) for the crossection one finds $\langle E_{\mathrm{ph}}^{\mathrm{thin}} \rangle \approx h\nu_{\mathrm{th}}/(\alpha+2) \equiv E_{\mathrm{th}}/(\alpha+2)$. For spectral indices of interest $\alpha > 1$ these excess energies are small fractions of the threshold energy E_{th}. This is because the integral in equation (7.1) is strongly weighted towards the threshold energy. In the optical thick limit where *every* ionizing photon emitted is absorbed the mean excess energy is typically much larger than $\langle E_{\mathrm{ph}}^{\mathrm{thin}} \rangle$ of equation (7.1). For the power-law spectrum discussed above $\langle E_{\mathrm{ph}}^{\mathrm{thick}} \rangle \approx h\nu_{\mathrm{th}}/(\alpha-1)$.

7.2.2 Energy input during reionization

A non–equilibrium multi–frequency 1-D radiative transfer code is used to study the thermal structure of R-type ionization fronts surrounding a point source in spherical symmetry (Abel, Meiksin, & Norman 1999). The code evolves the cooling/heating and chemistry model for primordial gas of Abel et al. (1997) with the methods discussed by Anninos et al. (1997). It solves the static radiative transfer equation in an expanding universe and explicitly conserves photons (Abel, Norman and Madau 1999).

Figure 7.1 shows radial temperature profiles of two different ionization fronts around a luminous QSO (photon emission rate $N_{\rm ph} = 3\times10^{56}\ {\rm s}^{-1}$, $\epsilon(\nu) = \epsilon_0\,(\nu/\nu_0)^{-1.8}$) at $z = 6$ and $z = 4$, respectively. In both cases the front evolves into a homogeneous IGM of primordial composition and mean baryonic density ($\Omega_{\rm bar}h^2 = 0.02$). In the first case the IGM is assumed to be completely neutral and hydrogen and helium reionization occur almost simultaneously. In the second case the gas is assumed to be predominantly in the form of HII and HeII due to a soft UV background already present when the QSO switches on. For both models the ionization front is shown after 10^7 and 10^8 yr.

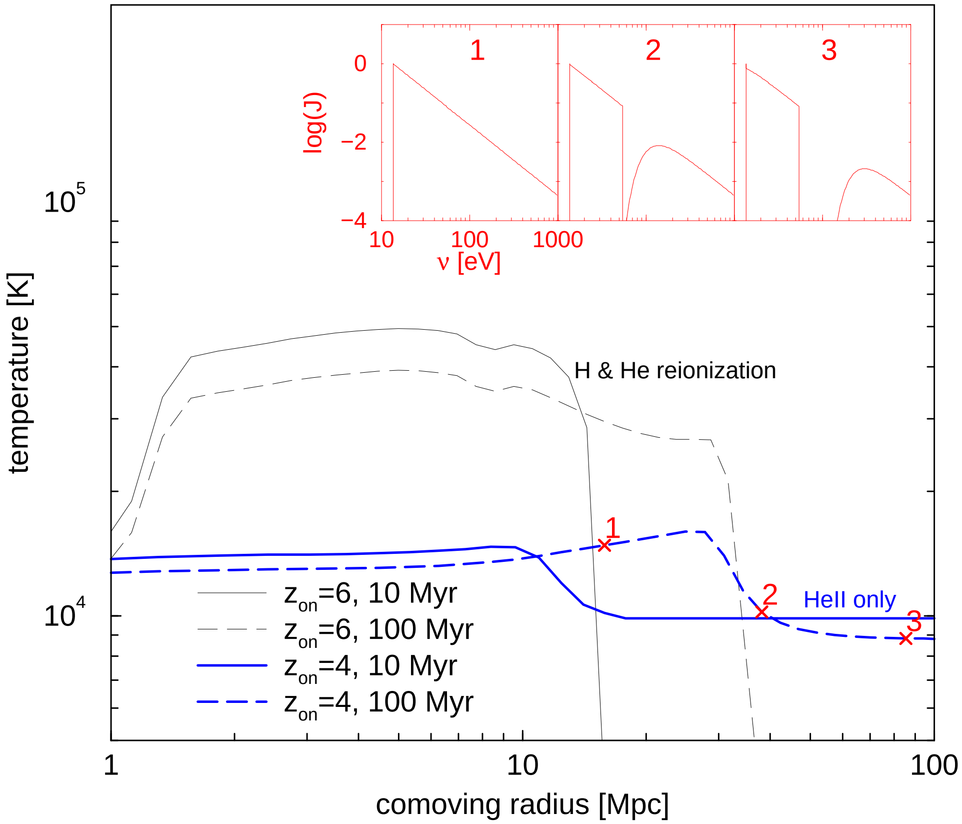

Figure 7.1

Thin and thick curves show the radial temperature profiles of the ionized region around a luminous quasar ($N_{\rm ph} = 3 \times 10^{56}\ {\rm s}^{-1}$) that switched on at $z = 6$ and $z = 4$, respectively. In the first case the ionization front evolves into a completely neutral homogeneous IGM of primordial composition while in the latter case the gas is assumed to be predominatly in the form of H II and He II . For the second case the inset shows the spectral shape of the ionizing flux at the three different radii marked in the figure.

In the first model the ionization front is very sharp due to the small mean free path of hydrogen ionizing photons and the temperature behind the reionization front rises to 50000 K. This corresponds to $\langle E_{\rm ph}\rangle \sim 0.85\times E_{\rm th}$. This is much larger than in the optical thin approximation, $\langle E_{\rm ph}^{\rm thin}\rangle = 0.26E_{\rm th}$, and approaches the optical thick limit, $\langle E_{\rm ph}^{\rm thick}\rangle = 1.25 E_{\rm th}$, for the adopted power-law spectrum with $\alpha = 1.8$ (Zheng et al. 1997). The temperature does not reach the possible maximum of $59000\ {\rm K}$ because of neutral hydrogen line cooling within the ionization front. At later times, when the ionization front has slowed down, hydrogen line cooling of the neutral component during the passage of the ionization front becomes more effective and the temperature reaches $28000\ {\rm K}$. (Miralda-Escude & Rees 1994). This is still nearly a factor two larger than the value of $15000\ {\rm K}$ in the optical thin limit (e.g. Haehnelt & Steinmetz 1998).

In the second case only helium is reionized and hydrogen line cooling plays no role due to the small neutral fraction of hydrogen. The mean free path of HeII ionizing photons is about a factor fifty larger than that of hydrogen ionizing photons and the ionization front extends now over a few (comoving) Mpc. The temperature is raised from 9000K to about 17000K and the total energy input corresponds to $\langle E_{\rm ph}\rangle \sim 0.5 \times E_{\rm th}$, but this value rises to $\langle E_{\rm ph}\rangle \sim 0.7 \times E_{\rm th}$ when the energy deposited ahead of the front is taken into account. The value is again smaller than that in the optical thick limit. This is because the mean free path of an helium ionizing photon becomes larger than the size of the ionized region once $(1 + E_{\rm ph}/E_{\rm th}) > 3.8\,(R/30\ {\rm Mpc})^{1/3}$ (where we have assumed that the ionization cross section scales as ν^{-3} above the threshold). This also explains why the IGM temperature behind the ionization front increases with increasing radius. The inset in Figure 7.1 shows the spectral shape behind, within and ahead of the front to demonstrate how the spectrum of absorbed photons becomes harder across the ionization front.

7.2.3 Photoheating after reonization

After reionization the mean free path of hydrogen ionizing photons is comparable to the mean distance between hydrogen Lyman limit systems (LLS) which is about $350((1+z)/4)^{-3}\ {\rm Mpc}$ comoving (Storrie-Lombardi 1994). Much less is known about the number of helium LLS. The model of Miralda-Escudé, Haehnelt, & Rees (1999, MHR99) which uses a realistic density distribution to treat inhomogeneous reionization predicts a typical distance of $\sim 30\ {\rm Mpc}$ around $z \sim 3$ (see also Fardal, Giroux & Shull 1998). Both values are larger than the typical size of numerical simulations. This is often used as argument to treat photoheating in the optically thin limit. However, it is not before z=1.6 that the mean free path of hydrogen ionizing photons becomes comparable to the Hubble radius (e.g. Madau, Haardt & Rees 1999) and the Universe is likely to be opaque to helium ionizing photons up to the present day. Almost all photons emitted at high redshift will therefore be absorbed within a Hubble time and calculations adopting the optically thin limit must severely underestimate at least the mass-weighted average photoheating rate after reionization.

In the case of hydrogen the mean free path of an hydrogen ionizing photon is smaller than the distance between ionizing sources and the optical depth of LLS is large. At a typical place in the Universe the UV background will be dominated by ionizing photons emitted within the region filling the volume to the next LLSs. In the case of HeII the mean distance between sources of ionizing photons at $z \sim 3$ is $\sim 100\ {\rm Mpc}$ (MHR99) and thus still larger than the mean distance between helium LLS ($\sim 30\ {\rm Mpc}$). Hence, at a typical point in the Universe the HeII ionizing photons will have intersected a helium LLS. The minimum energy input per ionization is thus raised such that $(1 + E_{\rm ph}/E_{\rm th}) > \tau^{1/3}$, where τ is the typical optical depth to the next HeII ionizing source at the ionization threshold. Little is known about the optical depth distribution of helium LLS. However, an even rather low average optical depth of $\tau \sim 10$ to the next source would raise the HeII photoheating rate by more than a factor of four compared to the optical thin case.

The optical thin approximation will significantly underestimate the HeII photo-heating rate. This is true even if the distance between helium LLS were larger than the mean distance between sources of ionizing photons, unless helium LLS have a very large optical depth. To understand this consider the extreme case of a homogeneous emissivity of ionizing photons and many helium LLS with optical depth of order unity at the He II ionization threshold. The ionizing background at a given frequency would then be given by the emisssivity times the mean free path at this frequency, $I(\nu) \propto \epsilon(\nu) l(\nu) \propto \epsilon(\nu)\sigma(\nu)^{-1}$. In this limit the mean absorbed photon energy is equal to the mean emitted energy of photons.

An accurate prediction of the mean absorbed energy is extremely difficult as it depends very sensitively on the spatial distribution of HeII optical depths and ionizing sources during and after reionization and on their emitted spectrum. We can here only roughly estimate that $E_{\rm ph}/E_{\rm th} \sim$ 0.5 to 1 at $z \sim 3$ to decrease with redshift. The effective HeII photoheating rate should thus be between 2 and 4 times larger than that in the optical thin approximation. It could be even larger, if the emitted spectrum were harder than the $\alpha = 1.8$ powerlaw assumed here.

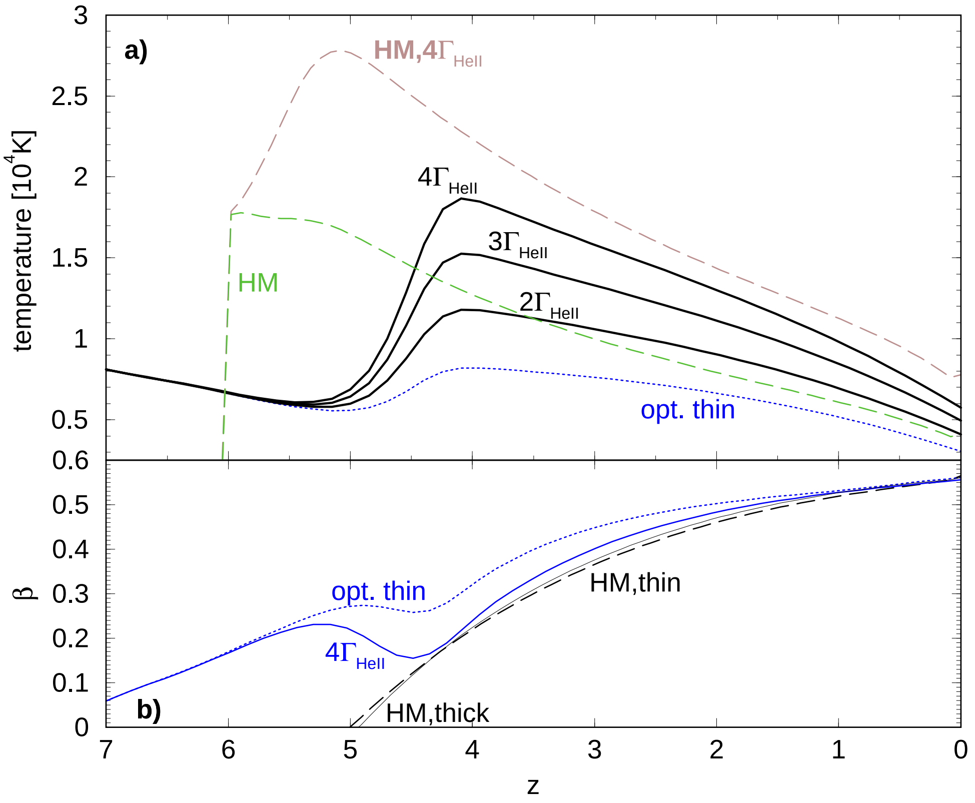

Figure 7.2
a) The temperature evolution of an IGM of primordial composition and mean density assuming a homogeneous UV background as in equation (3). For the solid curves the HeII photoheating rate was raised by a factor 2,3,4, respectively. The dashed curves assume a homogeneous UV background as given by Haardt & Madau (1996) with the HeII photoheating for the optical thin limit and raised by a factor four, respectively. b) The slope $\beta = \mathrm{d}\ln T/\,\mathrm{d}\ln\rho$ of the temperature density relation at mean density.

7.3 IMPLICATIONS

7.3.1 Temperature of the IGM

In the last section we have demonstrated that optical depth effects raise the effective helium photoheating rate by about a factor 2 to 4. Here we investigate the effect of such an increased helium photoheating rate on the temperature of the IGM. We used a non-equilibrium code to calculate the redshift evolution of the ionization state and temperature of an photoionized IGM of primordial composition with mean baryonic density. We have assumed a homogeneous UV background of the form,

$$\begin{aligned} I(\nu,z) &= \left[\frac{1}{1+(7/(1+z))^4}e^{-(z/4)^3}\left(\frac{\nu}{\nu_{\rm HI}}\right)^{-5}\right. \\ &+ \left.\frac{10}{1+(7/(1+z))^4}e^{-(z/2.5)^3}\left(\frac{\nu}{\nu_{\rm HI}}\right)^{-1.8}\right] \\ &\times\; 10^{-21}\ {\rm erg\ s^{-1}\ Hz^{-1}\ sr^{-1}}. \end{aligned} \tag{7.2}$$

This is similar to model C in Haehnelt & Steinmetz 1998. The soft spectrum of the first term mimicks reionization of hydrogen by stars before $z = 6$. The second component represents the contribution of QSO's to the UV background. This quasar contribution is modelled with a $\nu^{-1.8}$ powerlaw as is suggested by the observed spectra of radio quiet quasars (Zheng et al. 1997). The adopted model results in a separate epoch of HeII reionization around $z = 4$.

The predicted temperature evolution of the IGM is given in Figure 7.2. The dotted curve in the upper panel shows the temperature evolution for the optical thin case. For the solid curves we have raised the HeII photoheating rate by factors 2,3 and 4. This corresponds to an increase in the *total* photoheating rate by a factor 1.3, 2 and 2.6, respectively. For reference the dashed curves show the temperature evolution for the UV background as calculated by Haardt & Madau (1996) in the optical thin limit and with the HeII photoheating rate increased by a factor of four.

As pointed out by by MHR99 the assumption of an homogeneous UV background during reionization results in an artificially abrupt reionization. In reality reionization should occur over a significant fraction of the Hubble time. The assumption of a homogeneous background during reionization should nevertheless give a resonable estimate of the mean temperature after reionization even though there will be considerable spatial temperature fluctuations.

At $z \lesssim 6$ adiabatic cooling exceeds Compton cooling and after helium reionization and in a fully photoionized gas the temperature is thus determined by the balance between the photoheating rate, $\Gamma_{\rm ph} = (\alpha_{\rm HeIII}\langle E_{\rm ph}^{\rm HeIII}\rangle n_{\rm HeIII} + \alpha_{\rm HII}\langle E_{\rm ph}^{\rm HII}\rangle n_{\rm HII})n_{\rm e}$ and the adiabatic cooling rate $C_{\rm ad} = 3kTH(z)\rho/\mu m_{\rm p}$, where $\alpha(\propto T^{-0.7})$ is the recombination coefficient , n_e is the electron density, $H(z)$ is the Hubble constant μ is the mean molecular weight and $m_{\rm p}$ is the proton mass. Note that there is no explicit dependence on the strength of the radiation field. This results in a quasi-equilibrium temperature which is approached at late times (Miralda Escudé & Rees 1994)

$$\begin{aligned} T_{\rm ad} &\sim 5.9\times10^3\ (1+z)^{\frac{1.5}{1.7}}\left(\frac{\rho}{\langle\rho\rangle}\right)^{\frac{1}{1.7}}\left(\frac{\Omega_{\rm b}h}{0.04}\right)^{\frac{1}{1.7}} \\ &\left(\frac{\langle E_{\rm ph}^{\rm HeIII}\rangle}{E_{\rm th}^{\rm HeIII}}+0.15\right)^{\frac{1}{1.7}}\ {\rm K}, \end{aligned} \tag{7.3}$$

where we have taken the optical thin limit for hydrogen heating. The increased HeII photoheating rate due to optical depth effects results in an increase of the temperature by factors 1.5–2.5 (Fig. 2a). Changing to a cosmological model with $\Omega = 0.3$ would further raise this temperature by 20 percent at redshift three because of the decrease in the adiabatic cooling rate.

Madau & Efsthathiou (1999) recently suggested that Compton heating by the hard X-ray background might significantly contribute to the heating of the IGM. They obtain for the Compton heating rate at the present day $H_{\rm co} = 1.25 \times 10^{-31}\ {\rm erg\ s^{-1}}$. We can now compare that to the photoheating rate

$$\begin{aligned}\frac{\Gamma_{\rm ph}}{H_{\rm co} f(z) n_e} &\sim 23 \left(\frac{T}{10^4\ {\rm K}}\right)^{-0.7} \left(\frac{\Omega_{\rm bar} h^2}{0.02}\right) \\ &\times \left(\frac{\langle E_{\rm ph}^{\rm HeIII}\rangle}{E_{\rm th}^{\rm HeIII}} + 0.15\right) \frac{\rho}{\langle\rho\rangle} \frac{(1+z)^3}{f(z)}. \qquad (7.4)\end{aligned}$$

Note that the photoheating rate incrases with density while the Compton heating rate does not. The redshift evolution of the Compton heating rate $f(z)$ depends on the evolution of the energy density of the hard X-ray background and the mean energy of the Compton scattered photon. The Klein-Nishina reduction to the Compton cross section becomes increasingly important at high redshift. Madau & Eftathiou (1999) obtain $f(z) \sim (1+z)^{13/3}$ as the approximate redshift dependence if the hard X-ray background was produced at high redshift. Hence, the Compton heating rate by the hard X-ray background exceeds the photo-heating rate only at redshifts larger than

$$\begin{aligned}(1+z) &\sim 10 \left(\frac{T}{10^4\ {\rm K}}\right)^{-0.52} \left(\frac{\Omega_{\rm bar} h^2}{0.02}\right)^{3/4} \\ &\times \left(\frac{\langle E_{\rm ph}^{\rm HeIII}\rangle}{E_{\rm th}^{\rm HeIII}} + 0.15\right)^{3/4} \left(\frac{\rho}{\langle\rho\rangle}\right)^{3/4}. \qquad (7.5)\end{aligned}$$

7.3.2 Absorption properties of the IGM

The raise in temperature should affect the absorption properties of the IGM in several ways. It will increase the thermal broadening of absorption lines but might also introduce additional non-thermal broadening due to pressure-induced motions. The temperature increase due to optical depth effects during HeII photoheating is therefore a good candidate to resolve recently reported difficulties of numerical simulations to reproduce Doppler parameters of Lyα absorption lines at $z = 2$ to 3 as large as those observed (Bryan et al. 1999; Theuns et al. 1999). This would otherwise require an unreasonable large value of $\Omega_{\rm b} h^2$ (Theuns et al 1999). The temperature increase will also increase the mean baryonic density required to match the mean flux decrement in QSO absorption spectra (Rauch et al. 1997). The details of helium heating will furthermore affect the temperature density relation (Hui & Gnedin 1997) and thus the flux decrement distribution. To demonstrate the effect on the temperature density relation we have plotted in Fig. 2b the logarithmic slope $\beta = {\rm d}\ln T/{\rm d}\ln\rho$ at mean density for the same models as in Fig 2a.

7.3.3 Baryons in shallow potential wells

The increased helium photoheating rate will also raise the Jeans mass and will decrease the ability of the gas to cool and collapse into shallow potential wells. It will thus affect the overall distribution of baryons. For photoionized gas the dominant cooling processes during the early stages of the collapse are recombination cooling and Bremstrahlung. The equilibrium between photoheating and recombination cooling ($C_{\rm rec} \propto \rho^2 T^{0.3}$) results in a temperature $T_{\rm rec} \sim 2.3 \times 10^5$ $[(\langle E_{\rm ph}^{\rm HeIII}\rangle/E_{\rm th}^{\rm HeIII}) + 0.15]{\rm K}$. The increased HeII photoheating rate should thus affect the circular velocity threshold above which gas can collapse into dark matter haloes and the fraction of gas that can cool in shallow potential wells (Thoul & Weinberg 1996, Forcada-Miro 1999).

The increased photoheating rates will also raise the circular velocity threshold, V_c, below which baryons in shallow potential wells can be evaporated at reionization (Shapiro et al. 1998; Abel & Mo 1998; Barkana & Loeb 1999). Photo–evaporation occurs when the typical thermal velocities ($\sim (3kT/M_p)^{1/2}$) exceed the escape velocity of the dark matter halo ($\sim \sqrt{3}V_c$). This suggests that if the enhanced photo–heating rate yields a twice as large temperature then the critical V_c for photo–evaporation would be increased by a factor of $\sim \sqrt{2}$.

7.4 CONCLUSIONS

We have studied radiative transfer effects on the energy input into the IGM due to the reionization and photoheating of hydrogen and helium. The energy input depends crucially on the spectral distribution of the photons actually absorbed.

During reionization the spectrum of an ionizing source becomes harder across the ionization front. The energy input is close to the mean energy of the photons between the ionization threshold and the frequency for which the mean free path of an ionizing photons becomes larger than the radius of the ionized region.

After the reionization of HeII the mean spectrum of ionizing photons above the He III ionization edge will also be considerably harder than the emitted spectrum of an individual source. This is because hard photons can pass through helium LLS. The number and optical depth distribution of helium LLS is still highly uncertain. Thus their effect on the UV specrtum is likely to have been underestimated previously.

The increased HeII photoheating rate due to optical depth effects raises the temperature of the IGM typically by about a factor 1.5 to 2.5 compared to the optical thin approximation. It might thus resolve the problem that current numerical simulations of the Lyα forest (which treat photoheating in the optical thin limit) produce Doppler parameters narrower than observed.

The increased HeII photoheating rate will reduce the ability of the gas to collapse into shallow potential wells. It will also raise the circular velocity threshold below which gas in dark matter haloes is photoevaporated during reionization.

CHAPTER 8

Cosmological Radiative Transfer in three Dimensions

ABSTRACT

Many questions in physical cosmology regarding the thermal and ionization history of the intergalactic medium are now succesfully studied with the help of cosmological hydrodynamical simulations. Here we present a a numerical method that solves the radiative transfer around point sources within a three dimensional cartesian grid. The method is energy conserving independently of resolution: this ensures the correct propagation speeds of ionization fronts. We describe the details of the algorithm, and compute as first numerical application the ionized region surrounding a mini-quasar in a cosmological density field at $z = 7$.

8.1 INTRODUCTION

The incorporation of radiation processes and radiative transfer into cosmological hydrodynamical simulations is essential for modeling the structure and evolution of the Ly α forest (Cen et al. 1994; Zhang, Anninos & Norman 1995; Hernquist et al. 1996; Haehnelt & Steinmetz 1998), interpreting the observations of helium and metal line absorbers at high redshift (Reimers et al. 1997; Hellsten et al. 1997; Songaila 1998), and for simulating the early reheating and reionization of the intergalactic medium (IGM) (Ostriker & Gnedin 1996; Gnedin & Ostriker 1997). In the last case the large computational effort is justified by the hope that the study of the transition from a neutral IGM to one that is almost fully ionized could provide some hints on the first generation of stars and quasars in the universe. Until now, radiative transfer effects have either been ignored in such simulations, or treated as a self-shielding correction to an optically thin approximation (Katz et al. 1996; Gnedin & Ostriker 1997). Typically, radiation fields are treated as isotropic backgrounds $J_\nu(z)$ which are either specified as an external function computed by other means (e.g., Haardt & Madau 1996), or are computed by averaging over all sources within the computational volume (Cen 1994; Gnedin & Ostriker 1997). Only approximate treatments exist of the reprocessing of radiation via absorptions internal to the sources as well as by the IGM, an effect that can significantly influence the spectrum of the metagalactic flux (Haardt & Madau 1996). Moreover, at $z \gtrsim 3$ (5) the IGM itself is opaque in the helium (hydrogen) Lyman continuum, and radiation backgrounds become increasingly inhomogeneous and anisotropic (Reimers et al. 1997; Madau, Haardt & Rees 1998). Recent analytic work has attempted to forge a closer connection between sources, transport, and sinks of cosmic radiation, albeit in a spatial– and angle–averaged way (Haiman & Loeb, 1998a, b; Madau, Haardt & Rees 1998).

In this chapter we describe an approach to cosmological radiative transfer which relaxes these assumptions, and is appropriate on scales comparable to the separation of individual sources of radiation. Our method has the property that energy is conserved independently of numerical resolution, ensuring, for example, that ionization fronts propagate at the correct speeds. The radiation driven front surrounding a mini-quasar in a cosmological density field at $z = 7$ is computed as first applications of the technique.

8.2 COSMOLOGICAL RADIATIVE TRANSFER

The equation of cosmological radiative transfer in comoving coordinates (cosmological, not fluid) is (Norman, Mihalas, Paschos & Abel 1999):

$$\frac{1}{c}\frac{\partial I_\nu}{\partial t} + \frac{\hat{n}\cdot\nabla I_\nu}{\bar{a}} - \frac{H(t)}{c}\left(\nu\frac{\partial I_\nu}{\partial \nu} - 3I_\nu\right) = \eta_\nu - \chi_\nu I_\nu \tag{8.1}$$

where $I_\nu \equiv I(t,\vec{x},\hat{n},\nu)$ is the monochromatic specific intensity of the radiation field, $\hat{n}$ is a unit vector along the direction of propagation of the ray; $H(t) \equiv \dot{a}/a$ is the (time-dependent) Hubble constant, and $\bar{a} \equiv \frac{1+z_{em}}{1+z}$ is the ratio of cosmic scale factors between photon emission at frequency ν and the present time t. Here η_ν, χ_ν, and c denote the emission coefficient, the absorption coefficient, and the speed of light, respectively. Equation 8.1 will be recognized as the standard equation of radiative transfer with two modifications: the denominator $\bar{a}$ in the second term, which accounts for the changes in path length along the ray due to cosmic expansion, and the third term, which accounts for cosmological redshift and dilution. In principle, one could solve equation (8.1) directly for the intensity at every point in $(t,\vec{x},\hat{n},\nu)$ space given η and χ. However the high dimensionality of the problem not to mention the high spatial and angular resolution needed in cosmological simulations make this approach impractical. Therefore we proceed through a sequence of well-motivated approximations which reduce the complexity to a tractable level.

Comparing the third with the second term in equation (8.1), the classical transfer equation (Kirchhoff 1860):

$$\frac{1}{c}\frac{\partial I_\nu}{\partial t} + \hat{n}\cdot\nabla I_\nu = \eta_\nu - \chi_\nu I_\nu \tag{8.2}$$

is recovered if the scale of interest, L, is much smaller than the horizon, $c/H(t)$. (Note that this is only true if $|\nu\frac{\partial I_\nu}{\partial \nu}| \leq I_\nu$; i.e., for continuum radiation. However, we can nonetheless still use eq. (8.2) for line transfer provided we Doppler shift the absorption cross section in χ_ν due to Hubble expansion.) In the case of constant absorption and emission coefficients the time derivative can also be dropped and one is left with the static transfer equation

$$\hat{n}\cdot\nabla I_\nu = \eta_\nu - \chi_\nu I_\nu. \tag{8.3}$$

This equation is also adequate for problems in which the absorption and emission coefficients change on timescales much longer than the light crossing time, L/c. This will always be the case in the volumes we will be able to simulate in the near future, and thus we adopt this approximation. At small distances from the source, however, this simplification will always break down allowing I–fronts to expand faster than the speed of light. This can be easily dealt with as we will show in the subsequent section.

An extensive literature exists on methods of solution for equation (8.3) (e.g., Mihalas & Mihalas 1984) depending on the symmetry of the problem and the properties of η_ν and χ_ν. A direct solution of equation (8.3) using the method of short characteristics has recently been carried out in 3+2D on a 128^5 grid (**ref**). However, at a cost of ~ 100 cpu-hours per solution on a ~ 500 GFlop/s supercomputer, this direct approach is obviously impractical for dynamical simulations on large grids. Our approach is approximate, and is based on decomposing the radiation field into point source and diffuse components: $I_\nu \equiv I_\nu^{pts} + I_\nu^{diff}$. The reason for doing this is that whereas I_ν^{pts} is highly anisotropic, we expect I_ν^{diff} to be very nearly isotropic, and accordingly we can employ the best methods taylored for each component.

Utilizing the linearity of the radiation field, we can write:

$$\begin{aligned}\hat{n}\cdot\nabla I_\nu^{diff} &= \chi_\nu(S_\nu - I_\nu^{diff}) && (8.4)\\ \hat{n}\cdot\nabla I_\nu^{pts} &= -\chi_\nu I_\nu^{pts}, && (8.5)\end{aligned}$$

where diffuse emission (e.g., due to recombination radiation) appears only in the transport equation for the diffuse radiation field via the source function $S_\nu \equiv \eta_\nu/\chi_\nu$. This has the advantage that equation (8.5) can now be solved ray by ray in a completely decoupled fashion. For $\chi_\nu(x) = const$, equation (8.5) has the simple analytic solution

$$I_\nu(x_1) = I_\nu(x_0)e^{-\tau} = I_\nu(x_0)\exp(-\chi_\nu(x_1 - x_0)). \tag{8.6}$$

In the next section we describe an efficient implementation for solving equation (8.5) on rays emanating from point sources within a uniform Cartesian grid. Several methods of solution for equation (8.5) are discussed in Norman, Paschos & Abel (1998).

8.3 IMPLEMENTATION

Our method can be stated quite simply as follows. Figure 8.1 gives the flowchart of the simple algorithm; details of the individual computational steps are given in the following sections. For each point source in our volume, a set of radial rays quasi-uniformly distributed in solid angle are constructed. Enough rays are used such that every cell at large distances from the source is crossed by at least one ray *on average.* We are able to use fewer angles than one would naively assume by Monte Carlo sampling in angle within a radiation-matter coupling timescale. Each ray is discretized "cast" into ray segments according to how it intersects the cell boundaries. On each ray segment the intensity is attenuated according to equation (8.5) using an absorption coefficient appropriate to that cell. The number of absorptions in the frequency interval $\nu, \nu + d\nu$ in each ray segment inside a cell is simply related to the decrease in I_ν^{pts} along that segment. The total number of photoionizations in the cell is the sum over all ray segments crossing the cell.

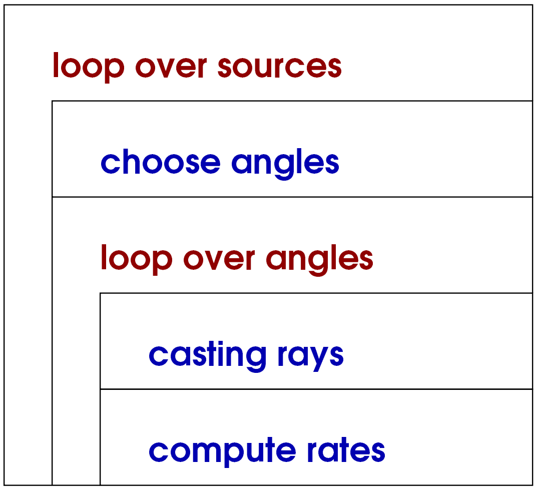

Figure 8.1
The flowchart for the radiation transfer algorithm.

8.3.1 Choosing Angles

To properly describe the I–front one needs at least $N_a = f_a \times 2\pi r/\triangle x$ rays so that at least one ray is casted to each cell of sidelength $\triangle x$ at the equator of a sphere with radius r. We introduced the factor f_a to allow for the number of rays to vary. To adopt the minimum number of rays needed we store the maximum radius, r_{max}, needed to capture the furthest point of the I–front.

We use spherical coordinates (r, ϕ, θ),

$$\begin{aligned} x &= r\cos\phi\,\cos\theta, \quad 0 \le \phi \le 2\pi \\ y &= r\sin\phi\,\cos\theta, \quad -\frac{\pi}{2} \le \theta \le \frac{\pi}{2} \\ z &= r\sin\theta, \end{aligned} \tag{8.7}$$

and divide the sphere in segments of similar size such that all rays will have similar fluxes. We can now find the angles that define the rays which pierce through segments of roughly equal area. The discrete values for θ are given by

$$\theta_j = (j - \frac{1}{2})\frac{2\pi}{N_a} - \frac{\pi}{2}, \quad 1 \le j \le \frac{N_a}{2}. \tag{8.8}$$

Closer to the poles fewer azimuthal angles are required,

$$N^j_\phi = \max(N_a\,\cos\theta, 1). \tag{8.9}$$

The azimuthal angles are now chosen to be,

$$\phi_i = (i - \frac{1}{2})\frac{2\pi}{N_\phi}, \quad 1 \le i \le N_\phi. \tag{8.10}$$

One also needs to know the area of the sphere segment, $A(i,j)$ described by each ray. In units of the surface of the sphere ($4\pi r^2$), this is

$$\begin{aligned} A(i,j) &= \frac{|\sin\theta_2 - \sin\theta_1|}{2N^j_\phi}, \\ \theta_1 &= (j-1)\frac{2\pi}{N_a} - \frac{\pi}{2}, \; \theta_2 = j\frac{2\pi}{N_a} - \frac{\pi}{2}. \end{aligned} \tag{8.11}$$

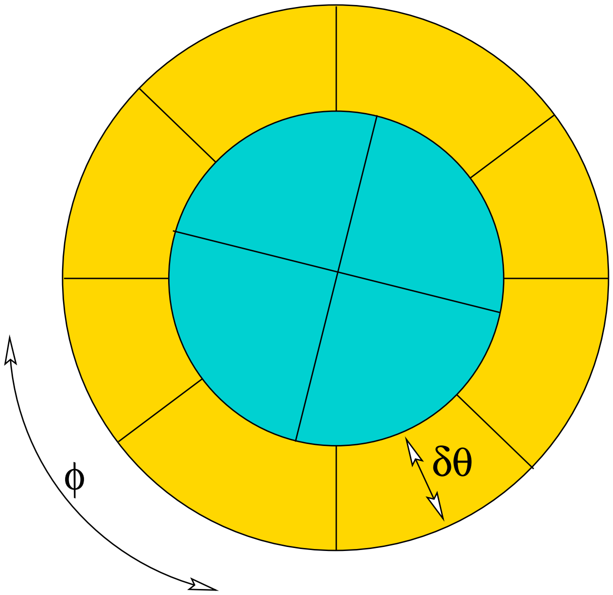

Figure 8.2

Sphere from top with the division into areas of similar size. The azimuthal angle $0 \leq \phi \leq 2\pi$ and $\delta\theta$ are also indicated. The variying $N_\phi(\theta)$ is evident.

A random rotation of the coordinate system is then introduced to avoid any possible pole artifacts and reduce the number of angles in a variety of problems.

8.3.2 Casting Rays

Ray casting is the next step. This means to compute, for a given ray (θ, ϕ), the indices $i(l), j(l), k(l)$ of the grid cells it traverses, as well as the lengths of the ray segments $dS(l)$ within each cell. Here i, j, k are the indices of grid cells in a Cartesian lattice $x(i), y(j)$, and $z(k)$, and l is the index of the ray segment. For simplicity we restrict our discussion to uniform, isotropic grids such that $x(i) = i\Delta, y(j) = j\Delta, z(k) = k\Delta$ where Δ is the cell size and $0 \leq i \leq N_i$, and similarly for j and k. Ray casting is a problem in computational geometry with efficient methods discussed in books on computer graphics. For a uniform Cartesian grid the problem is straightforward. Here we write down a direct algorithm (i.e., requiring no costly sorts). Consider a point source at coordinate x_s, y_s, z_s in cell i_s, j_s, k_s. We have simply $i(1) = i_s, j(1) = j_s, k(1) = k_s$. We cast a ray in direction θ, ϕ and ask which cell boundary it intersects first. If it intersects an x boundary first, $i(2) = i(1) + \text{sign}(\cos\phi), j(2) = j(1), k(2) = k(1)$, and analogously if the y or z boundaries are crossed first. To determine which cell face is crossed first, we compute the distances (radii) from the source to the next x, y or z crossings. Call these distances r_x, r_y and r_z. The minimum of these three distances determines which cell boundary is crossed first.

This can be expressed as follows: Define

$$\begin{aligned} \mu &= \cos\phi, & s_\mu \equiv &\ \text{sign}(\mu) \\ \gamma &= \sin\phi, & s_\gamma \equiv &\ \text{sign}(\gamma) \\ \zeta &= \sin\theta, & s_\zeta \equiv &\ \text{sign}(\zeta) \end{aligned} \tag{8.12}$$

then, for all $l \geq 2$ we have

$$\begin{aligned}
r_x(l) &= |\Delta[i(l) + \frac{1}{2}(s_\mu + 1)] - x_s| / \max(\epsilon, |\mu \cos\theta|) \\
r_y(l) &= |\Delta[j(l) + \frac{1}{2}(s_\gamma + 1)] - y_s| / \max(\epsilon, |\gamma \cos\theta|) \\
r_z(l) &= |\Delta[k(l) + \frac{1}{2}(s_\zeta + 1)] - z_s| / \max(\epsilon, |\mu\, \zeta|)
\end{aligned} \tag{8.13}$$

$$\begin{aligned}
i(l) &= i(l-1) \\
j(l) &= j(l-1) \\
k(l) &= k(l-1) \\
\text{if } [r_x(l) \leq \min(r_y(l), r_z(l))], &\quad \text{then} \\
S(l) &= r_x(l) \\
i(l) &= i(l-1) + s_\mu \\
\text{if } [r_y(l) \leq \min(r_x(l), r_z(l))], &\quad \text{then} \\
S(l) &= r_y(l) \\
j(l) &= j(l-1) + s_\gamma \\
\text{if } [r_z(l) \leq \min(r_x(l), r_y(l))], &\quad \text{then} \\
S(l) &= r_z(l) \\
k(l) &= k(l-1) + s_\zeta.
\end{aligned} \tag{8.14}$$

Here ϵ is a small number to avoid dividing by zero.

8.3.3 Computing Rates

Although the above technique can be applied to any absorption process, in the following we will discuss the specific case of hydrogen photoionization, and compute the photoionization rate coefficient and the associated heating term. Given the path length $dS(l) = S(l) - S(l-1)$, and the absorption coefficient in cell $(i(l), j(l), k(l))$, the optical depth for photoionization along this path is given by $\tau_\nu^l = \chi_\nu(i(l), j(l), k(l)) dS(l)$. Further, from the solution of the static transfer equation (8.6), one sees that $\delta t \times \dot{N}_\nu(l-1)(1 - e^{-\tau_\nu^l})$ photons are absorbed in the time interval, δt. Hence, the rate of change of the neutral hydrogen density, $n_{\rm H}$, due to photoionization is simply given by,

$$\dot{n}_{\rm H} = \dot{N}_\nu^{l-1} \left[1 - e^{-\tau_\nu^l}\right] / V_{\rm cell}, \tag{8.15}$$

where $\dot{N}_\nu$ is the monochromatic number of photons emitted by the source per unit time, and $V_{\rm cell}$ denotes the volume of the cell. The heating rate is then,

$$\dot{e} = (h\nu - 1\,{\rm ryd})\, \dot{N}_\nu^{l-1} \left[1 - e^{-\tau_\nu^l}\right] / V_{\rm cell}. \tag{8.16}$$

Both of the above rates are summed over the contributions of all rays. Employing the analytical solution for each ray segment insures that I–fronts move at the correct speed independent of spatial resolution.

8.3.4 Faster than light I–fronts

In deriving equation (8.3) we have neglected the time dependent term of the transfer equation (8.1). The assumption that the light crossing time is shorter than the ionization timescale breaks down close to the source. As a consequence the I–front expands at a speed exceeding the speed of light. This can also be seen from the simple jump condition in a static universe,

$$4\pi r_I^2 n_{\rm H} \frac{dr_I}{dt} = \dot{N} - 4\pi\alpha_B \int_0^{r_I} n_e n_p r^2 dr, \tag{8.17}$$

where α_B is the recombination coefficient to the excited states of hydrogen. In this expression, dr_I/dt exceeds the speed of light for radii less than $r_c = (\dot{N}/4\pi c n_{\rm H})^{0.5} \approx 5.3\ {\rm kpc}\sqrt{\dot{N}_{56}/n_{\rm H}}$, to subsequently slow down because of geometric dilution. To avoid this unphysical effect we simply do not compute rates at distances further than $r_l = c(t - t_{\rm on})$. The radius r_l is also used in the computation of the optical depths in equations (8.16) and (8.15). Additionally, to speed up the calculation for radii $r < r_c$ we evolve the equations on a tenth of the light travel time across one cell. As a consequence the time evolution of the ionized fration close to the source will not be computed correctly. However, we do not consider this a severe limitation of our approach since the neutral fraction becomes practically zero in regions close to the source within a light travel time.

8.4 APPLICATIONS

In this section we first provide a test case that demonstrates the accuracy of the method, and then, as first application, compute the ionized region surrounding a "mini-quasar" in a cosmological density field at $z = 7$. Mini-quasars could be common at early epochs if black holes can form in the first $10^8\ M_\odot$ cold dark matter (CDM) condensations (Haiman & Loeb 1998b).

8.4.1 Spherical I–front

To test our algorithm we set up a point source in a uniform medium, and neglect the effect of radiative recombinations. The radius of the spherically expanding I–front can be derived analytically by balancing the number of emitted photons with the hydrogen atoms that are present in the ionized volume,

$$R_I(\triangle t) = \left(\frac{3\dot{N}}{4\pi n_{\rm H}}\triangle t\right)^{\frac{1}{3}}. \tag{8.18}$$

Figure 8.3 compares this analytical solution with the results of our algorithm on a 64^3 grid. The radius and the spherical geometry are perfectly recovered within the accuracy of the spatial resolution. The specific parameters used in this test were, $\dot{N} = 10^{51}\ {\rm s}^{-1}$, $n_{\rm H} = 10^{-2}\ {\rm cm}^{-3}$, and $\triangle x = 1$ kpc. The algorithm has also been tested to reproduce accurately the size of classical Strömgren sphere in calculations where radiative recombinations are included.

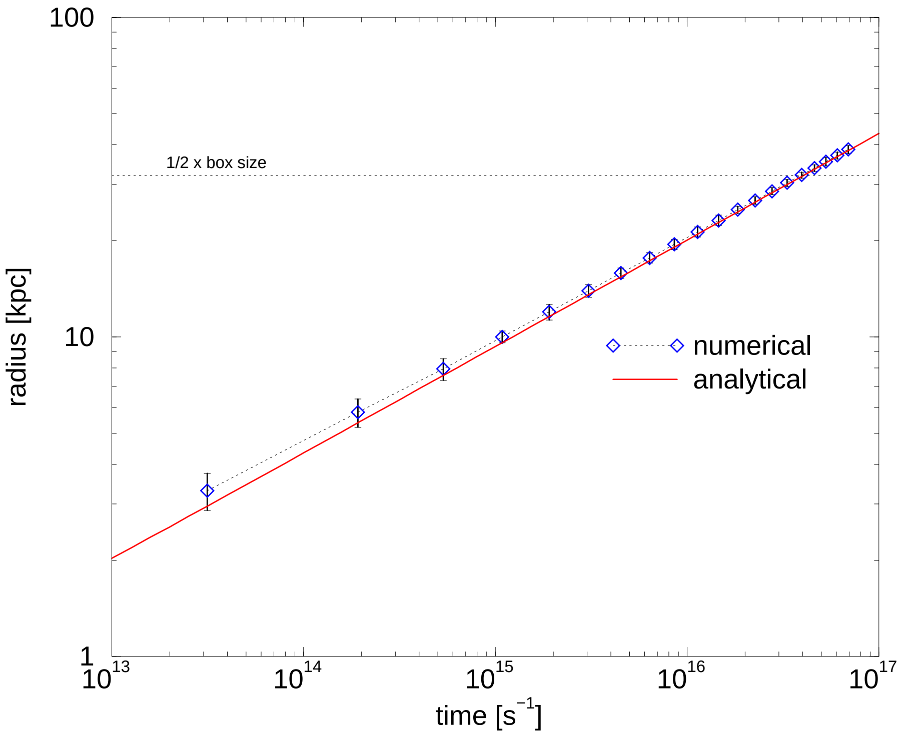

Figure 8.3

Comparison of the analytical radius of an I–front [eq. (8.18)] with the numerical solution on a 64^3 3D cartesian grid. The error bars indicate the maximum deviation found on the spherical ionization front. The deviations are always less than one grid cell. The straight line indicates were part of the I–front leaves the simulation volume. The cell size is 1 kpc in this test case.

8.4.2 Cosmological Density Field

Our first interesting application is the calculation of an the ionized region surrounding a mini-quasar at $z = 7$ in the inhomogeneous density field derived from cosmological simulations. For simplicity, we have neglected any thermal evolution of gas, and included hydrogen radiative recombinations by assuming a constant Case B recombination rate at 7000 K of $\alpha_B = 3.4 \times 10^{-13}$ cm^3 s^{-1} everywhere on the grid. As a background medium we use the H I distribution computed in a SCDM cosmology (with $\Omega_b = 0.06$ and $h = 0.5$) at $z = 6.941$ from Bryan et al. 1998. The 2.4 Mpc box length corresponds to 300 proper kiloparsecs. At the densest cell, which is found in a virialized halo of total mass $\approx 1.3 \times 10^{11}\ M_\odot$, we introduce a quasar-type source with an ionizing photon emission rate of $\dot{N} = 5 \times 10^{53}\ \mathrm{s}^{-1}$. The gas clumping factor is $\langle n_{\mathrm{H}}^2 \rangle / \langle n_{\mathrm{H}} \rangle^2 = 59.2$, and is larger than the ionized hydrogen clumping factor, $C = \langle n_{\mathrm{HII}}^2 \rangle / \langle n_{\mathrm{HII}} \rangle^2$, as clumps that are dense and thick enough to be self-shielded from UV radiation remain neutral and do not contribute to the recombination rate.

Figure 8.4 illustrates the evolution of the I–front during the first 0.6 Myr. The initial spherical expansion (at the speed of light since the number of available photons exceeds by far the number of neutral hydrogen atoms and recombinations) is quickly broken as the front quickly expands first into the voids (increasing their thermal pressure by many orders of magnitude by photo–heating), then more slowly into the denser filaments.

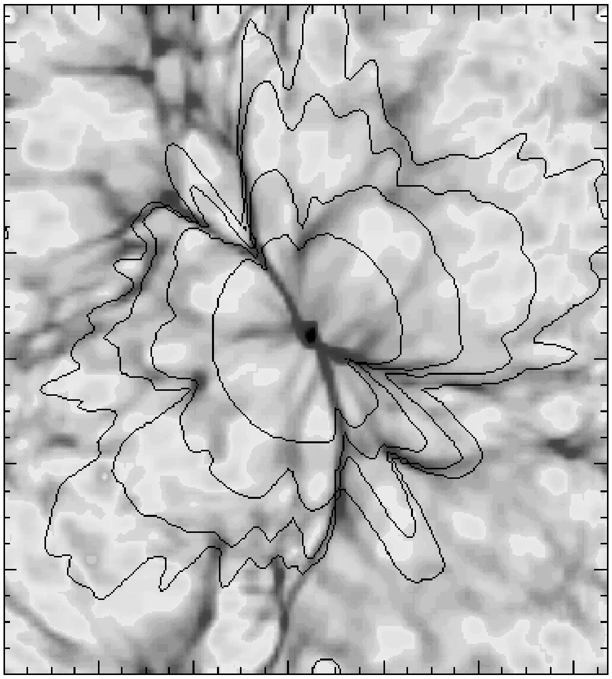

Figure 8.4
Propagation of an R-type I–front in a 128^3 cosmological density field produced by a mini-quasar with $\dot{N} = 5 \times 10^{53}$ s^{-1}. The solid contours give the position of the I–front at 0.15, 0.25, 0.38, and 0.57 Myr after the quasar has switched on. The underlying greyscale image indicates the initial H I density field.

In a highly inhomogeneous universe, the volume-averaged gas recombination timescale,

$$t_{\rm rec} = (n_e \alpha_B C)^{-1} = 0.1\,{\rm Gyr}\left(\frac{1+z}{8}\right)^{-3} C_{20}^{-1} \tag{8.19}$$

(for $\Omega_b h_{50}^2 = 0.06$) is much shorter than the then Hubble time. At later epochs, when the size of the HIIregion is large compared to the scale of the clumping, the front will fill its time-varying Strömgren volume in a few recombination times just like in the static case (Madau, Haardt, & Rees 1998),

$$V_S = \frac{\dot{N} t_{\rm rec}}{n_{\rm H}} = 0.63\,{\rm Mpc}^3 \dot{N}_{53.7}\left(\frac{1+z}{8}\right)^{-6} C_{20}^{-1}. \tag{8.20}$$

This is 20 times larger than our simulation box.

8.5 SUMMARY

Not only for theoretical reasons, but also in light of upcoming space missions such as MAP, PLANCK, and NGST, a detailed understanding of the thermal history of the IGM and reionization is highly desirable. In this chapter we have described a photon conserving algorithm which allows to simulate inhomogenous reionization self–consistently within in a cosmological hydrodynamical simulation. The method employs an on the spot approximation to treat the effects of diffuse emission of ionizing photons. For scenarios in which stellar sources are responsible for hydrogen reionization the on the spot approach is expected to give reliable results. However, for calculations in which diffuse radiation due to recombination of helium is also expected to be important a separate solver can be used. In applications where radiative recombinations can be neglected the number of rays used can be reduced greately due to the variable choice of coordinate system for the selection of rays. Recently, a differnt algorithm for 3D radiative transfer in cosmological situation has been presented by Razoumov and Scott (1998). Their explicit advection scheme (at the speed of light) seems well suited for situations in which the I–fronts move faster than any hydrodynamical flow. Only temporary 2D arrays are used in the mehod presented here requiring negligible small additional memory for 3D cosmological hydrodynamics simulations.

8.6 ANOTHER MUCH FASTER METHOD?

Here we briefly scetch a possible method for solving for the propagation of ionization fronts of N-point sources simultaneously employing variable Eddington tensors. Note that this is only speculative in the sense that I have not implemented or tested this approach.

General considerations I'll discuss a scheme which I believe to be able to propagate multiple I-fornts (including shadowing) at correct speeds. For simplicity of notation I'll specifically discuss the method for a regularly spaced 2-D cartesian grid. For the same reason I will also drop c and κ terms for most of the discussion. Also I only focus on monochromotaic transport for now.

We want to solve the following equation

$$\nabla \cdot \vec{\mathbf{F}} = \epsilon - \kappa E, \tag{8.21}$$

where $\vec{\mathbf{F}}$ is derived from

$$\begin{aligned} \vec{\mathbf{F}} &= -\frac{c}{\kappa_f}\nabla \cdot P, & (8.22)\\ P &= fE. & (8.23) \end{aligned}$$

Here E denotes the photon number density and $\vec{\mathbf{F}}$ then photon number flux. The 2×2 variable Eddington tensor is f which has in this two dimensional case only 2 independent components due to the constraint that $\mathrm{trace}(f) = 1$ and that it has to be symmetric. In three dimensions this would give 5 independent components.

An Ansatz for the variable Eddington tensors The idea here for solving many point-sources simultaneous is to specify the Eddington tensors as if the entire box were optically thin. In this optically thin case we can easily compute the Eddington tensors everywhere on the grid. Given N source of varying photon luminoisty L_k at the postions $\vec{s_k}$ the second moment (P) at position $\vec{r}$ is given by

$$P_{ij}(\vec{r}) = \sum_k^N \frac{L_k}{|\vec{r} - \vec{s_k}|^2} \frac{((\vec{r} - \vec{s_k}) \cdot \hat{n}_i)((\vec{r} - \vec{s_k}) \cdot \hat{n}_j)}{|\vec{r} - \vec{s_k}|^2}. \tag{8.24}$$

To get f_{ij} one would need to divide this by E. This is however not necessary since the requirment that $\mathrm{trace}(f) = f_{11} + f_{22} = 1$ already tells us that $f_{ij}(\vec{r}) = P_{ij}(\vec{r})/\mathrm{trace}(P_{ij}(\vec{r}))$.

Why should this Ansatz be good for cosmological applications? For example HI reionization we will have a quite long period where we need to compute expanding I-fronts before they overlap. The flux there will be dominated by the nearest source which our Ansatz correctly describes. Basically we are assuming that a point in space will be reionized by the source closest to it. What the method says is that in principle we know roughly along which line the photons will travel. Note that it does not say which direction on this line. This direction will still be given from the gradient of fE. This way shadowing is included.

Comments on the numerics We want to solve equation (8.21) in conservative form. I.e. integrate it to get surface integrals for the flux to ensure photon conservation. We then need to note only use zone-centered absorption coefficients but also inperpolated ones at the zone edges (κ_f). However, that shouldn't matter much sine we explicitly conserve photons. Compared to what I believe that you are already solving now this method is only slightly different in that it modifies the difference operator in equation (8.21).

Handling faster than light I-fronts This old problem of faster than light I-fronts will also occur with the method described here up until the chemical timescales at the I-front become shorter than the light travel time from the source to the front position. However, to overcome this problem we can either assume slowly switching on of sources or simply include the time dependent term ($\partial E/\partial t$) in equation (8.21).

Chapter 9

Summary and possible Future Research

This dissertation contains results relating three topics in physical cosmology that were typically studied independently of each other. In the following I will highlight the advances we have made in each field and discuss how they will be unified in future investigations. Also a preview to research which we are currently carrying out and possible valuable extensions of the presented studies is given.

9.1 FIRST STRUCTURE FORMATION

In this thesis we introduce cosmological hydrodynamics as valuable tool in the study of the first objects in the universe. Multiple interesting questions on the nature of the first objects are addressed. We discuss the question of the minimum mass of the first objects, studied their morphology, the formation of primordial molecular clouds, their fragmentation, and the likely nature of these structures. The first baryons that are able to dissipate their gravitational potential energy in the universe are found in virializing dark matter halos of masses $\sim 10^5\ M_\odot$. These halos are formed at the intersection of filamentary structures. The dynamics of these objects is very complex due to the flatness of the powerspectrum on these scales. I.e. a range of modes become gravitationally unstable almost simultaneously. The hydrodynamics show a complex velocity field with multiple shocks within the accretion radius. The gas cools appreciably once its molecular hydrogen fraction exceeds 10^4 by number. The chemical and cooling processes yield cold ($T \sim 200$ K) pockets of gas on scales of ~ 30 pc with densities $\sim 100\ \mathrm{cm}^{-3}$ and masses $\lesssim 10^4\ M_\odot$. Although, their molecular fraction is $\lesssim 10^{-3}$ we identify them as the high redshift analog of present day molecular clouds. We have gained first insight on the physics responsible for fragmentation within these "primordial molecular clouds". Most notably our three dimensional adaptive mesh refinement calculations have identified the Bonnor Ebert mass as the relevant scale for the formation of a massive ($\sim 100\ M_\odot$) molecular cloud core. The fate of these gravitationally unstable condensations will determine the subsequent evolution of its parent cloud.

Scenarios

Assume for the moment that the $\sim 100\ M_\odot$ cores found within primordial molecular clouds do not fragment further. If now a large fraction of the mass in such cores would form a single massive star it would radiate a large number of UV photons. These energetic photons might destroy H_2 in the parent cloud and possibly inhibit further fragmentation and PoPIII star formation. Once this first star explods in a supernovae and enriches its environment with heavy elements new star formation will become possible. Due to metal cooling the enriched regions might be the prefered site of this new star formation phase. As a consequence no zero metalicity star will survive until the present day, consistent with current observations.

The first molecular cloud cores might fragment further giving rise to high and low mass stars. In this case if PoPIII stars with less than a solar mass are formed they still should be on their main sequence today. Their atmospheres, however, might have been poluted by the massive stars that exploded in their surrounding and/or by secondary accretion of metals. In this case the massive stars might still have halted the fragmentation of the parent cloud by the photo–dissociation of molecular hydrogen via the Solomon process. In principle the UV radiation can also photoionize the entire parent cloud causing the interstellar medium to leave the shallow potential well of the DM halo.

What if the core fragments into very small clumps below the hydrogen burning limit ($\lesssim 0.1\ M_\odot$)? In this case one does not expect radiative nor kinetic (explosive) feedback. One might hence envision all the gas in primordial molecular clouds to fragment into such low mass objects. Such scenarios have been put forward to explain the microlensing events, extreme scattering events, and baryonic dark matter. Our results indicate that if indeed fragmentation to such small scale objects were to occur these objects should be strongly clusterd on scales $\ll 10$ pc . In our simulations the dense cores undergo a stage of quasi–hydrostatic contraction before they become gravitationally unstable. During this contraction phase small density perturbations will be damped and one might therefore expect the core to not break up once it becomes fully molecular due to 3–body association. One should note that the PoPIII star formation process necessarily needs to form some massive stars. This is not only because metal enrichement is observed redshifts $\lesssim 5$ it is, of course, also a necessary condition for PoPII star formation.

Let me stress here that within the framwork of a given structure formation model the formation of the first cosmological object is in principal an ab initio calculation. However, once the first star in these objects forms are we currently not able to realistically predict the subsequent evolution. We are left with simplistic modeling and speculations on the future of the first comsological objects. More realistic predictions might be made in the future once we have a better understanding of the star formation and feedback processes in general.

9.2 EFFECTS OF RADIATIVE TRANSFER

Effects of radiative transfer on small scale structure are outlined, in particular the possibility of a radiative negative feedback were discussed. As a consequence such negative radiative feedback on H_2 formation might yield a large number of $\sim 10^6\ M_\odot$ neutral clumps of gas which can explain the observed large number of Lyman Limit Absorption systems in quasar spectra. These small scale systems can originate because the pressure in the IGM is much smaller prior to reionizaiton than it is afterwards. Such small scale structure will play a significant role on how reionization proceeds. This is because the geometry and distribution of these objects might well determine the typical mean free path of an hydrogen ionizing photon. In the case of widely separated ionizing sources, for example, such small objects might have to be photoevaporated first before most of the inter–source medium can see any ionizing photon.

Another important effect of radiative transfer is to enhance the typical photo–heating rate during and after reionization. This is due to the simple effect that a radiation spectrum hardens as it is processed by larger columns of hydrogen or helium. In particular we have examplified how the temperature of the intergalactic medium at $3 < z < 5$ might have a factor two higher temperature than previously assumed. This way the apparent discrepancy between observed and simulated Lyman alpha absorption lines in quasar spectra may easily be resolved. Thus, warranting improvement on current studies of the evolution of the intergalactic medium. In particular the latter will require to incorporate radiative transfer into multi–dimensional hydrodynamic models of the IGM. Also this spectral hardening will influence the details of photo–evaporation of small scale structure.

9.3 NUMERICAL COSMOLOGICAL RADIATION HYDRODYNAMICS

First possible approaches to include radiative transfer in cosmological hydrodynamics are suggested. Such numerical methods are of crucial importance to advance our current modelling and understanding of reionization and the thermal history of the IGM. In particular we explain how cosmological radiative transfer can be reduced to the classical treatment. We would like to emphasize that for current purposes we need to focus on the accurate determination of photo–ionization and heating rates. The radiation field itself can always be reconstructed from the model chemical and hydrodynamic state of the intergalactic medium and the emissivities. We suggest to split the radiative transfer problem into solving point and diffuse sources separately. The suggested ray casting method is powerful since it is highly accurate and conservative by construction. However, the computational effort spent on it scales roughly with the number of sources. One important virtue of the ray tracing algorithm is that it will conserve enery and hence advance ionization fronts at the correct speed independent of grid resolution.

For applications with a lot of sources we have outlined a different approach using variable Eddington tensors. There the computational effort to compute the evolution of the radiation field is independent of the number of sources. Another advantage is that one can choose the desired accurace of the method in selecting ones approach to estimate the Eddington tensors. For the latter we have only given the simplest possible estimate that will work if ionization fronts are widely separated and hence dominated by the nearest source of radiation. For more complex situations Monte–Carlo ray casting techniques seem particularly well suited to give reliable Eddington tensors.

Undoubtedly, numerical cosmological radiation (magneto)–hydrodynamics will become a standard tool in the investigation of the formation and evolution of structure in the universe. In this thesis we have contributed a few new numerical techiques, outlined effects of the rich physics on “small” scales, and shed some new insights on the question “What was the first object to form in the universe?”; the question that Mike Norman had asked me five years ago when I asked him for an undergraduate independent study project. It has been a wonderful scientific journey which I am happily looking forward to continue at Harvard starting this fall.

REFERENCES

Abel, T., 1995, thesis, Univ. Regensburg.

Abel, T., Anninos, P., Zhang, Y., and Norman, M.L. 1997, NewA, 2, 181.

Abel, T., Anninos, P., Norman, M.L., & Zhang, Y. 1998, ApJ, 508, 518.

Abel, T., Bryan, G.L., Norman, M.L. 1999, ApJ, submitted.

Abel, T., & Haehnelt, M. 1999, ApJL, in press.

Abel, T., Meiksin, A., & Norman, M. 1999, in preperation.

Abel, T. & Mo, H.J. 1998, ApJ, 494, L151.

Abel, T., Norman, M.L., Madau, P. 1999, ApJ, in press (astro-ph/9812151).

Abel, T., Stebbins, A., Anninos, P., Norman, M.L. 1998, ApJ, 508, 534.

Abgrall, H. et al. 1992, A&AS, 101,273.

Abraham, R., Tanvir, N., Santiago, B., Ellis, R., Glazebrook, K., & Van den Bergh, S. 1996, MNRAS, 279, L47.

Allen, B., Caldwell, R.R., Shellard, E.P.S., Stebbins, A., and Veeraraghavan, S. 1996, Phys.Rev.Lett, 77, 3061.

Anninos, P., Norman, M.L., & Clarke, D.A. 1994, ApJ, 436, 11.

Anninos, P. and Norman, M.L. 1996, ApJ, 460, 556.

Anninos, P., Zhang, Y., Abel, T., and Norman, M.L. 1997, NewA, 2, 209.

Barkana, R., Loeb, A. 1999, ApJ, submitted, preprint (astro-ph/9901114).

Bell, K.L., and Berrington, K.A. 1987, J. Phys. B20, 801.

Bennett, D.P., Stebbins, A., and Bouchet, F., 1992, ApJ, 399, L5.

Berger, M.J. & Colella, P. 1984, J. Comp. Phys., 82, 64.

Bertoldi, F., Draine, B. T. 1996, ApJ, 458, 222

Bertschinger, E. 1994, Private Communication.

Bertschinger, E. and Watts, 1988, ApJ, 316, 489.

Bodenheimer, P.H. 1986, Final Technical Report, California Univ., Santa Cruz.

Bond, J.R., Kaiser, N., Cole, S., Efstathiou, G. 1991, ApJ, 379, 440.

Bower, R.G. 1991, MNRAS, 248, 332.

Brandenberger, R., Kaiser, N. and Turok, N., 1987 Phys.Rev.D, 36, 2242.

Bryan, G.L., Machacek, M., Anninos, P., & Norman, M.L. 1998, preprint (astro-ph/9805340).

Bryan, G.L., Norman, M.L. 1997, in *Computational Astrophysics*, eds. D.A. Clarke and M. Fall, ASP Conference #123

Bryan, G.L., Norman, M.L. 1998, *in preperation*

Burles, S., Tytler, D. 1998, ApJ, 499, 699

Carr, B.J., Bond, J.R., Arnett, W.D. 1984, ApJ, 277, 445

Cen, R., Miralda-Escudé, J., Ostriker, J.P., Rauch, M 1994, ApJ, 437, 9L.

Chevalier, R.A., and Imamura, J.N. 1982, ApJ, 261, 543.

Ciardi, B., & Ferrara, A. 1997, ApJ, 483, 5L.

Ciardi, B., Ferrara, A., Abel, T. 1999, ApJ, in press.

Colombi, S. 1993, Ph.D. Thesis, l'Universite de Paris 7.

Copi, C.J., Schramm, D.N., & Turner, M.S. 1995, Science, 267, 192.

Couchman, H.M.P. & Rees, M.J. MNRAS, 1986, 221, 53.

Coulson, D., Ferreira, P., Graham, P., and Turok, N., 1994, Nature, 386, 27.

De Jong, T. 1972, A&A, 20, 263.

Dubrovich, V.K. 1977, Soviet, Astron. Lett., 3, 128.

Efstathiou, G. 1993, MNRAS, 256, 43

Fardall M.A., Giroux M.L. and Shull J.M., 1999, AJ, 115, 2206.

Ferland, G.J., Peterson, B.M., Horne, K., Welsh, W.F., & Nahar, S.N. 1992, ApJ, 387, 95.

Fixsen, D.J., Cheng, E.S., Gales, J.M., Mather, J.C., Shafer, R.A., & Wright, E.L. 1997, ApJ, 473, 576.

Forcada-Miro, M.I. 1999, preprint (astro-ph/9712205).

Gardner, J.P., Katz, N., Hernquist, L., & Weinberg, D.H. 1997, ApJ, 484, 31.

Giallongo, E., Cristiani, S., D'Odorico, S., Fontana, A., & Savaglio, S. 1996, ApJ, 466, 44.

Giroux, M.L., and Shapiro, P.R. 1996, ApJS, 102, 191.

Gnedin, N.Y. & Ostriker, J.P. 1997, ApJ, 486, 581.

Gunn, J.E., & Gott, J.R. 1972, ApJ, 432, 1.

Gunn, J.E., and Peterson, B.A. 1965, ApJ, 142, 1633.

Haardt, F., & Madau, P. 1996, ApJ, 461, 20.

Haehnelt, M.G., & Steinmetz, M. 1998, MNRAS, 289, L21.

Haehnelt, M.G., Steinmetz, M., & Rauch, M. 1996, ApJ, 465, 95L.

Haiman, Z., Rees, M.J., & Loeb, A. 1997, ApJ, 476, 458.

Haiman, Z., Rees, M.J., & Loeb, A. 1996a, ApJ, 467, 522.

Haiman, Z., Thoul, A.A., & Loeb, A. 1996b, ApJ, 464, 523.

Haiman, Z., & Loeb, A. 1998a, ApJ, 499, 520.

Haiman, Z., & Loeb, A. 1998b, ApJ, 503, 505.

Haiman, Z., Abel, T., Rees, M.J. 1999, ApJ, in press.

Hara, T., and Miyoshi, S., 1987, Prog. Theor. Phys., 78, 1081.

Hara, T., Yamamoto, H., Mähönen, P., and Miyoshi, S. 1996a, ApJ, 461, 1.

Hara, T., Yamamoto, H., Mähönen, P., and Miyoshi, S. 1996b, ApJ, 462, 601.

Hellsten, U., Dave, R., Hernquist, L., Weinberg, D.H., & Katz, N. 1997, ApJ, 487, 482.

Hernquist, L., Katz, N., Weinberg, D.H., & Miralda-Escudé, J. 1996, ApJ, 457, 51L.

Hogan, C., 1984, Phys. Lett. B., 143B, 87.

Hollenbach, D. & McKee, C.F. 1979, ApJS, 342, 555.

Hoyle, F. 1953, ApJ, 118, 513

Hirasawa, T. 1969, Prog. Theor. Phys., 42, 523.

Hu, W., Scott, D., & Silk, J. 1993, Phys. Rev. D, 49, 648.

Hugoniot, Par H. 1889, J. de l'Ecole Polytechnique, 57, 1.

Hui, L., & Gnedin, N.Y. 1997, MNRAS, 292, 27.

Hutchins, J.B. 1976, ApJ, 205, 103.

Jeans, J.H. 1929, *Astronomy and Cosmogony* ed. Cambridge: Cambridge University Press.

Kashlinsky, A., Rees, M.J. 1983, MNRAS, 205, 955

Katz, N., Weinberg, D.H., Hernquist, L., & Miralda-Escudé, J. 1996, ApJ, 457, 57L.

Kirchhoff, H. 1860, Phil. Mag., 19, 193.

Kolb, E.W., and Turner, M. 1990, *The Early Universe*, Addison–Weseley Publishing Company, Redwood City, California.

Lacey C., & Cole S. 1994, MNRAS, 271, 676.

Lepp, S. & Shull, J.M. 1983, ApJ, 270, 578.

Mac Low, M.-M. & Shull, J.M. 1986, ApJ, 302, 585.

Madau, P., & Efsthathiou, G. 1999, submitted to ApJ, preprint (astro-ph/9902080).

Madau, P., Haardt, F., & Rees, M.J. 1998, ApJ, in press (astro-ph/9809058).

Maoli, R., Ferrucci, V., Melchiorri, F., Signore, M., and Tosti, D. 1996, ApJ, 457, 1.

Maoli, R., Melchiorri, F., and Tosti, D. 1994, ApJ, 425, 372.

Matsuda, T., Sato, H., Takeda, H.1969, Progr. Theoret. Phys., 41, 840

Mihalas, D. & Mihalas, B. 1984, *Foundations of Radiation Hydrodynamics*, New York: Oxford University Press.

Miralda-Escudé, J., Cen, R., Ostriker, J.P., & Rauch, M 1994, ApJ, 471, 582.

Miralda-Escudé, J., & Rees, M.J. 1994, MNRAS, 266, 343.

Miralda-Escudé, J., Haehnelt, M.G., & Rees, M.J. 1999, submitted to ApJ, preprint (astro-ph/9812306).

Mo, H.J. & Miralda-Escudé, J. 1996, ApJ, 469, 589.

Moessner; R., and Brandenberger, R. 1997, astro-ph/970208.

Mücket, J.P., & Kates, R.E. 1997, A&A, 324, 1.

Navarro, J.F., Frenk, C.S., & White, S.D.M. 1996, ApJ, 462, 563.

Norman, M.L., Bryan, G.L. 1997, in *Workshop on Structured Adaptive Mesh Refinement Grid Methods*, ed. N. Chrisochoides

Norman, M.L., Bryan, G.L. 1998, in *Numerical Astrophysics 1998*, eds. S. Miyama & K. Tomisaka

Navarro, J.F., & Steinmetz, M. 1997, ApJ, 478, 13.

Ostriker, J.P., & Gnedin, N.Y. 1996, ApJ, 472, L63.

Ostriker, J.P., & Vishniac, E.T. 1986, ApJ, 306, L51.

Padmanabhan, T. 1993, *Structure Formation in the Universe*, Cambridge University Press.

Padoan, P. 1995, MNRAS, 277, 377.

Padoan, P., Jimenez, R., & Jones B.J.T. 1997, MNRAS, 285, 711.

Palla, F., Salpeter, E.E., & Stahler, S.W. 1983, ApJ, 271, 632.

Paschos, P., Mihalas, D., Norman, M.L. & Abel, T. 1999, in preperation.

Peebles, P.J.E. 1968, ApJ, 153, 1.

Peebles, P.J.E., Dicke, R.H. 1968, ApJ, 154, 891

Peebles, P.J.E. 1993, *Principles of Physical Cosmology*, (Princeton University Press, NJ).

Perivolaropoulos, L., Brandenberger, R., and Stebbins, A. 1990, Phys.Rev.D, 41, 1764.

Petitjean, P., Müket, J.P., & Kates, R.E. 1995, A&A, 295, L9.

Press, W.H. & Schechter, P. 1974, ApJ, 187, 425.

Puy, D., Signore, M. 1996, A&A, 305, 371

Rankine, W.J.M. 1870, Phil. Trans. Roy. Soc. London, 160, 277.

Razoumov, A.O., & Scott, D. 1998, preprint (astro-ph/9810425).

Rees, M.J. 1986, MNRAS, 218, 25P.

Rees, M.J. 1986, MNRAS, 222, 27.

Reimers, D., Köhler,S., Wisotzki, L. Groote, D., Rodriguez-Pascual, & P. Wamsteker, W. 1997, å, 327, 890.

Saslaw, W.C. & Zipoy, D. 1967, Nature, 216, 976.

Sauval, A.J, & Tatum, J.B. 1984, ApJS, 56, 193.

Scheuer P., 1965, Nature, 207, 963.

Silk, J. 1983, MNRAS, 205, 705

Shapiro, P.R. and Kang, H. 1987, Rev. Mexicana Astron. Astrof., 14, 58.

Shapiro, P.R. & Kang, H. 1987, ApJ, 318, 32.

Shapiro, P.R., Raga, A.C., & Mellema, G. 1998, Mem.S.A.It., 69, 463.

Shapiro, P.R., Iliev, I.T., Raga, A.C. 1999, preprint (astro-ph/9810164).

Scherrer, R., Melott, A., and Bertschinger, E. 1989, Phys.Rev.Lett, 62, 379.

Songaila, A. & Cowie, L.L. 1996 AJ, 112, 335.

Songaila, A. 1998, ApJ, 480, L1.

Sornborger, A., Brandenberger, R., Fryxell, B., and Olson, K. 1997, ApJ, 482, 22.

Sornborger, A. 1997, astro-ph/9702038.

Stebbins, A., Veeraraghavan, S., Brandenberger, R., Silk, J., and Turok, N. 1987, ApJ, 322, 1.

Steidel, C.C. 1990, ApJS, 74, 37.

Steidel, C.C. 1995, in QSO Absorption Lines, ed. G. Meylan. Springer, Berlin, p.139.

Steidel, C.C., Giavalisco, M., Pettini, M., Dickinson, M. & Adelberger, K.L. 1996, ApJ, 462, 17L.

Stengler–Larrea, E.A., Boksenberg, A., Steidel, Charles C., Sargent, W.L.W., Bahcall, J.N., Bergeron, J., Hartig, G.F., Jannuzi, B.T., Kirhakos, S., Savage, B.D., Schneider, D.P., Turnshek, D.A., and Weymann, R.J. 1995, ApJ, 444, 64.

Stone, J.M., and Norman, M.L. 1992, ApJS, 80, 753.

Storrie–Lomardie, L.J, McMahon, R.G., Irwin, M.J., and Hazard, C. 1994, ApJ, 427, L13.

Sunyaev, R.A. & Zel'dovich, Ya.B. 1972, å, 20, 189.

Takeda, H., Sato, H., Matsuda, T. 1969, Progr. Theoret. Phys., 41, 840

Tegmark, M., Silk, J., Rees, M.J., Blanchard, A., Abel, T., Palla, F. 1997, ApJ, 474, 1.

Theuns, T., Leonard, A., Schaye, J., & Efstathiou, G. 1999, preprint (astro-ph/9812141).

Thoul, A.A. & Weinberg, D.H. 1996, ApJ, 465, 608.

Tiné, S., Lepp, S., & Dalgarno, A. 1998 in preperation.

Tytler, D., Burles, S., & Kirkman, D. 1996, preprint, astro-ph/9612121.

Vilenkin, A. and Shellard, E.P.S. 1994, Cosmic Strings and Other Topological Defects (Cambridge Monographs on Mathematical Physics).

Wampler, E.J., Williger, G.M., Baldwin, J.A., Carswell, R.F., Hazard, C., and McMahon, R.G. 1996, A&A, 316, 33.

Williger, G.M., Baldwin, J.A., Carswell, R.F., Cooke, A.J., Hazard, C., Irwin, M.J., McMahon, R.G., and Storrie-Lombardi, L.J. 1994, ApJ, 428, 574.

Wishart 1979, MNRAS, 187, 59P.

Wolfe, A.M., Fan, X.M., Tytler, D., Vogt, S.S., Keane, M.J., Lanzetta, K.M. 1994, ApJ, 435, L101.

Zanchin, V., Lima, J.A.S., and Brandenberger, R. 1996, Phys.Rev.D, 54, 6059.

Zel'dovich, Ya.B, & Sunyaev, R.A. 1969, AA&SS, 4, 301.

Zhang, Y. & Anninos, P., & Norman, M.L. 1995, ApJ, 453, L57.

Zhang, Y., Norman, M.L., Anninos, P., & Abel, T. 1997, proceedings of the 7th Annual Astrophysics Conference in Maryland, *Star formation, near and far*, eds. Stephen S. Holt and Lee G. Mundy.

Zheng, W., Kriss, G.A., Telfer, R.C., Grimes, J.P., Davidsen, A.F. 1997, ApJ, 475, 469.

CURRICULUM VITAE

Personal:

Name:	Tom Abel
Present Address:	Harvard Smithsonian Center for Astrophysics 60 Garden Street Cambridge, MA 02138
email:	tabel@cfa.harvard.edu
Born:	September 3, 1970, Straubing, Germany
Citizenship:	German
Marital Status:	Single

Education & Employment:

1980 - 1986	Robert Koch Gymnasium Deggendorf
1986 - 1988	Fachoberschule Deggendorf
1988 - 1989	Fachhochschule Isny, general physics
1989 - 1990	Fachhochschule München, technical physics
1990 - 1998	University of Regensburg in general physics
1993 - 1994	Exchange Student at the University of Illinois
1995	Master thesis at the University of Regensburg *Molecular Hydrogen and the first Light in the Universe* Advisors: M.L. Norman, U. Krey
7/96 - 7/99	Visiting Research Scholar at the National Center for Supercomputing Applications.
1/97 - 9/99	Visitor at the Max Planck Institute for Astrophysics, Garching.
6/1999	Submitted this PhD thesis at the Ludwig Maximillians University Munich Advisor: S. D. M. White.
10-99 - now	Postdoctoral Fellow at the Harvard Smithsonian Center for Astrophysics

Teaching Experience

1990-1992: Lecturer at the Berufsfortbildungszentrum Regensburg
(re–integration program for longterm unemployed people in Germany)
for basic astronomy, math, physics, biology, and computer science
1990-1994: Tutoring from high–school to university level
1993-1994: Teaching Assistant, Math Department, University of Regensburg

Awards

Oskar Karl Forster Scholarship, 1993
DAAD Scholarship, 1993-1994